Simulation du bullage dans un photobioréacteur

Wenbiao Jiang

université PARIS-SACLAY

CentraleSupélec

NNT : 2018SACLC086

Thèse de doctorat

Simulation of bubbling in a photobioreactor

Thèse de doctorat de l'Université Paris-Saclay
préparée à CentraleSupélec

Ecole doctorale n°579 Sciences mécaniques et énergétiques, matériaux et géosciences (SMEMaG)
Spécialité de doctorat : Génie des procédés

Thèse présentée et soutenue à Gif-sur-Yvette, le 5 décembre 2018, par

M. WENBIAO JIANG

Composition du Jury :

M. HAVET Jean-Louis Professeur, GPIP, CNAM Paris	Président
Mme. CHARCOSSET Catherine DR CNRS, LAGEP, Université Lyon 1	Rapporteur
Mme. CHARTON Sophie Chercheur Senior HdR, CEA Marcoule	Rapporteur
M. DALMAZZONE Didier Professeur, UCP, ENSTA Paris Tech	Examinateur
M. POZZOBON Victor Ingénieur de Recherche, Dr., LGPM, CentraleSupélec	Co-directeur de thèse
M. PUEL François Professeur, LGPM, CentraleSupélec	Directeur de thèse

CentraleSupélec, Université Paris-Saclay

Doctoral Thesis

Simulation of bubbling in a photobioreactor

Author:
Wenbiao Jiang(姜文彪)

Supervisors:
Dr. Victor Pozzobon
Prof. François Puel

A thesis submitted in fulfillment of the requirements for the degree of Doctor of Philosophy

in the

Laboratoire de génie des procédés et matériaux
L'école doctorale: SMEMaG - ED579

December 5th, 2018

Declaration of Authorship

I, Wenbiao JIANG, declare that this thesis titled, "Simulation of bubbling in a photobioreactor" and the work presented in it are my own. I confirm that:

- This work was done wholly or mainly while in candidature for a research degree at this University.
- Where any part of this thesis has previously been submitted for a degree or any other qualification at this University or any other institution, this has been clearly stated.
- Where I have consulted the published work of others, this is always clearly attributed.
- Where I have quoted from the work of others, the source is always given. With the exception of such quotations, this thesis is entirely my own work.
- I have acknowledged all main sources of help.
- Where the thesis is based on work done by myself jointly with others, I have made clear exactly what was done by others and what I have contributed myself.

Signed: 姜文彪 JIANG Wenbiao

Date: December 13th, 2018.

「仁遠乎哉?我欲仁，斯仁至矣。」

孔子

"*Il n'y a rien qui soit entièrement en notre pouvoir que nos pensées.*"

René Descartes

"*Nur die Kunst und die Wissenschaft erhöhen den Menschen bis zur Gottheit.*"

Ludwig van Beethoven

"*Knowledge is a limitless ability to interpret and reinterpret itself - it cannot be set down exhaustively in any single set of formulas, for universal, once-for-all use.*"

John M. Cooper

Acknowledgements

First and foremost I want to thank my supervisor Prof. François Puel for the continuous support of my PhD study and related research, for his patience, motivation, and immense knowledge. His guidance helped me in all the time of research and writing of this thesis. I could not have imagined having a better supervisor for my PhD study.

My deep and unrestrained appreciation goes to my co-supervisor Dr. Victor Pozzobon, who gave me invaluable and insightful advice throughout my doctoral study. Specially, he also trained me in numerical simulations and corrected my manuscript. A thousand thanks for his help!

For this dissertation I would like to thank my reading committee members: Ms. Catherine Charcosset, Ms. Sophie Charton, for their time, interest, and helpful comments. I would also like to thank the other two members of my oral defense committee: Mr. Didier Dalmazzone, Mr. Jean-Louis Havet (also as president) for their time and insightful questions.

I would like to thank Prof. Patrick Perré, who helped to design the reactor and gave other useful suggestions, Mr. Thierry Martin, who has manufactured a sophisticated reactor, Mr. Joel Casalinho, who has set up the electrical part of the experimental system, they all taught me the necessary skills for the experiments. Specially, I would like to thank Prof. Hervé Duval for generously lending us his high speed camera and other devices. All the other colleagues in our lab, you all deserve my gratitude!

I would also like to thank all my friends who I can talk to when I had problems in research and life.

My sincere gratitude goes to my homeland for financially supporting my study by China Scholarship Council (CSC 201504490092).

Last, but certainly not least, I wish to express my deepest gratitude to my family for all their love and encouragement. For my parents who gave me life and do everything possible to let me have good education and living conditions. For my sister who is always a mentor in my life, also gives me financial and emotional support.

Contents

List of Figures

List of Tables

List of Abbreviations

2D	Two-dimensional
3D	Three-dimensional
CFD	**C**omputational **F**luid **D**ynamics
CFL	**C**ourant-**F**riedrichs-**L**ewy
CPU	**C**entral **P**rocessing **U**nit
CSF	**C**ontinuum **S**urface **F**orce
C.V.	**C**ontrol **V**olume
D-A	**D**onor-**A**cceptor
DOM	**D**iscrete **O**rdinates **M**ethod
E-E	**E**ulerian-**E**ulerian
E-L	**E**ulerian-**L**agrangian
HSM	**H**orizontal **S**egmentation **M**ethod
IA	**I**nterrogation **A**rea
LDA	**L**aser **D**oppler **A**nemometry
LED	**L**ight-**e**mitting **d**iode
LIF	**L**aser-**I**nduced **F**luorescence
MCM	**M**onte **C**arlo **M**ethod
OpenFOAM	**Open** Source **F**ield **O**peration **a**nd **M**anipulation
PBE	**P**opulation **B**alance **E**quation
PBR	**P**hoto**bio**reactor
PC	**P**ersonal **C**omputer
PDE	**P**artial **D**ifferential **E**quation
PIV	**P**article **I**mage **V**elocimetry
PLIC	**P**iecewise **L**inear **I**nterface **C**alculation
RTE	**R**adiative **T**ransfer **E**quation
SLIC	**S**imple **L**inear **I**nterface **C**alculation
VFC	**V**olumetric **F**low **C**ontroller
VOF	**V**olume **O**f **F**luid

List of Symbols

Symbol	Name	Units
A	area	m^2
$[A]$	matrix representation of an operator	-
A_R	aspect ratio	1
$[b]$	known column vector	-
C	mass concentration	$kg{\cdot}m^{-3}$
c	general coefficient	-
Co	Courant number	1
D	dilution rate	s^{-1}
$\mathcal{D}$	diffusivity	$m^2{\cdot}s^{-1}$
d	diameter	m
e	base of the natural logarithm	-
Eo	Eötvös number	1
$\mathscr{F}$	indicator function	1
F	general force	N ($kg{\cdot}m{\cdot}s^{-2}$)
f_{ext}	force per unit mass	$m{\cdot}s^{-2}$
f_C	force per unit length	$N{\cdot}m^{-1}$
f_σ	force per unit volume	$kg{\cdot}m^{-2}{\cdot}s^{-2}$
f	general force per unit mass/volume/length	$N{\cdot}kg^{-1}$, $N{\cdot}m^{-3}$ or $N{\cdot}m^{-1}$
$\mathfrak{f}$	frequency	Hz (s^{-1})
f_{circ}	circularity	1
G	general function	1
H	dimensionless Henry coefficient	1
h	height	m
$\mathcal{I}$	pixel intensity	-
I	specific radiative intensity	$W{\cdot}m^{-2}{\cdot}sr^{-1}{\cdot}Hz^{-1}$
i	general integer	-
J	mass flux	$kg{\cdot}m^{-2}{\cdot}s^{-1}$
j	general integer	-
j_e	emission coefficient	$m{\cdot}s^{-3}{\cdot}sr^{-1}$
$\mathfrak{k}$	general integer	-
k_a	general coefficient	-
k, k_g, k_l	mass transfer coefficient	$m{\cdot}s^{-1}$
K_s	substrate concentration when $\mu = 0.5\mu_{\max}$	$kg{\cdot}m^{-3}$
K_g, K_l	overall mass transfer coefficient	$m{\cdot}s^{-1}$
l	general integer	-
M	mass	kg
m	general integer	-
Mo	Morton number	1
N	general integer	-
$\mathcal{N}$	total cell number	-
$\mathfrak{n}$	refractive index	1

n	amount of substance	mol
$\vec{n}$	normal vector at interface ($\approx \nabla\alpha_l$)	m^{-1}
$\hat{n}$	unit normal vector at interface	1
n_c	cell number density in total space	-
$\mathcal{O}$	truncation error	-
P	product concentration	$\mathrm{kg{\cdot}m^{-3}}$
$\mathcal{P}$	rate of photosynthesis	-
$\mathscr{P}$	perimeter	m
$\mathfrak{p}$	momentum	$\mathrm{kg{\cdot}m{\cdot}s^{-1}}$
$\overline{\mathfrak{p}}$	volume-averaged momentum	$\mathrm{kg{\cdot}m^{-2}{\cdot}s^{-1}}$
p	pressure	Pa ($\mathrm{kg{\cdot}m^{-1}{\cdot}s^{-2}}$)
Q	volumetric flow rate	$\mathrm{m^3{\cdot}s^{-1}}$
q	quadrature weight	-
r_X	cell growth rate	$\mathrm{kg{\cdot}m^{-3}{\cdot}s^{-1}}$
r_D	cell death rate	$\mathrm{kg{\cdot}m^{-3}{\cdot}s^{-1}}$
r_S	substrate consumption rate	$\mathrm{kg{\cdot}m^{-3}{\cdot}s^{-1}}$
r (as subscript)	spatial coordinates	m
r	radius	m
$\vec{r}$	position	m
R	radius	m
$\mathcal{R}$	random number	-
Re	Reynolds number	1
S	substrate concentration	$\mathrm{kg{\cdot}m^{-3}}$
s	source term	-
$\hat{s}$	general normalized vector	m
s_c	variation of cell number density in total space	-
t	time	s
T	thermodynamic temperature	K
u	velocity	$\mathrm{m{\cdot}s^{-1}}$
V	volume	$\mathrm{m^3}$
v	velocity in PIV	$\mathrm{m{\cdot}s^{-1}}$
v_g	injecting gas velocity	$\mathrm{m{\cdot}s^{-1}}$
$\mathfrak{w}$	work per unit area	$\mathrm{J{\cdot}m^{-2}}$ ($\mathrm{kg{\cdot}s^{-2}}$)
w	width	m
X	cell concentration	$\mathrm{kg{\cdot}m^{-3}}$
$[x]$	unknown column vector	-
Y	yield coefficient	1
x, y, z	spatial coordinates	m

α	contact angle	rad
α_l	volume fraction of liquid	1
β	contact angle	rad
β_e	extinction coefficient	$\mathrm{m^{-1}}$
δ	difference	-
Δ	difference	-
Δx (in chapter 4)	mesh size	m
Δr	displacement	m
ε	general coefficient	-
ϵ	variation of cell number density in physical space	-
θ (in chapter 2)	contact angle	rad

θ (in chapter 5)	azimuthal angle in spherical coordinates	rad
ζ	velocity in an internal space	-
η	dynamic viscosity	Pa·s ($kg{\cdot}m^{-1}{\cdot}s^{-1}$)
κ	curvature	m^{-1}
κ_a	absorption coefficient	m^{-1}
Λ	a constant between 0 and 1	-
λ	Henry coefficient	$Pa{\cdot}m^3{\cdot}mol^{-1}$
μ_a	attenuation coefficient	m^{-1}
μ	specific cell growth rate	s^{-1}
ν	kinematic viscosity	$m^2{\cdot}s^{-1}$
ξ	coordinates of an internal space	-
π	Pi	-
ρ	density	$kg{\cdot}m^{-3}$
σ	surface tension	$N{\cdot}m^{-1}$ ($kg{\cdot}s^{-2}$)
σ_s	scattering coefficient	m^{-1}
τ	optical path length	m
Φ	cross-correlation	-
ϕ	polar angle in spherical coordinates	rad
χ	cell number density in physical space	-
Ψ	scattering phase function	-
ψ	general scalar field	-
Ω	volume	m^3
Ω (as $d\Omega$)	solid angle	sr
∇	nabla operator, $\nabla = \left(\frac{\partial}{\partial x}, \frac{\partial}{\partial y}, \frac{\partial}{\partial z}\right)$	m^{-1}

Physical Constants

Air density	$\rho_{\text{air}} = 1.19\ \text{kg}\cdot\text{m}^{-3}$
Air dynamic viscosity	$\mu_{\text{air}} = 1.80 \times 10^{-5}\ \text{Pa}\cdot\text{s}$
Air molar mass	$M_{\text{air}} = 2.90 \times 10^{-2}\ \text{kg}\cdot\text{mol}^{-1}$
Air-water surface tension	$\sigma_0 = 7.20 \times 10^{-2}\ \text{N}\cdot\text{m}^{-1}$
Atmospheric pressure	$p_{\text{atm}} = 1.00 \times 10^{5}\ \text{Pa}$
Gravitational acceleration	$g = 9.80665\ \text{m}\cdot\text{s}^{-2}$
Gas constant	$\mathscr{R} = 8.3144598\ \text{J}\cdot\text{mol}^{-1}\cdot\text{K}^{-1}$
Room temperature during experiments	$T_0 = 293\ \text{K}$
Water density	$\rho_{\text{water}} = 998\ \text{kg}\cdot\text{m}^{-3}$
Water dynamic viscosity	$\mu_{\text{water}} = 1.00 \times 10^{-3}\ \text{Pa}\cdot\text{s}$

謹以此博士論文獻給我最親愛的父母和胞姊
感謝他們無微不至的關懷
無條件的支持與鼓勵

This thesis is dedicated to my parents and sister
for their love, endless support
and encouragement.

Je dédie cette thèse à mes parents et ma sœur
pour leur amour inestimable, leur confiance
et leur soutien.

Chapter 1

Introduction

As the industrialization process speed up, we demand more and more energy to fulfill the economic development, as shown in Fig. 1.1 from the report of Petroleum [1]. Meanwhile, we can see from Fig. 1.1 that the largest fraction of consumed energy is still fossil fuel, and it seems that the situation will continue to be so for decades [2]. However, fossil fuel is a non-renewable resource, in other words, it does not renew itself at a sufficient rate for sustainable economic extraction in meaningful human time-frames [3]. Worse still, the combustion of fossil fuel emits enormous amounts of carbon dioxide, a greenhouse gas, into the atmosphere. About half of the emitted carbon dioxide remains in the atmosphere, which results in the global warming and other climate problems [4].

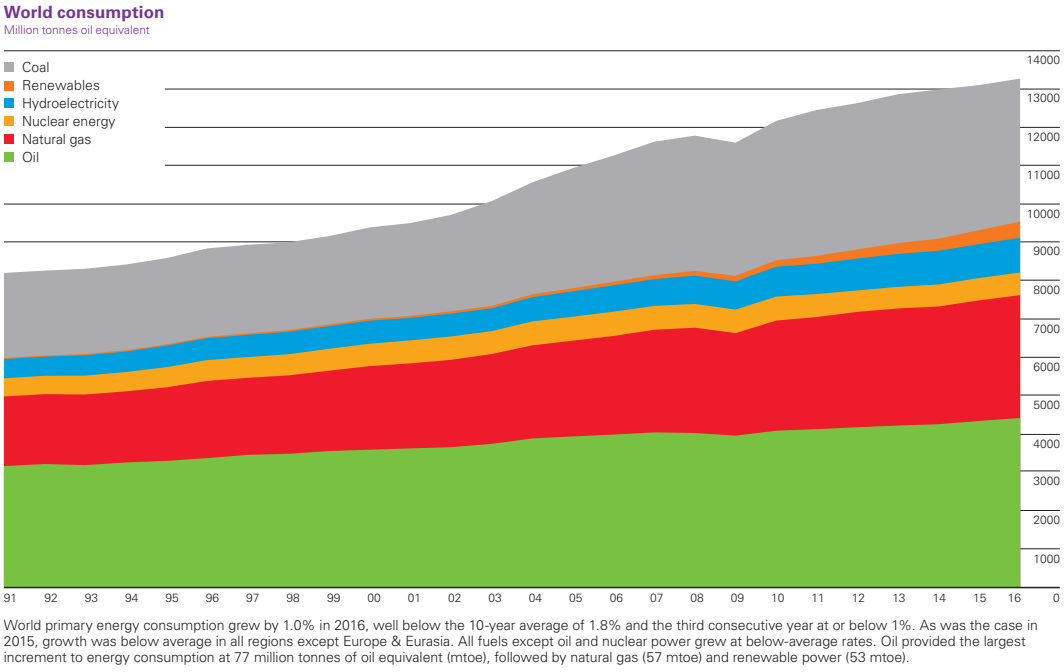

FIGURE 1.1: World energy consumption, illustration from the BP Statistical Review of World Energy June 2017.

To mitigate the climate change, CO_2 capture can be applied to fossil fuel power plants, fuel processing plants and other industrial plants. There are three main systems for capturing CO_2: post-combustion capture, pre-combustion capture and oxy-fuel combustion capture [5]. Here we focus mainly on the post-combustion capture,

whose principal technologies are physicochemical absorbents, deep ocean storage, geological storage and biological fixation [6]. Among these technologies, biological fixation is the only sustainable technology, since it can fix carbon and convert into biofuel and products again. Therefore, biological fixation in principle can mitigate energy shortage and global warming in the same time.

Both terrestrial crops and microalgae can accomplish biological fixation. However, microalgae can fix CO_2 via photosynthesis at higher rate than terrestrial corps can [6], thus microalgae have higher biomass yields per unit land area[7]. Also, the growth of microalgae is not limited by the seasons as the terrestrial crops, which guarantees a stable supply of biomass for industries. Besides, microalgae can be cultivated under the conditions that are unsuitable for the terrestrial crops, for example, they can grow in brackish, saline and waste water [8]. More important, microalgae also have great commercial value, and applications in nutritions, cosmetics, pharmaceuticals, biodiesel, etc. have been widely investigated [9] [10].

There are two main systems to cultivate microalgae: open system and closed system. For example, raceway pond is a typical open system and column photobioreactor is a closed system. In consideration of the small size, the easy monitoring and controllable conditions including illumination, CO_2 consumption, etc., a photobioreactor is more practical and suitable for investigating the microalgal carbon-fixation in a laboratory.

There are various types of photobioreactors in terms of illumination, mixing and shape. For example, both internally-illuminated and externally-illuminated photobioreactors have been developed [11]. To mix gas and liquid, both gentle stirring by impeller and air-lift design are available [12]. As for the shape, tubular, flat panel, vertical column photobioreactors have been widely investigated [13]. In this thesis, the photobioreactor that we investigate is an airlift one, since the shearing of a stirred reactor may damage the mycelium [14]. In addition, the shape of reactor is a cuboid rather than a column, since a cylindrical reactor may cause image distortion when we take images of bubbles and liquid velocity field [15].

The phenomena inside an airlift photobioreactor is a combination of two-phase flow and cell growth [16]. First, air is injected into the reactor and CO_2 is transferred into the microalgal cells by the liquid medium. Meanwhile, air bubbles also play an important role in stirring the liquid and mixing all sorts of nutrients. Subsequently, with the external illumination, the cells convert inorganic carbon into organic carbon by photosynthesis. Each step in the microalgal cultivation is a complicated phenomenon, however, the real complexity of a photobioreactor shows up in the interplay between the basic phenomena. For example, the motion of bubbles obviously influences the mixing of a reactor. Also, the light intensity is attenuated with distance according to Beer-Lambert law [17], accordingly, the cell growth will have fluctuations within the space of the reactor [18]. Besides, the cells travel along with liquid in a recirculated way [19], as a consequence, the cells grow faster when they are entrained towards the reactor wall and vice versa.

At laboratory scale, the cell growth is considered homogeneous due to the recirculation inside a photobioreactor [20]. Therefore, the performance of a lab-scale reactor is mainly determined by the gas-liquid two-phase flow, namely the bubble behaviors and hydrodynamics. Actually, the bubble behaviors largely determine the hydrodynamics, since bubbles are the momentum source of the two-phase flow. Moreover, bubble size and bubble shape have crucial influence on the gas-liquid mass transfer rates, which directly determines the cell growth [21] [22]. Thus, understanding bubble behaviors becomes the very necessary first step to understand the phenomena inside a photobioreactor.

Chapter 2

State of art

This chapter introduces the microalgal cultivation systems, specially the closed systems, i.e. photobioreactors. Understanding the phenomena inside photobioreactors requires both physical and biological knowledge, which are also discussed in this chapter.

2.1 Microalgal cultivation systems

Microalgae are photosynthetic microorganisms that can convert carbon dioxide into organic matter, such as carbohydrates and lipids, which is a feedstock for biodiesel [23] [24], as shown in Fig. 2.1. Therefore, the basic conditions to cultivate microalgae are light, water, CO_2, and other trace elements [25], which can be provided by two kinds of systems, open systems, such as raceway ponds, as shown in Fig. 2.2 and closed systems, such as photobioreactors (PBR), as shown in Fig. 2.3.

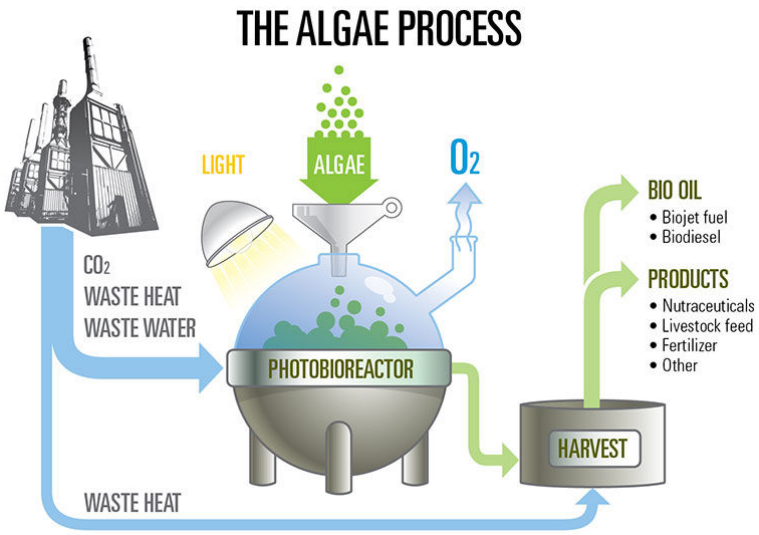

FIGURE 2.1: Illustration of Microalgae process from [26].

The advantages of open systems are lower costs, easier construction and simpler maintenance, thus open systems are widely applied in large-scale industrial productions. However, open system can be easily contaminated by external bacteria, furthermore, the environmental conditions are also difficult to be kept constant [31]. In consideration of these shortcomings, closed systems were designed to provide a more closed space and better control of environmental factors. These two systems are compared in table 2.1 [32] [33] [34].

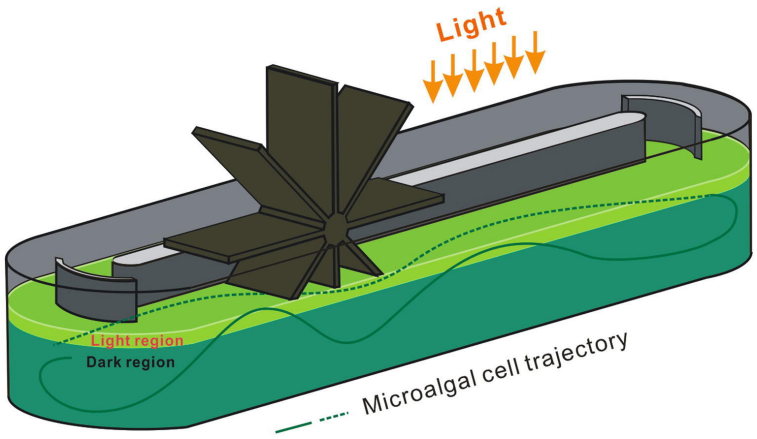

FIGURE 2.2: A schematic diagram of raceway pond, illustration from [27].

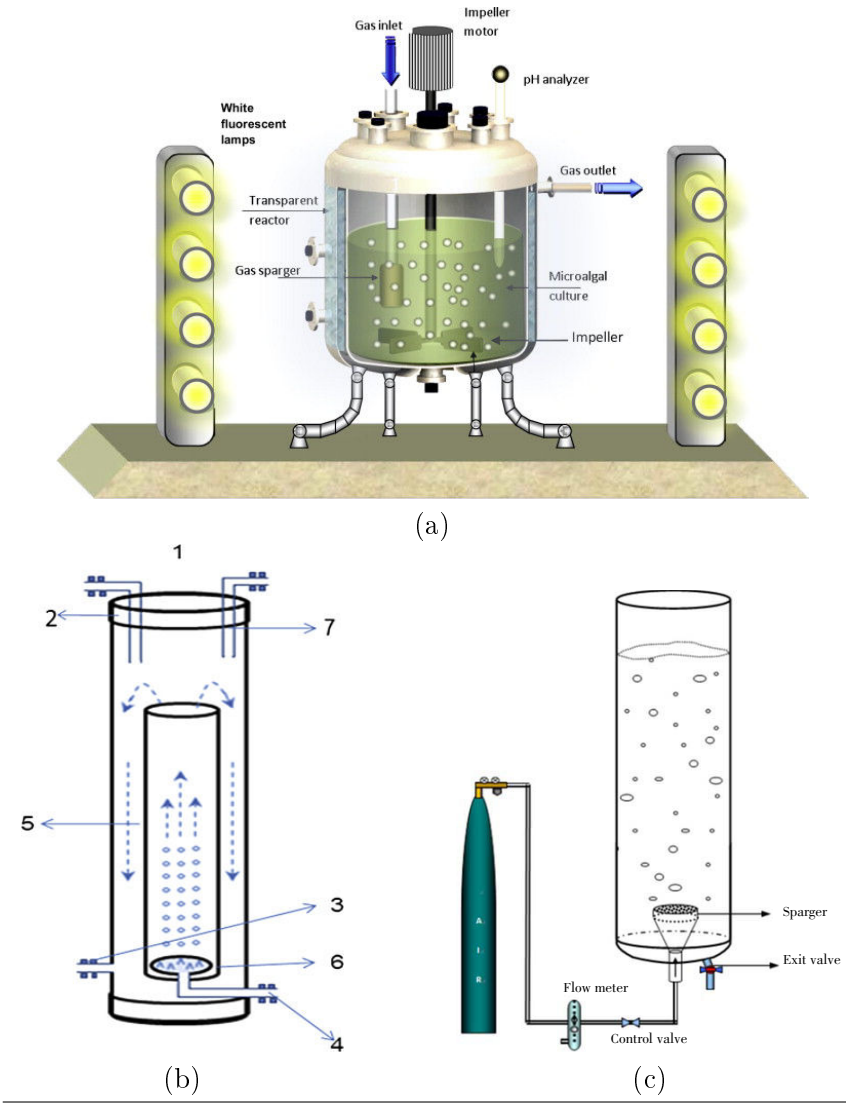

FIGURE 2.3: A schematic diagram of different types of photobioreactor: (a) stirred tank [28], (b) airlift [29], (c) bubble column [30].

TABLE 2.1: A comparison between open and closed microalgal cultivation systems, based on [32] [33] [34].

Parameters	Open systems	Closed systems
Costs	Relatively cheap	Expensive
Construction	Relatively simple	Sophisticated
Maintenance	Easy	Difficult
Occupied area	Large	Relatively small
Contamination risk	High	Low
Natural conditions dependence (weather, season, sunlight, etc.)	Absolute	Insignificant
Mixing	Poor	Good
Biomass productivity	Low	High
Cultivatable species	Limited	Nearly all
Environmental conditions control (temperature, pH, illumination, etc.)	Difficult	Possible

2.2 Photobioreactors

Between the two sorts of systems, closed systems, namely PBRs are more adopted for lab-use in view of their accurate control of parameters. Moreover, there are also various designs of PBRs, the main types are horizontal tubular, vertical column (including bubble column and airlift), flat-plate, and stirred tank, as shown in Fig. 2.4, they are compared in table 2.2 [31] [35] [36] [37].

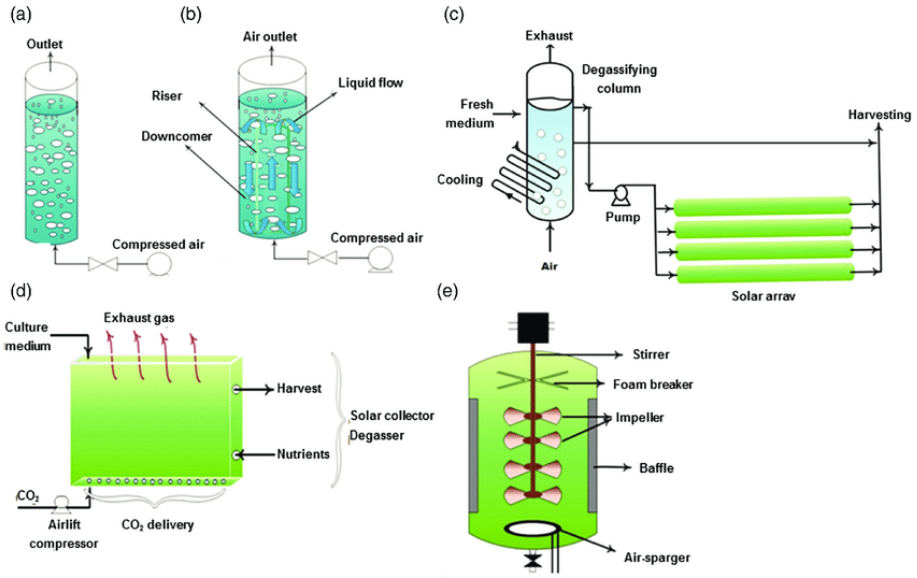

FIGURE 2.4: Various types of photobioreactors: (a) bubble column, (b) airlift, (c) horizontal tubular, (d) flat-plate, (e) stirred tank, illustration from [38].

TABLE 2.2: A comparison of various types of PBRs, based on [31] [35] [36] [37].

Reactor type	Advantages	Disadvantages
Tubular	• Relatively cheap • High surface to volume ratio • Low hydrodynamic stress • High biomass productivity • Suitable for outdoor cultivation	• Fouling • Large land space required • Accumulation of dissolved oxygen • Photoinhibition risk • Poor mass transfer
Vertical column	• High mass transfer • Good mixing • Low shear stress • Low photoinhibition	• Small illumination area • Expensive construction materials • Limited scale up
Flat-plate	• High surface to volume ratio • Small land space required • Good light path • Low oxygen accumulation	• Fouling • High hydrodynamic stress • Poor temperature regulation
Stirred tank	• High mass transfer • Simple design • Moderate biomass productivity	• Difficult to scale up • Small illumination area • High energy consumption

2.3 Gas-liquid flow

Gas-liquid flow plays a crucial role in the microalgal cultivation inside a PBR, since it is the gas-liquid flow that provides nearly all the essential nutrients and movements for cell growth. Specifically, the algal cells move with the liquid phase [39], consequently, they may be brought closer or further to the light source by the liquid phase. However, the distance between cells and light source has an important influence on the cell growth due to light attenuation over distance [40] [41]. Therefore, the flow pattern of the liquid phase strongly determines the efficiency of a PBR.

In fact, the flow patterns, or the velocity fields of both phases are still described by the Navier-Stokes equations [42] [43]. Besides, the two phases are often considered as incompressible, and the Navier-Stokes equations for incompressible flow is

$$\frac{\partial \vec{u}}{\partial t} + (\vec{u} \cdot \nabla)\vec{u} = -\frac{1}{\rho}\nabla p + \nu \nabla^2 \vec{u} + \vec{g} + \vec{f}_{\text{ext}}, \tag{2.1}$$

where p is the pressure, ν is the kinematic viscosity, $\vec{g}$ denotes gravity and $\vec{f}_{\text{ext}}$ represents other external forces, for example the surface tension on the gas-liquid interface. Equation (2.1) is a set of non-linear PDEs (Partial Differential Equations), it has no analytical solution for a general case. Therefore, CFD (Computational Fluid Dynamics) simulations and experimental tools, such as PIV (Particle Image Velocimetry), shadowgraphy, ect. are often applied to obtain the flow patterns.

CFD simulations of gas-liquid flow has been widely applied to the optimization of PBR designs in recent years, thanks to the rapid development of computers [44]. The main numerical models to simulate gas-liquid flow include Eulerian-Eulerian (E-E), Eulerian-Lagrangian (E-L) and Volume of Fluid (VOF). The Eulerian-Eulerian approach treats both continuous and dispersed phases as inter-penetrating continuum [45], thus the bubbles can not be well represented by this method. The Eulerian-Lagrangian approach treats the dispersed phase as spherical particles, therefore the bubbles can be tracked. VOF method is a numerical technique that can track two-fluid interface, thus the bubbles can be reproduced by this method.

Among these numerical models, there is not an absolutely best one, a better model is the one that can fulfill the research purpose with least cost. In the literature, Becker et al. investigated the velocity field of liquid phase in a rectangular bubble column by simple 2D E-E simulation, whose results were in agreement with experiments [46]. Pfleger et al. investigated the importance of 3D and turbulence model in E-E simulations, and they found that a 3D, turbulent E-E model agreed better with the experiments [47]. Rampure et al. adopted the E-E model to obtain the velocity field and gas hold-up at high gas velocity [48], as shown in Fig. 2.5, naturally, more sophisticated influence from bubbles was omitted in this research. Deen et al. applied large eddy simulation to a 3D E-E model, which captured more accurately the bubble plume movement. Buwa et al. applied single/multi-group model to 3D E-E simulations in order to represent bubble population [50]. Sanyal et al. coupled the E-E model with Population Balance Model (PBM) in order to model the significant variations in bubble size distribution due to bubble coalescence and breakup, and the PBM were solved by Classes Method (CM) and Quadrature Method of Moments (QMOM) [51]. Bannari et al. also coupled E-E model with PBM, but they carried out this coupling in an open source platform: OpenFOAM [52]. Sarkar et al. studied mixing in a stirred bioreactor by E-E model coupled with PBM [53]. Morchain et al. coupled 3D E-E model with population balance model of microalgae, which allows investigating the influence of concentration distribution on cell growth [54]. Gradov et al. coupled mass

transfer with 3D E-E model in ANSYS in order to simulate the cell cultivation in a industrial-scale bioreactor [55]. Rahimi et al. also added mass transfer into 3D E-E model, but it was carried out in open source OpenFOAM [56]. Saini et al. added radiative transfer into 3D E-E model [57]. Akhtar et al. applied VOF method to study the influence of superficial gas velocity on gas hold-up in a cylindrical bubble column [58], as shown in Fig. 2.6, yet the bubbles was not well resolved by the computer of that time. Besbes et al. investigated the velocity field in consideration of the influence of dispersed bubbles [45], as shown in Fig. 2.7, therefore E-L model was adopted in their research, yet without taking into account bubble breakup, coalescence and deformation. However, it is possible to add a breakup, coalescence and deformation kernel to this model, in order to handle those phenomena. E-L model was also applied to study the dynamics of bubble swarm in a bubble column [59], as shown in Fig. 2.8. Table 2.3 summarizes some representative studies that applies the different multiphase models, and an extended table including experimental investigations can be found in appendix A.

Meanwhile, the researchers also developed several experimental techniques to measure gas-liquid flow. First of all, to obtain the informations about the gas phase, i.e. bubbles, a shadowgraphy technique is often applied to capture the bubbles by high speed camera [60], as shown in Fig. 2.9. Although it is difficult to measure the physical quantities inside a bubble, a non-invasive infra-red technique was developed recently to measure the variation of gas concentration inside a bubble [61], as shown in Fig. 2.10. Second, the velocity field of the liquid phase is often measured by LDA (Laser Doppler Anemometry) or PIV technique. LDA is a point measurement technique, yet LDA has very high temporal resolution [62]. On the contrary, PIV allows a full-field measurement, but the temporal resolution is often limited by laser repetition rate and camera framing rate [63]. Besides, in some studies, conductivity probes are used to measure the gas hold-up, bubble velocity, etc. [48], the measuring principle is that the electrical conductivity varies with gas hold-up [64].

Both simulations and experiments demonstrated that gas-liquid flow has several flow patterns, for example bubbly flow, annular flow, slug flow, etc. [65], as shown in Fig. 2.11(a), and the flow patterns depend on the fluid properties, the pipe size, the flow rates, etc. [66]. Furthermore, several flow-pattern maps have also been proposed [67] [68] [69], as shown in Fig. 2.11(b). It should also be noted that the gas-liquid flow in most of PBRs is often a bubbly flow [70] [71] [72].

TABLE 2.3: Various studies that applies different multiphase models to investigate gas-liquid flow in a reactor.

Ref.	Objective	Multiphase model	Main conclusions	Strength & Limitation
[46] (1994)	To study the gas-liquid flow in a rectangular bubble column by both simulation and experiments. Experimental study for the influence of the type and location of the gas sparger on the hydrodynamics.	2D,Eulerian-Eulerian,laminar	The calculated liquid velocity field (vortices) agreed with the measured one qualitatively for non-coalescing bubbly flow regime	Strength: velocity field was investigated by both experiments and simulation. Limitation: the bubbles were not captured.
[47] (1999)	To obtain the knowledge of the hydrodynamics in chemical reactors and finally to improve the efficiency of the reactor.	2D vs 3D, Eulerian-Eulerian, laminar vs $k-\epsilon$ turbulence model, software: CFX4.2.	2D simulations were not able to show the periodic bubble hose movement observed in reality due to an over-prediction of the turbulent energy in the fluid. Laminar simulations did not reproduce the behavior of the test case, a turbulence model had to be considered. The turbulence dampened the dynamic of the bubble. 3D simulation with a sufficient fine resolution is necessary for accurate results.	Strength: 2D and 3D were compared, with and without turbulence model were compared. Limitation: the bubbles were not captured.

Ref.	Objective	Multiphase model	Main conclusions	Strength & Limitation
[49] (2001)	To apply large eddy simulation to the modeling of gas-liquid flow. To compare $k-\epsilon$ and large eddy turbulence model.	3D, Eulerian-Eulerian, $k-\epsilon$ vs large eddy turbulence model, software: CFX4.3.	LES simulation captured the strong transient movement of the bubble plume, which were observed in the experiment. Both the velocity and velocity fluctuations were in quantitative agreement with the measurement data.	Strength: Another turbulence model (LES) was used in this study. Limitation: absence of bubbles in simulations.
[50] (2002)	To understand better the mixing in bubble column reactor, we have to know better the dynamic characteristics. The effect of gas flow rate and sparger configuration on dynamics of gas-liquid flow were studied numerically and experimentally.	3D,Eulerian-Eulerian, single/multi-group models, software: FLUENT4.5.	The plume oscillation periods measured by wall pressure fluctuation were in good agreement with LDA measurements from literature. Bubble plume comprising of smaller bubbles led to faster oscillations than those comprising of larger bubbles. Coalescence is more pre-dominant than breakage because of lower turbulence. Lower axial upward averaged velocity resulted in longer residence time, lower bubble concentration.	Strength: flow pattern and plume oscillation periods were well investigated. Limitation: no explicit bubbles.
[51] (2005)	To model variations in the bubble size distribution due to bubble coalescence and breakup	2D, Eulerian-Eulerian coupled with Population Balance Model, solving the equations by Classes Method and (Direct) Quadrature Method of Moments, mixture $k-\epsilon$ turbulence model, software: FLUENT 6.0.	Even at low gas flow velocity, bubble size distribution changes. At least 12-18 classes are required to accurately model the entire range of bubble diameters in a typical bubble column. QMOM requires lower CPU time than CM.	Strength: bubble size distribution were studied with relatively less computing time. Limitation: no their own experiments.
[48] (2007)	To investigate bubble column reactor at high superficial velocity ($U_G \leq 0.4$).	3D,Eulerian-Eulerian, standard $k-\epsilon$ vs RNG $k-\epsilon$ turbulence model, software: FLUENT 6.2.	The conductivity probes were used to measure local time-averaged gas hold-up, bubble size distribution, bubble velocity distribution, and interfacial area distribution within the column. The CFD model showed good agreement with experimental data for time-averaged flow properties.	Strength: both experiments and simulations for gas hold-up, bubble velocity and bubble size. Limitation: only simulations for velocity field, no PIV measurements.
[58] (2007)	To study the influence of superficial gas velocity and distributors on gas hold-up and interfacial area. the authors have used VOF method, which was used for single bubble before, in this paper the VOF is used for a continuous bubble chain.	2D vs 3D, VOF, $k-\epsilon$ turbulence model, software: FLUENT 6.1.	Lower superficial gas velocity resulted in smaller bubbles and lower bubble rise velocity. Leading bubble was bigger than trailing bubble which might be due to less effects of wall and other surface forces on the trailing bubble. Bubble rise velocities in 2D were $\sim$ 30% lower than those in 3D, maybe because the 3D wake cannot be accurately modeled with 2D. 3D bubble rise velocity had a good agreement with Deckwer equation [73]. Same superficial gas velocity, smaller size distributor resulted in smaller bubbles and lower bubble rise velocity. Gas hold-up from 3D VOF simulation had good agreement with experiments.	Strength: VOF method is used for studying a bubble swarm. Limitation: more bubble behaviors should be detailed.
[52] (2008)	To predict bubble size distribution, volume fraction and velocity field taking account of bubble breakup and coalescence.	3D, Eulerian-Eulerian coupled with Population Balance Model, solved by Classes Method, dispersed $k-\epsilon$ turbulence model, software: OpenFOAM.	Good agreement between simulations and experiments. Eleven classes is a good compromise between reasonable computational effort and precision.	Strength: E-E and PBM are coupled in OpenFOAM, an open source software. Limitation: no experimental validation.
[59] (2011)	To simulate turbulent bubbly flow in complex systems by Eulerian-Lagrangian approach.	3D Eulerian-Lagrangian, LES turbulence model, bubble growth/collapse was modeled by the Rayleigh–Plesset equation, cylindrical and rectangular reactor.	The approach is suitable for simulation of subgrid bubble dynamics in complex flows without cavitation as well as small-scale bubbly cavitating flows. The approach is suitable for simulation of up to million bubbles in a turbulent flow.	Strength: a through numerical study of bubbly flow by Eulerian-Lagrangian model with bubble coalescence kernel. Limitation: there is no their own experimental validation.
[54] (2014)	To develop a CFD nodel coupled with a population balance model for the biological phase for lab-scale and industrial scale bioreactors.	3D Eulerian-Eulerian, coupled with population balance model, $k-\epsilon$ and LES turbulence model, cylindrical reactor (70 L and 70 m^3).	Cell growth was essentially sensitive to the volume average concentrations, whereas substrate assimilation was more sensitive to the spatial distribution of the substrates. The biological rates are not algebraically linked to the local concentrations.	Strength: the heterogeneity of cells in liquid phase was taken into account. Limitation: omitting the influence of bubble behaviors on the heterogeneity of cells.
[45] (2015)	To study the liquid phase velocity in homogeneous regime at low gas flow rates.	3D, Eulerian-Lagrangian, $k-\epsilon$ turbulence model, an average about 100 to 150 bubbles are present in the domain for the range of superficial gas velocities considered.	This article has mainly compared the measured and the simulated vertical and horizontal time-averaged liquid velocity profiles. At low gas flow rate (0.1 L/min), it had a reasonable agreement, but at relatively high gas flow rate (0.2 L/min), the discrepancy was larger.	Strength: velocity field was investigated by both PIV and 3D turbulent E-L simulation. Limitation: low gas flow rate, bubble coalescence or breakup was not taken into account.
[53] (2016)	To investigate mixing in a stirred bioreactor taking into account of bubble coalescence and breakup	3D, Eulerian-Eulerian coupled with Population Balance Model, $k-\epsilon$ turbulence model, software: FLUENT 14.	Near the impeller region, bubble size was smaller, and hence mass transfer was more effective. An optimum impeller was obtained to achieve maximum mixing without creating excessive cell damage.	Strength: mixing in a bioreactor was studied by a economic and effective way. Limitation: no their own experiments.

Ref.	Objective	Multiphase model	Main conclusions	Strength & Limitation
[55] (2018)	To develop a CFD model for simulating cell cultivation in an industrial-scale reactor.	3D Eulerian-Eulerian, taking into account mass transfer and bacterial activity, realizable $k-\epsilon$ turbulence model, software: ANSYS.	Concentration of species in simulations were in agreement with the one measured in a similar scale reactor. The CFD modeling was proved to be a reliable tool for design of industrial aerobic fermenters.	Strength: it studied most phenomena in a bioreactor, like mass transfer, fermentation kinetics, turbulence, etc. Limitation: hydrodynamics was not validated by experiments.
[56] (2018)	To investigate hydrodynamics, oxygen transfer and oxygen uptake in bubble-column and airlift bioreactors by simulations	3D Eulerian-Eulerian, cylindrical reactor, mass transfer and oxygen consumption were also added in the model, software: OpenFOAM.	The simulation result for gas holdup and gas-liquid mass transfer were in good agreement with experiments and engineering correlations from the bubble-column literature.	Strength: a thorough numerical study of bioreactor. Limitation: no their own experimental validation.
[57] (2018)	To investigate the influence of the impeller speed in revolutions and crossover frequency between the light and the dark zones on the growth of microalgae in a stirred tank photobioreactor by CFD.	3D Eulerian-Eulerian, cylindrical reactor, $k-\epsilon$ turbulence model, taking into account radiative transfer, software: ANSYS-Fluent.	The cell particles followed the fluid trajectory. The crossover frequency between the dark and light zones is critical for cell growth.	Strength: radiative transfer was coupled with CFD. Limitation: no enough experimental validation.

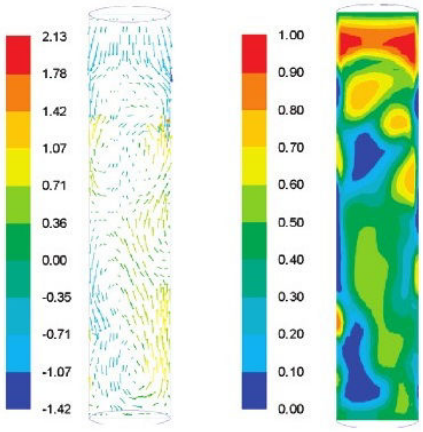

FIGURE 2.5: Velocity field and gas hold-up from Eulerian-Eulerian simulations, illustration from [48].

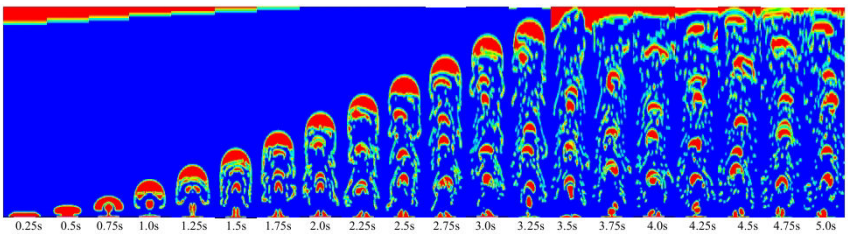

FIGURE 2.6: Simulation of gas-liquid flow by Volume of Fluid method, illustration from [58].

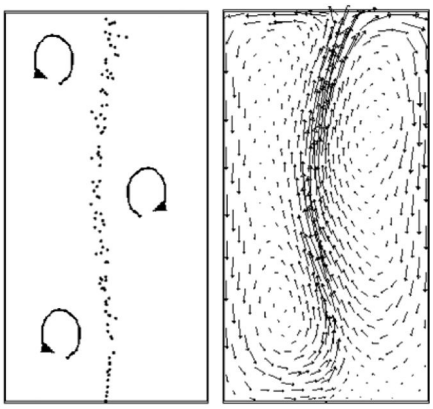

FIGURE 2.7: The velocity field of liquid phase from Eulerian-Lagrangian simulation, illustration from [45].

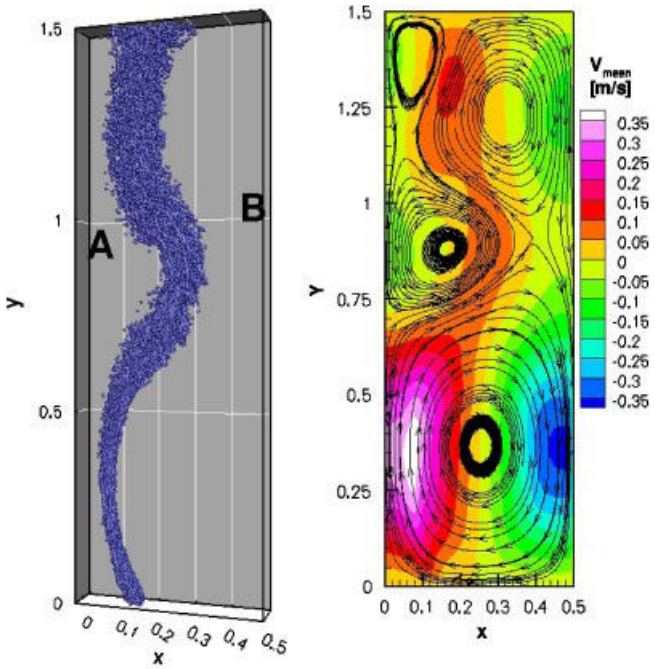

(a) Geometry (b) Avg. Velocity field

FIGURE 2.8: Bubble swarm simulated by Eulerian-Lagrangian model, illustration from [59].

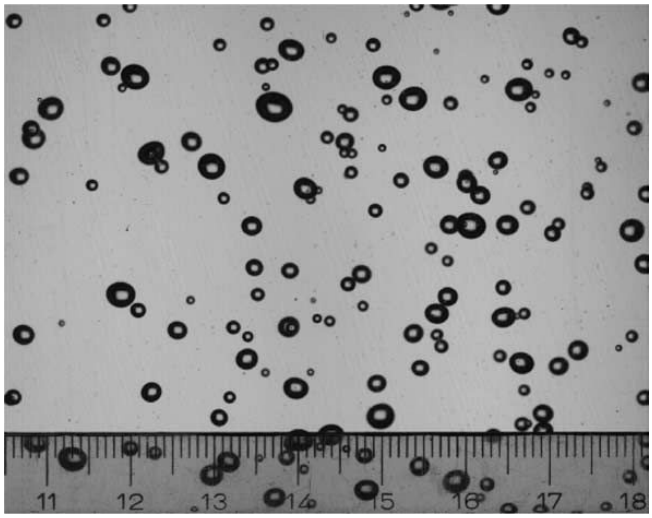

FIGURE 2.9: The bubbles captured by shadowgraphy technique, illustration from [74].

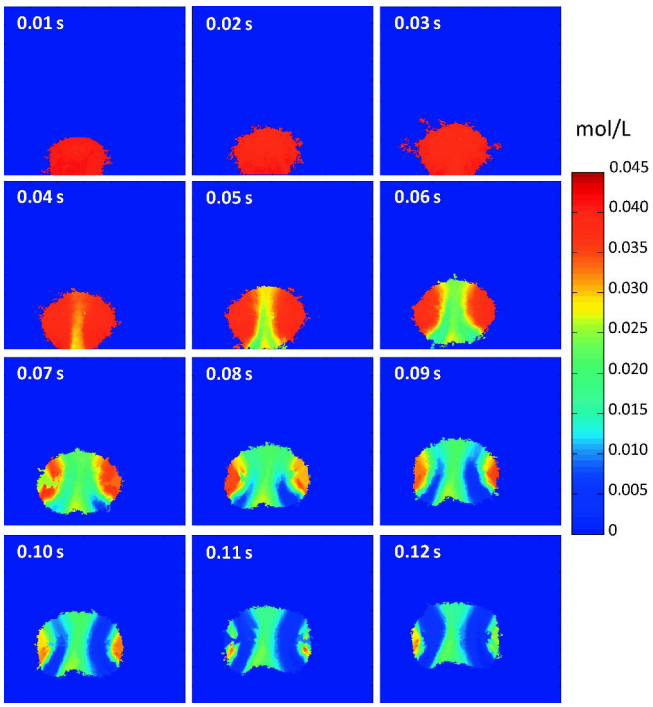

FIGURE 2.10: The gas concentration measured by infra-red technique, illustration from [61].

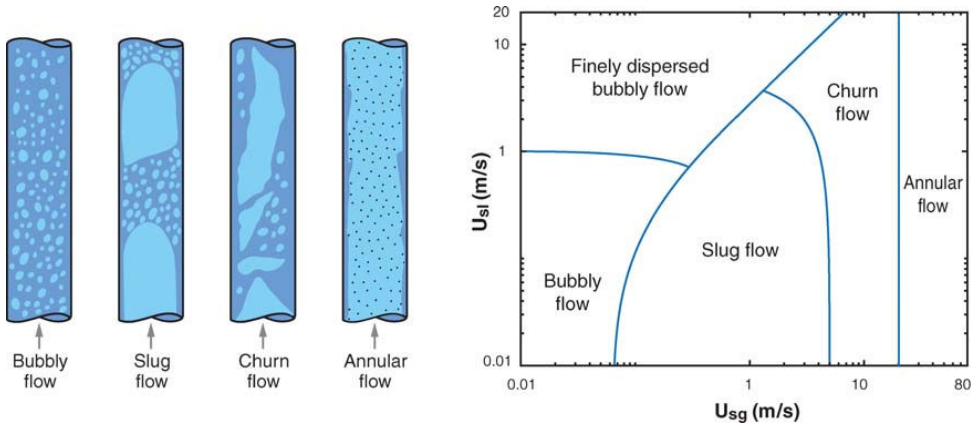

(a) (b)

FIGURE 2.11: (a) flow patterns, (b) flow-pattern map, illustration from [75].

2.4 Mass transfer

2.4.1 Mass transfer in a photobioreactor

Mass transfer for CO_2 from gas to a cell consists of several steps [76]:

1. transfer from a gas bubble to gas-liquid interface, mainly by convection and diffusion,
2. transport across a thin liquid boundary layer surrounding the gas bubble, usually by a combination of diffusion and convection,
3. transport through the liquid bulk, usually by convection or turbulence.
4. transport across another liquid boundary layer surrounding the cell, by diffusion,
5. transport across the cell envelope to the reaction site inside the cell, mainly by diffusion,

as shown in Fig. 2.12. In addition, mass transfer for products from cell to liquid follows the reverse route, except that the solid products transport only from cell to liquid.

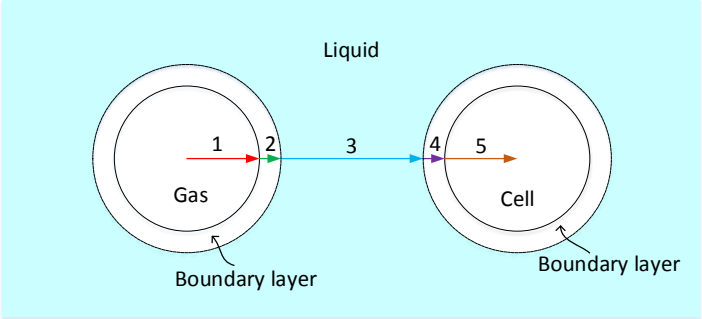

FIGURE 2.12: Chain of mass transfer in a photobioreactor.

2.4.2 Diffusion in a single phase

Several important steps of mass transfer are achieved by diffusion, which is the net movement of molecules or atoms from a region of high concentration (or high chemical potential) to a region of low concentration (or low chemical potential) [77] [78], as shown in Fig. 2.13.

To quantitatively study diffusion, a quantity called diffusion flux is defined as the mass transferred in one direction per unit area per unit time [79]:

$$J = \frac{M}{At}, \tag{2.2}$$

where A is area, t is time, M is mass:

$$M = \int_V C dV, \tag{2.3}$$

where C is mass concentration. Therefore, if mass concentration is time-independent, mass is also time-independent, so is J, which corresponds to so-called steady-state

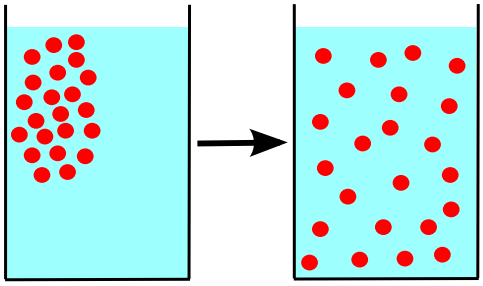

FIGURE 2.13: The process of diffusion, illustration from Wikipedia article *Diffusion*.

diffusion. Otherwise, if mass concentration is time-dependent, it is unsteady-state diffusion.

Steady-state diffusion is described by Fick's first laws of diffusion [79]: diffusion flux is proportional to the concentration gradient in the direction of mass transfer,

$$J = -\mathcal{D}\frac{dC}{dx}, \tag{2.4}$$

where $\mathcal{D}$ is diffusion coefficient or diffusivity, minus sign implies that mass is transferred from higher concentration to lower concentration. The inhomogeneity of mass concentration is the driving force for mass transfer.

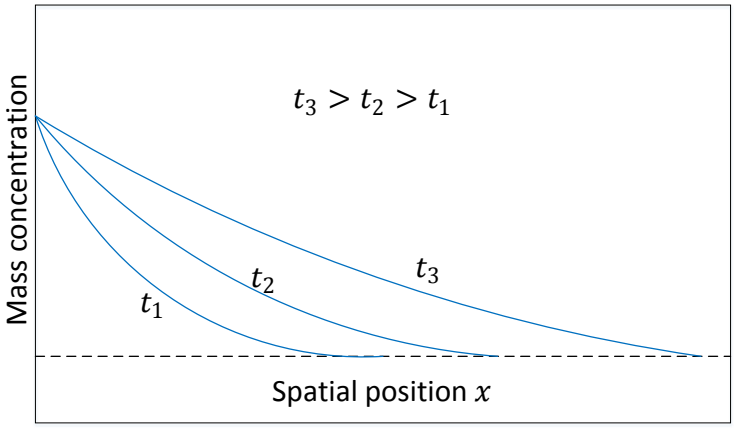

FIGURE 2.14: Unsteady state: concentration is dependent of time.

In unsteady state, concentration is a function of space and time, as shown in Fig. 2.14. And unsteady-state diffusion is described by Fick's second law of diffusion [79], which is deduced as follows. First, the change of concentration in the volume element illustrated in Fig. 2.15 is

$$\Delta C = \frac{\Delta M}{\Delta V} = \frac{J_1 A\Delta t - J_2 A\Delta t}{A\Delta x},$$

thus

$$\frac{\Delta C}{\Delta t} = -\frac{\Delta J}{\Delta x}, \tag{2.5}$$

in other words,

$$\frac{\partial C}{\partial t} = -\frac{\partial J}{\partial x}. \tag{2.6}$$

Substituting equation (2.4) into (2.6), we have

$$\frac{\partial C}{\partial t} = -\frac{\partial}{\partial x}\left(-\mathcal{D}\frac{\partial C}{\partial x}\right) = \mathcal{D}\frac{\partial^2 C}{\partial x^2}, \tag{2.7}$$

which is Fick's second law of diffusion, its three-dimensional form is

$$\frac{\partial C}{\partial t} = \mathcal{D}\nabla^2 C. \tag{2.8}$$

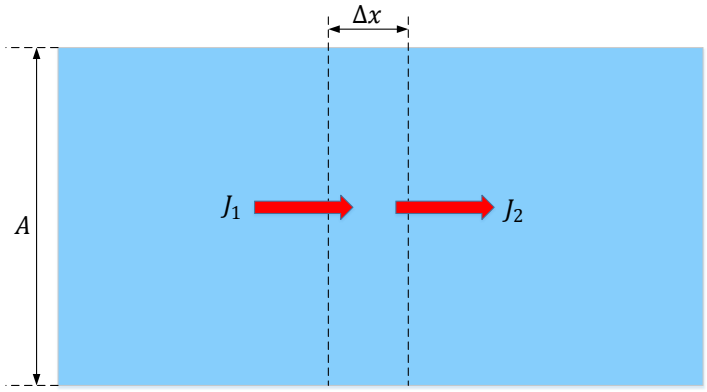

FIGURE 2.15: The volume element used to deduce Fick's second law of diffusion.

2.4.3 Diffusion between gas and liquid phases

When gas and liquid phases are in equilibrium, there is no net mass transfer between the two phases. This gas-liquid equilibrium is described by Henry's law, which says that the amount of dissolved gas is proportional to its partial pressure[1] [81]:

$$p = \lambda C_l, \tag{2.9}$$

where p is gas partial pressure (Pa), C is the concentration of dissolved gas in liquid (mol/m^3) and λ is Henry coefficient (Pa·m^3/mol). Besides, the ideal gas law is

$$p = \frac{n}{V}\mathscr{R}T = C_g\mathscr{R}T, \tag{2.10}$$

where C_g is the concentration of gas phase. Substituting equation (2.10) into equation (2.9), we have

$$C_g = HC_l, \tag{2.11}$$

where

$$H = \frac{\lambda}{\mathscr{R}T}, \tag{2.12}$$

[1] In a mixture of gases, each gas has a partial pressure which is the hypothetical pressure of that gas if it alone occupied the volume of the mixture at the same temperature [80].

known as the dimensionless Henry coefficient.

Henry's law holds only in gas-liquid equilibrium, if it is not equilibrium, there will be net mass transfer across the gas-liquid interface until equilibrium is reached again. To study the mass transfer between different phases due to non-equilibrium, Nernst proposed a film theory that assumes a stagnant film existing in one phase near the interface [82], as shown in Fig. 2.16. Note that this stagnant film is hypothetical since we do not really know the details of the velocity profile near the interface.

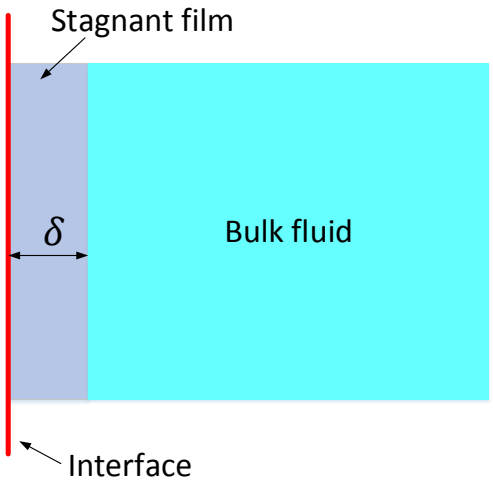

FIGURE 2.16: Nernst's film theory.

The molecules pass through this film by diffusion, which is described by Fick's law (2.4), thus mass flux across this film is

$$J = -\mathcal{D}\frac{C_b - C_i}{\delta}, \tag{2.13}$$

where C_b is the concentration in bulk fluid, C_i is the concentration at interface and δ is the thickness of this film. Moreover, equation (2.13) can be written as

$$J = k_c(C_b - C_i), \tag{2.14}$$

where

$$k_c = -\frac{\mathcal{D}}{\delta} \tag{2.15}$$

is known as mass transfer coefficient and its inverse $1/k_c$ is called resistance to mass transfer. Besides, Henry's law is applied to calculate C_i by assuming that the interface is in equilibrium. For example, if the bulk fluid in Fig. 2.16 is liquid phase and the other side is gas phase, according to equation (2.11), we have

$$C_i = \frac{C_g}{H}. \tag{2.16}$$

Nernst's film theory actually reduces gas-liquid mass transfer to one-phase-like mass transfer, since both film and bulk are in the same phase, the other phase appears only as part of interface by Henry's law. However, gas and liquid phases are often on

an equal footing, thus Lewis and Whitman proposed a two-film model in which films exist at both sides of interface [83], as shown in Fig. 2.17.

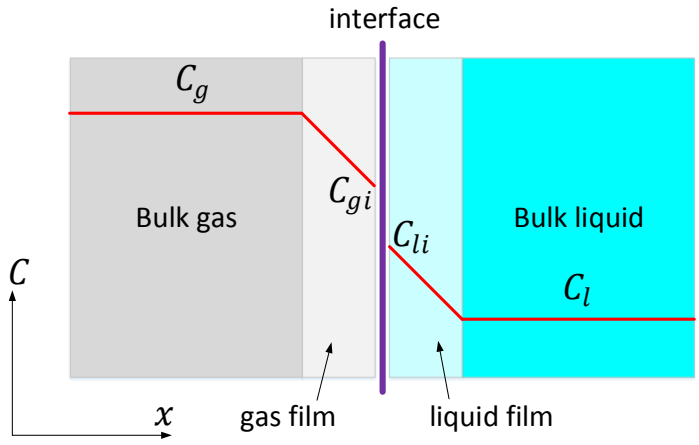

FIGURE 2.17: Two film model: films exist in both phases.

Still supposing that the interface is in equilibrium, indicating that Henry's law (2.11) holds, thus we have

$$C_{li} = \frac{C_{gi}}{H}, \tag{2.17}$$

where C_{li}, C_{gi} are the concentration at interface in liquid film, gas film, respectively. Furthermore, Fick's law holds in these two stagnant films:

$$J_l = k_l(C_l - C_{li}), \tag{2.18}$$
$$J_g = k_g(C_g - C_{gi}). \tag{2.19}$$

And the stagnant films are considered to be in steady state, thus flux through each film should be equal:

$$J_l = J_g = J. \tag{2.20}$$

Consequently, equations (2.18) (2.19) become

$$J = k_l(C_l - C_{li}), \tag{2.21}$$
$$J = k_g(C_g - C_{gi}). \tag{2.22}$$

However, concentrations at interface C_{li}, C_{gi} can not be measured. Therefore, two auxiliary equations are proposed:

$$J = K_l(C_l - C_l^*), \tag{2.23}$$
$$J = K_g(C_g^* - C_g), \tag{2.24}$$

where K_l, K_g are called overall mass transfer coefficients, C_l^*, C_g^* is the concentration of liquid/gas phase at interface that would be in equilibrium with the concentration of bulk gas/liquid, which satisfies Henry's law (2.11):

$$C_l^* = \frac{C_g}{H}, \tag{2.25}$$
$$C_g^* = HC_l. \tag{2.26}$$

Substituting equation (2.25) (2.26) into (2.23) (2.24), we obtain the relation between the two overall mass transfer coefficients:

$$K_l = HK_g. \tag{2.27}$$

In other words, K_l and K_g are physically equivalent, they only have the difference of a constant coefficient, thus either one can be used to describe mass transfer, here we choose K_l to represent the overall mass transfer coefficient.

Subsequently, equation (2.23) is rewritten as

$$J = K_l[(C_l - C_{li}) + (C_{li} - C_l^*)], \tag{2.28}$$

substituting equations (2.17) (2.25) into (2.28), we have

$$J = K_l \left[(C_l - C_{li}) + \frac{(C_{gi} - C_g)}{H}\right]. \tag{2.29}$$

Substituting equations (2.21) (2.22) into (2.29), we obtain

$$J = K_l \left[\frac{J}{k_l} + \frac{J}{Hk_g}\right], \tag{2.30}$$

J is canceled, we finally have

$$\frac{1}{K_l} = \frac{1}{k_l} + \frac{1}{Hk_g}. \tag{2.31}$$

In equation (2.31), $1/K_l$ represents total resistance to mass transfer, which is determined by liquid film resistance ($1/k_l$), gas film resistance ($1/k_g$) and solubility ($1/H$). For highly soluble gases (low H), such as ammonia, it satisfies $1/Hk_g \gg 1/k_l$, consequently, the liquid film resistance can be ignored. On the other hand, for poorly soluble gases (high H), such oxygen, satisfying $1/k_l \gg 1/Hk_g$, thus gas film resistance can be ignored.

2.5 Light

Microalgal growth is a photosynthetic process, by which light energy is absorbed by chlorophyll, an organic pigment contained in organisms, subsequently carbon dioxide and water are converted into carbohydrates and oxygen [84]. Moreover, photosynthesis is traditionally divided into two parts, the light-dependent reactions, or light reactions and light-independent reactions, or dark reactions, as shown in Fig. 2.18 [85]. The light reactions require light to produce organic energy molecules, ATP and NADPH. The dark reactions utilize energy molecules (ATP/NADPH) to fix carbon dioxide into carbohydrates. Therefore, photosynthesis is essentially the conversion from light energy into chemical energy, in other words, the whole process is driven by light energy. In consideration of the importance of light in microalgal growth, it is necessary to understand how light influences lab-scale or even industrial-scale microalgal cultivation [86].

The relation between light intensity and photosynthesis of cells is classically depicted by a so-called light-response curve, also known as PI (Photosynthesis-Irradiance) curve, as shown in Fig. 2.19 [87]. Scientists first studied PI curve of a population of cells, then individual cells only recently [88] [89] [90] [91]. The curve includes three distinct stages:

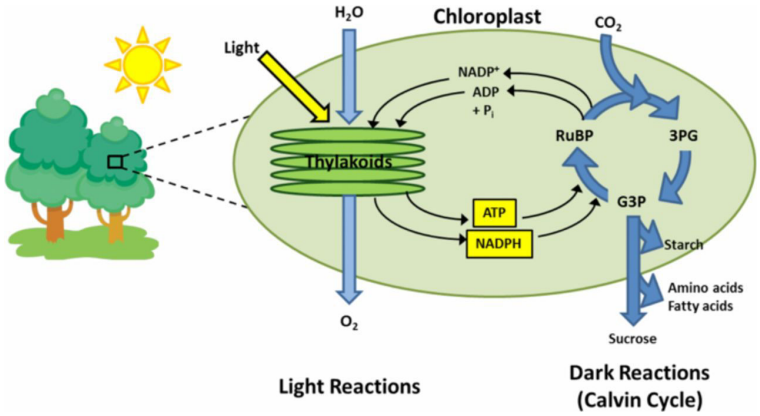

FIGURE 2.18: Photosynthesis: light reactions and dark reactions, illustration from [85].

1. Light-limited: rate of photosynthesis linearly increases with light intensity at relatively low light intensity.
2. Light-saturated: the curve reached a plateau, accordingly rate of photosynthesis obtains its maximum value.
3. Light-inhibited: rate of photosynthesis decreases with light intensity, known as photo-inhibition of synthesis.

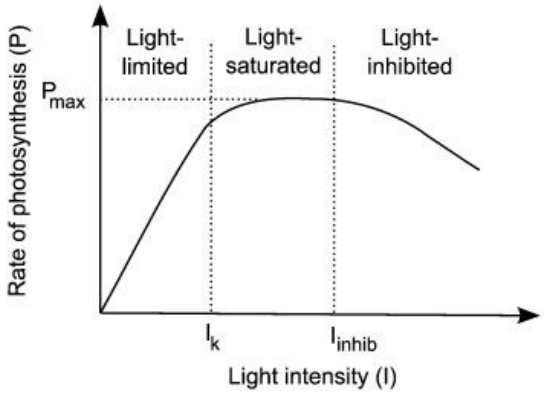

FIGURE 2.19: Light-response curve: the relation between rate of photosynthesis and light intensity, illustration from [87].

Subsequently, several mathematical models are constructed to fit the light-response curve when light intensity is limited, naturally photo-inhibition is not accounted for in such model. For example, Monod-like models describe the light-response curve as [87]

$$\mathcal{P} = \mathcal{P}_{\max} \frac{I}{I_k + I}, \tag{2.32}$$

where $\mathcal{P}$ is the rate of photosynthesis, $\mathcal{P}_{\max}$ is the maximum rate of synthesis, I is the light intensity, I_k represents saturation irradiance.

Based on the study of light-response for individual cells, researchers established the light-response model for the whole culture including a large amount of cells. The first category of models is simple, the light-response curve is considered to be homogeneous

in the entire culture by assuming that each single cell receives exactly the same light intensity. Therefore, the first type of models for the entire culture is the same as the model for individual cells, i.e. (2.32).

However, the assumption in the previous models is very ideal, since light intensity may vary from place to place due to the light-blocking by dense cells and light attenuation with distance. Therefore, the second category of models is established by considering the nonuniform distribution of light in the reactor. In such model, light intensity is a function of cell concentration and position, which is often described by the Beer-Lambert law

$$I(x) = I_0 e^{-\mu_a x}, \tag{2.33}$$

where x is the distance from system surface to the cell in question, I_0 is the incident light intensity, μ_a is the attenuation coefficient depending on the cell concentration and position. Incidentally, the attenuation coefficient μ_a also depends on the absorbing ability of chlorophyll and other light-absorbing molecules [92].

Equation (2.33) implies that the irradiance is rapidly attenuated in the course of penetrating the culture medium, consequently, cells are likely to be in dark reactions when they are in the center of a photobioreactor. Therefore, by mixing of a photobioreactor, the microalgal cells may experience a shorter light/dark cycle, which may reduce light-inhibition [87]. The effect of short light/dark cycle is not included in the second type of models, thus the third category of models is established to include this effect [93] [94] [95] [96] [97]. Such model is accomplished by recording photosynthesis of every single cell, which is driven by liquid flow to move between the light and dark zones. Subsequently, the rate of photosynthesis of the entire culture is calculated by summing all the rates of photosynthesis of single cell. However, such model runs the risk of overfitting, since there are too many parameters [98].

2.6 Cell growth

This thesis mainly studied the physics inside a photobioreactor, i.e. the phenomena of gas-liquid flow. However, the biological process will come shortly into the subject in future once the study of physics is finished. Therefore, we give the theoretical minimum that describes cell growth to facilitate the future studies [99] [100]. To construct a mathematical model of cell growth in a reactor, we need the equations that describe:

1. Kinetic models of cell growth
2. Mass balance for different boundary conditions
3. Heterogeneity of cell growth

2.6.1 Kinetic model

First of all, to study cell growth, we need to know the rate of cell growth r_X, which was found to be proportional to the present cell concentration:

$$r_X = \mu X, \tag{2.34}$$

where μ is the specific growth rate, its unit is s^{-1}, and X is the mass concentration of cells in a reactor, its unit is generally g/L.

Therefore, a model for the specific growth rate is necessary in order to calculate the rate of cell growth from equation (2.34). At low substrate concentration, supposing

that there is only one limiting substrate, the specific growth rate is described by the Monod model

$$\mu = \mu_{\max} \frac{S}{K_s + S}, \tag{2.35}$$

where $\mu_{\max}$ is the maximum specific growth rate, K_s is the substrate concentration when the specific growth rate is $0.5\mu_{\max}$, S is the substrate concentration. $\mu_{\max}$, K_s are constants, influenced by temperature, pH..., they also depend on the type of the micro-organism, for example K_s of *Aerobacter aerogenes* is 8 mg/L, and the K_s of *Aspergillus oryzae* is 5 mg/L.

There are certainly other models for cell growth, as shown in table 2.4 [100].

TABLE 2.4: Different kinetic models [100]

Model name	Kinetic expression
Tessier	$\mu = \mu_{\max}(1 - e^{-c_s/K_s})$
Moser	$\mu = \mu_{\max} \frac{c_s^n}{c_s^n + K_s}$
Contois	$\mu = \mu_{\max} \frac{c_s}{c_s + K_s x}$
Blackman	$\mu = \begin{cases} \mu_{\max} \frac{c_s}{2K_s}; & c_s \leq 2K_s \\ \mu_{\max}; & c_s \geq 2K_s \end{cases}$
Logistic law	$\mu = \mu_{max}(1 - \frac{x}{K_x})$

2.6.2 Mass balance

Cells, substrates, products, they all respect mass balance, a general form of mass balance is

$$\text{Inlet} + \text{Production} + \text{Initial State} = \text{Outlet} + \text{Consumption} + \text{Final State}, \tag{2.36}$$

which can also be rewritten as

$$\text{Inlet} + \text{Production} = \text{Outlet} + \text{Consumption} + \text{Accumulation}, \tag{2.37}$$

where

$$\text{Accumulation} = \text{Final State} - \text{Initial State}. \tag{2.38}$$

For the discussions in this section 2.6.2, μ is assumed to be uniform in the whole reactor, for which a perfectly-mixed reactor will be a necessary but not sufficient condition, since μ also depends on the age of cell, etc.

Mass balance of cells

The cells have their specific form of mass balance, for example, the *production* in (2.37) becomes the *birth* of cells, the *consumption* is actually the *death* of cells, and the *accumulation* is now the net variation of cells in the bioreactor. Supposing that the volume of bioreactor is a constant V_0, thus the mass balance of cells per unit time is

$$Q_{\text{in}} X_{\text{in}} + r_X V_0 = Q_{\text{out}} X_{\text{out}} + r_D V_0 + \frac{d(V_0 X)}{dt}, \tag{2.39}$$

where Q is the volumetric flow rate of liquid, X is the mass concentration of cells, r_X, r_D are the rate of cellular birth and death, respectively.

To simplify the problem, assuming that there is no cellular death in the following discussions. With this assumption, we apply different boundary conditions to equation (2.39):

B.C. 1, a continuous open reactor, which indicates:

$$Q_{\text{in}} = Q_{\text{out}} = Q, \tag{2.40}$$

thus (2.39) is now

$$QX_{\text{in}} + r_X V_0 = QX_{\text{out}} + \frac{d(V_0 X)}{dt}. \tag{2.41}$$

More constraints can be added to (2.40):

B.C. 1.1, a perfectly-mixed reactor, whose concentration of cells does not depend on the space: $X(\cancel{x,y,z},t)$. Therefore, if we take some samples from different zones of the reactor, the concentration of the samples has no difference with the one in the reactor, which implies

$$X_{\text{out}} = X, \tag{2.42}$$

consequently, (2.41) becomes

$$QX_{\text{in}} + r_X V_0 = QX + V_0 \frac{dX}{dt}. \tag{2.43}$$

B.C. 1.2, still a perfectly-mixed reactor, yet only substrate, no cell in the inlet flow, which is often the case, in other words

$$X_{\text{in}} = 0, \tag{2.44}$$

thus (2.43) becomes

$$r_X - \frac{Q}{V} X = \frac{dX}{dt}. \tag{2.45}$$

Together with equation (2.34), we have

$$(\mu - D)X = \frac{dX}{dt} \tag{2.46}$$

where

$$D = \frac{Q}{V_0}, \tag{2.47}$$

known as dilution rate. Equation (2.46) simply signifies that the increase of cells (μ) minus the removal of cells (D) equals to the variation of cells (dX).

B.C. 2, a closed reactor(batch), which satisfies

$$Q_{\text{in}} = Q_{\text{out}} = 0, \tag{2.48}$$

in this case, (2.39) becomes

$$r_X = \frac{dX}{dt}. \tag{2.49}$$

Mass balance of substrate

The substrate also has its own version of (2.37), for example, the biological reaction dose not produce substrate, on the contrary, it only consumes substrate. Therefore,

the *production* for substrate is 0, the mass balance of substrate per unit time is

$$Q_{\text{in}}S_{\text{in}} = Q_{\text{out}}S_{\text{out}} + r_S V_0 + \frac{d(V_0 S)}{dt}, \tag{2.50}$$

where S is the mass concentration of substrate, r_S is the consumption rate of substrate concentration, which satisfies

$$r_S = \frac{r_X}{Y_{XS}}, \tag{2.51}$$

where Y_{XS} is the yield coefficient. Equation (2.51) just means that the reaction consumes a certain amount of substrate, and produces some cells accordingly.

For different boundary conditions:

B.C. 1, a continuous and perfectly-mixed reactor, which implies (2.40) and

$$S_{\text{out}} = S, \tag{2.52}$$

together with (2.51), mass balance (2.50) becomes

$$QS_{\text{in}} = QS + \frac{r_X}{Y_{XS}} + V_0\frac{dS}{dt}. \tag{2.53}$$

Subsequently, dividing equation (2.53) by V_0, then applying (2.47) (2.34), we have

$$(S_{\text{in}} - S)D - \frac{\mu X}{Y_{XS}} = \frac{dS}{dt}, \tag{2.54}$$

which means that the net inflow of substrate minus the consumption of substrate equals the variation of substrate. Besides, when the inlet flow satisfies

$$S_{\text{in}} > S, \tag{2.55}$$

the substrate can make the cells flourish.

B.C. 2, a closed perfectly-mixed system, satisfying (2.48), thus (2.50) becomes

$$\frac{dS}{dt} = -\frac{\mu X}{Y_{XS}}, \tag{2.56}$$

substituting equation (2.49), we have

$$\frac{dS}{dX} = -\frac{1}{Y_{XS}}, \tag{2.57}$$

in other words,

$$X - X_0 = S_0 - Y_{XS}S. \tag{2.58}$$

With equations (2.56) (2.58) (2.35), we obtain

$$\frac{dS}{dt} = -\frac{\mu_{\max}S}{K_s + S}\left(\frac{S_0}{Y_{XS}} - S\right). \tag{2.59}$$

A typical solution of (2.59) is shown in Fig. 2.20, where we can observe that the substrate will be exhausted, which is expected to take place for a closed system.

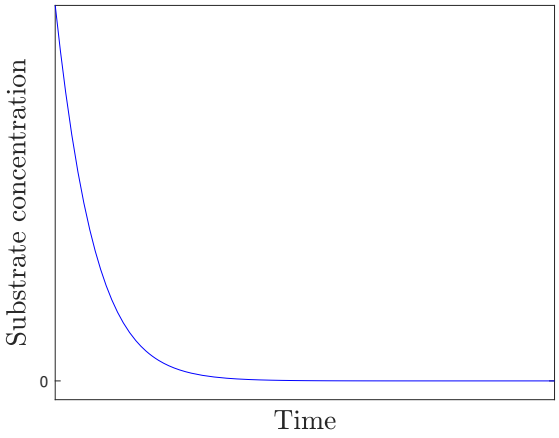

FIGURE 2.20: The variation of substrate concentration with time in a closed system.

Mass balance of products

For products, the *production* in (2.37) is just the metabolic products, and the *consumption* is 0. Normally, there is no products in inlet flow, i.e.

$$P_{\text{in}} = 0. \tag{2.60}$$

Therefore, the mass balance of products per unit time is

$$r_P V_0 = Q_{\text{out}} P_{\text{out}} + \frac{d(PV_0)}{dt}, \tag{2.61}$$

where P is the mass concentration of products, r_P is the formation rate of products, similar to (2.51), it satisfies

$$r_P = Y_{PX} r_X. \tag{2.62}$$

For different boundary conditions:

B.C. 1, a continuous and perfectly-mixed reactor, which indicates (2.40) and

$$P_{\text{out}} = P. \tag{2.63}$$

Consequently, (2.61) becomes

$$r_P - DP = \frac{dP}{dt}, \tag{2.64}$$

substituting (2.62), we have

$$Y_{PX} r_X - DP = \frac{dP}{dt}, \tag{2.65}$$

whose significance is similar to the one of (2.46).

B.C. 2, a closed system, implying (2.48), thus (2.61) becomes

$$Y_{PX} r_X = \frac{dP}{dt}. \tag{2.66}$$

2.6.3 Population balance equation

In the previous discussions, μ is assumed to be uniform in the whole reactor, which is often not the case in reality, since the cells may grow with different velocities in different zones. Therefore, in this section 2.6.3, we will discuss the method to describe the heterogeneity in a reactor, namely the *population balance equation* (PBE) [101] [102] [103].

The PBE is closely connected to the continuity equation that describes a conserved quantity, since the cell number is also a conserved quantity with a source term (net birth/death of cells). For a conserved quantity ψ, the general continuity equation is

$$\frac{\partial \rho}{\partial t} + \nabla \cdot (\rho \vec{u}) = s, \tag{2.67}$$

where ρ is ψ per unit volume, $\vec{u}$ is the velocity field and s is the variation of ψ per unit volume per unit time, i.e. the net source term.

For cell number, equation (2.67) has the form

$$\frac{\partial n_c}{\partial t} + \nabla_\xi \cdot (n_c \vec{\zeta}) + \nabla_r \cdot (n_c \vec{u}) = s_c, \tag{2.68}$$

where ξ denotes the coordinates of internal space in which heterogeneity takes place, for example cell size, specific growth rate, etc.; r is the coordinates of the three-dimensional physical space; n_c is the cell number per physical volume per internal volume; s_c is the variation of cell number per physical volume per internal volume; $\vec{\zeta}$ is the "velocity" in the internal space:

$$\vec{\zeta}(t) = \frac{d\vec{\xi}}{dt}. \tag{2.69}$$

Also noticing that the total cell number is

$$\mathcal{N}(t) = \int_{\Omega_\xi} \int_{\Omega_r} n_c d\xi dr, \tag{2.70}$$

and the cell number density in the physical space is

$$\chi(r,t) = \int_{\Omega_\xi} n_c d\xi. \tag{2.71}$$

Subsequently, we integrate (2.68) on the internal space:

$$\frac{\partial}{\partial t}\left(\int_{\Omega_\xi} n_c d\xi\right) + \nabla_\xi \cdot \left(\vec{\zeta} \int_{\Omega_\xi} n_c d\xi\right) + \nabla_r \cdot \left(\vec{u} \int_{\Omega_\xi} n_c d\xi\right) = \int_{\Omega_\xi} s_c d\xi. \tag{2.72}$$

By substituting (2.71) into (2.72), we have

$$\frac{\partial \chi}{\partial t} + \nabla_\xi \cdot (\vec{\zeta}\chi) + \underbrace{\nabla_r \cdot (\vec{u}\chi)}_{\text{convective}} = \epsilon(r,t), \tag{2.73}$$

where ϵ is the variation of cell number per physical volume. Equation (2.73) is the population balance equation for cell growth. In the numerical approach of equation (2.73), the convective term in the physical space is handled by the CFD modeling, thus we just need to treat the rest part, i.e. the transport equation in the internal

space:

$$\frac{\partial \chi}{\partial t} + \nabla_\xi \cdot (\vec{\zeta}\chi) = \epsilon(r,t). \tag{2.74}$$

Furthermore, the specific growth rate is often considered as the only internal coordinate, consequently, transport equation (2.74) becomes

$$\frac{\partial \chi}{\partial t} + \frac{\partial}{\partial \mu}\left(\frac{\partial \mu}{\partial t}\chi\right) = \epsilon(r,t), \tag{2.75}$$

which signifies that the cells are transported by the "velocity" field in μ-space. The "velocity" at a μ-point, or the direction of cell transport at this point, is still determined by the Monod equation (2.35): cells will "flow" into a larger/smaller neighboring μ-point if the actual point is smaller/larger than μ_{env}, the optimal specific growth rate in the same medium [101].

To numerically solve equation (2.75), the μ-space with the range of $[0, \mu_{\max}]$ is often divided into N subspaces, as shown in Fig. 2.21. Therefore, μ in the i-th subspace is

$$\mu_i = \frac{i-1}{N-1}\mu_{\max}, \quad i = 1, 2, \cdots, N, \tag{2.76}$$

and μ_i is a constant in each subspace. Consequently, cells will "flow" from i-th subspace to $(i+1)$-th subspace for $\mu_i < \mu_{\text{env}}$, and also from i-th subspace to $(i-1)$-th subspace for $\mu_i > \mu_{\text{env}}$, as shown in Fig. 2.22.

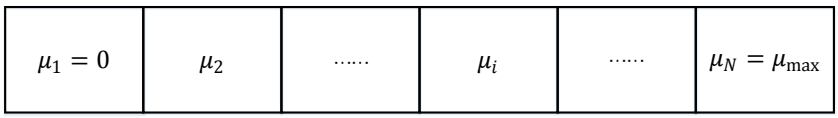

FIGURE 2.21: μ-space is divided into N subspaces, each subspace holds a constant μ_i, and μ_i increases from left to right in the illustration.

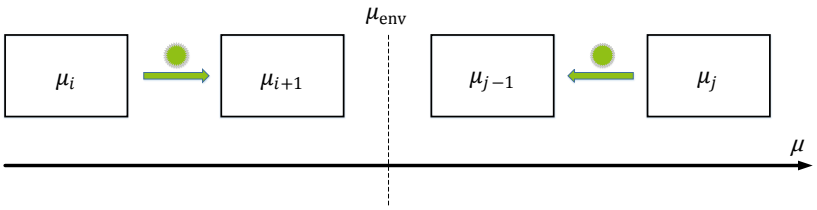

FIGURE 2.22: For $\mu_i < \mu_{\text{env}}$, cells "flow" in μ-space from smaller μ_i to larger μ_{i+1}; for $\mu_j > \mu_{\text{env}}$, cells are "transported" in μ-space from larger μ_j to smaller μ_{j-1}.

Furthermore, to numerically solve the entire equation (2.73), Morchain et al. have coupled CFD modeling that handles the gas-liquid flow, a kinetic rate expression that describes biological reactions and a population balance modeling that accounts for biological adaptation to local concentration gradients [54]. This approach is particularly interesting when one would like to scale-up an aerated fermenter, since the concentration gradients is more likely to occur at large scale. In addition, such approach also

provides an explanation for the decreased performances of poorly mixed industrial bioreactors.

Besides, ξ in equation (2.73) may include more than one internal coordinate. For example, Quedeville et al. have recently investigated two internal coordinates, the specific growth rate and the cell length of rod shaped cells [104], in order to uncouple growth in mass (controlled by the rate of anabolic reactions) and growth in number (controlled by the cell division kernel) when the equilibrium between a cell population and its environment is disrupted.

2.7 The influence of bubble behaviors on cell growth

Both physical and biological phenomena are discussed above, and they are all indispensable for the proper functioning of a photobioreactor. However, these two kinds of phenomena may not be bystanders to each other: an interaction between them may take place in the meantime.

For example, it has been observed that the bubble behaviors can affect microalgal growth and give rise to a heterogeneous microalgal distribution in a bubble column photobioreactor [105]: the microalgal cells are absorbed on the bubble surface, and cells are carried upwards by the bubbles, as shown in Fig. 2.23. Consequently, microalgae tend to accumulate at the top of the culture. Further, smaller orifice size and higher gas flow rate produce more serious bubble carrying, which accordingly results in more accumulations of cells at the top of culture. In addition, the reverse effect also exists [106]: the aggregation of microalgal cells on the surface of CO_2 bubbles resulted in an easier bubble detachment in the microalgal suspension than in pure water, since the aggregation on bubble surface may have reduced the gas-liquid surface tension. Besides, bubble formation at sparger can result in shear stress, which will finally lead to cell damage and death [107]. And small bubbles are more damaging than large bubbles [108].

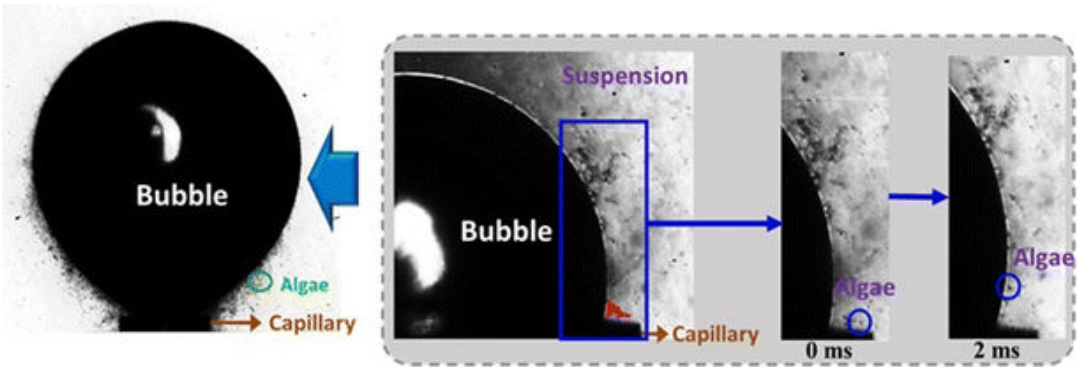

FIGURE 2.23: Microalgae are absorbed on the bubble surface, illustration from [106].

Also, T. Coward et al. have generated a large population of small bubbles to cultivate microalgaes, and the influence of bubble size and rise velocity on microalgal harvesting is significant [109]. Besides, bubble behaviors can also impact gas-liquid mass transfer, which also influences the cell growth. For example, the mass transfer coefficient was observed to be proportional to the bubble diameter [110]. Also, a small flow rate with large bubbles may be more efficient for CO_2 mass transfer since the shearing forces are reduced [111].

2.8 The complete model

A complete model is required in order to study all the phenomena and interactions between them in a photobioractor, and the complete model can be achieved by coupling different sub-models, as shown in Fig. 2.24. Starting with gas-liquid flow: hydrodynamics, gas concentration and pressure in bubbles, bubble behaviors including bubble volume and shape are obtained by means of experimental methods like shadowgraphy, PIV, and the numerical tool proposed and validated in this thesis. Taking hydrodynamic information as input, plus Lagrangian tracer properties, Lagrangian transport model yields cell concentration, cell trajectories, etc. Similarly, the transport model of scalar existing mainly in liquid gives pH, temperature and scalar concentration at different moments and positions.

Meanwhile, using gas pressure, gas concentration in bubbles, bubble volume, bubble shape, temperature, etc. as inputs, gas-liquid mass transfer model gives the amount of CO_2 transferred from bubbles into liquid. And the amount of the dissolved CO_2 becomes an input for the dissolved gas scalar transport model, which provides dissolved CO_2 concentration at different moments and positions.

On the other hand, with cell concentration, cell trajectories, liquid scalar concentration obtained from previous models, plus external illumination conditions, light model yields light received by moving individual cells [112]. Subsequently, rate of photosynthesis is obtained according to photosynthesis-irradiance relationship.

Finally, all the outputs from the previous models serve as inputs for the cell growth model, which gives temporal evolution and spatial distribution of physical states such as position and biological states like cell growth rate of microalgae in a photobioreactor.

In chapter 5, we will attempt to carry out some important sub-models, and also introduce other essential kernels of the complete model in more details.

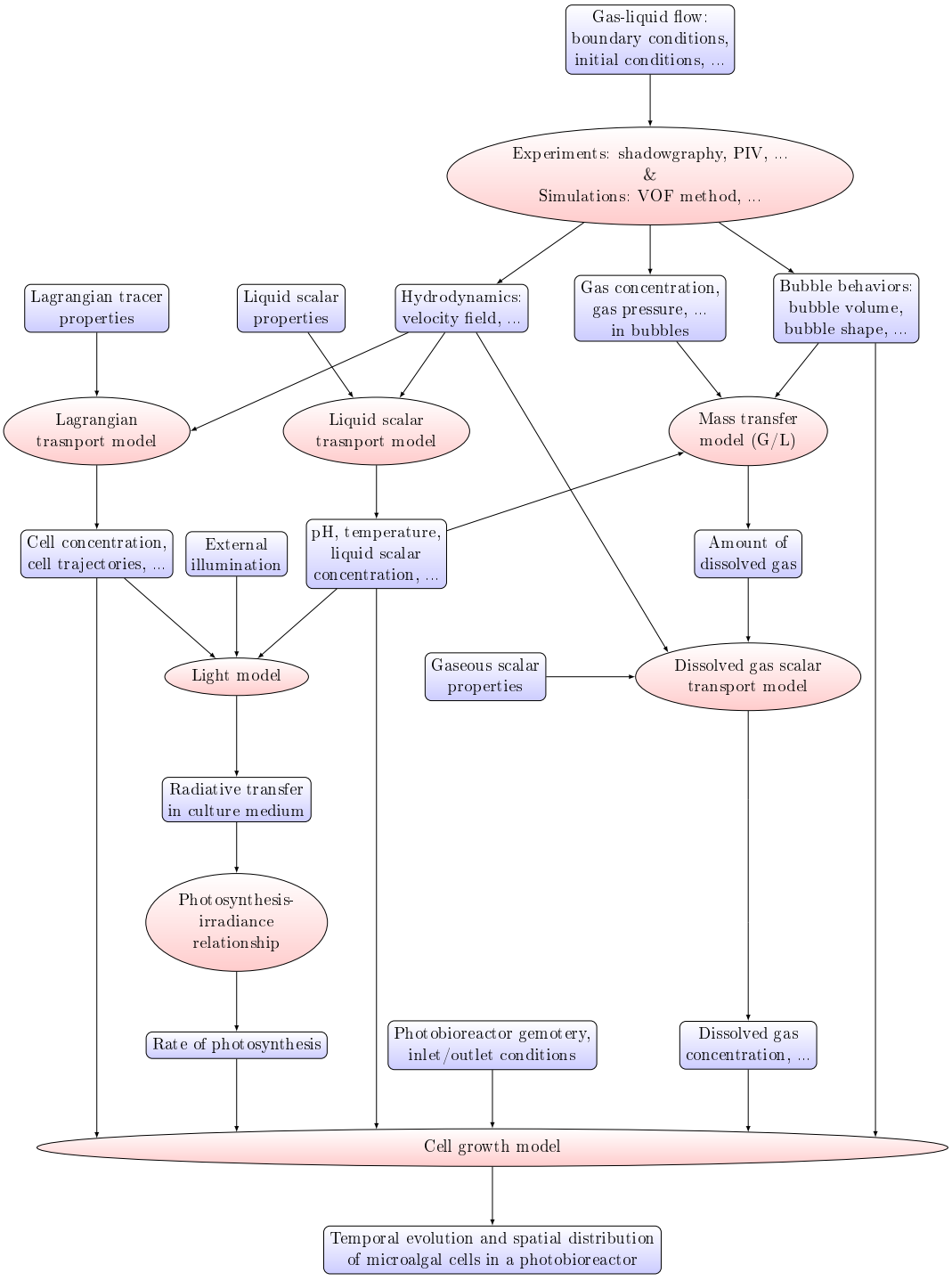

FIGURE 2.24: The basic structure of the complete model. An ellipse represents a model handling a specific problem, and a rectangle represents the inputs required by a model, or outputs yielded from a model.

2.9 Objectives

In this chapter, we have reviewed all the essential studies of physical, biological, and physical-biological coupling phenomena in a photobioreactor, which presents the great complexity of a photobioreactor. In light of the literature review, we found that bubble behaviors have important influence on the productivity of a photobioreactor: on one hand, bubbles are the driving source of the gas-liquid flow, on the other hand, they also have direct impact on cell growth. However, to our knowledge, a thorough study of bubble behaviors (volume and shape evolution) in a bubble column photobioreactor was not often reported in existing literature.

Therefore, this PhD project aims to investigate how bubbles behave under different flow conditions by both experimental and numerical methods to gain more insight into the complicated phenomena in a photobioreactor. On the basis of literature review, shadowgraphy is adopted as the experimental method. Also, VOF method seems to be a more suitable numerical method for this project, since, among the mainstream multiphase models, only VOF can generate bubbles and represent bubble shape evolution without additional kernels.

In order to achieve the aim of the project, following research objectives are pursued in this thesis:

1. To design and manufacture a lab-scale photobioreactor suitable for the present and follow-up studies:
    - The reactor uses glass as the material of its wall in order that the camera can clearly capture the bubbles.
    - The reactor is a rectangular one in order to avoid possible image distortion.
    - The reactor size is relatively small for less energy demand, easier maintenance, less complicated phenomena. Besides, a small reactor also benefits the later simulation, since a smaller numerical domain requires less computing time.
    - The reactor has multiple nozzles, which allows searching for the optimal injecting configuration for the microalgal cultivation.
2. To set up a photography system that can accurately capture bubbles, specially the profile of a bubble:
    - A shadowgraphy technique is applied to construct the system.
    - A monochromatic light source is used in order to avoid unwanted optical effect on the images.
    - The camera has enough field of view so that a whole bubble can be captured by the camera.
    - The camera can take images at a relatively high frame rate in order to record enough images for a fast-moving bubble.
3. To process the images to obtain the information of bubble behaviors:
    - Image Processing Toolbox™ in Matlab is applied to process the images since it possesses many practical functions and it is more efficient in processing many images.
    - The images are binarized and useless elements in the images are removed.
    - Bubble volume, bubble shape and bubbling frequency are calculated from the processed images.

4. To simulate bubble behaviors by a numerical tool:
    - OpenFOAM is chosen to be the basic tool, whose solver for two-phase flow is based on VOF method.
    - The robustness of the numerical tool is investigated by literature review.
    - The basic numerical parameters are determined through less computation-intensive simulations, such as 2D simulations.
    - 3D bubbles are simulated by the numerical tool and the relevant information of bubble behaviors are also obtained through post-processing.
5. To compare bubble behaviors from simulations with those from experiments:
    - The ability of the numerical tool to simulate bubbles is validated through this comparison.
    - The working range of the numerical tool for a specific numerical domain is also known.
6. Several points are discussed as perspectives:
    - The time required to arrive at a quasi-steady state of two-phase flow.
    - The mixing time of a scalar tracer.
    - The transport of microalgal cells in the liquid.
    - The radiative transfer equation and its numerical solutions for calculating the light field throughout the reactor.
    - The complete model that couples different phenomena.

Chapter 3

Experimental study

In this chapter, bubble behaviors were investigated in a lab-scale photobioreactor under different bubbling conditions using experimental methods. We first gave a preliminary calculation about influence of wettability on bubble formation and detachment. Then, bubbles were captured into digital images by applying a shadowgraphy technique. Subsequently, the original images were processed in order to filter out the less important informations and only keep the critical elements. Finally, several bubbling features, such as bubbling frequency, bubble volume, and bubble shape evolution, were extracted from the processed images. In addition, the Matlab code for image processing and analysis is available in appendix B.

3.1 Preliminary reflection on the role of wettability in bubble formation and detachment

For a bubbly flow, one of the most essential phenomena is bubble formation and detachment at a submerged orifice, since it initially determines bubble volume, bubble velocity and other important parameters of bubbly flow. The previous researchers have observed that bubble growth has two regimes [113]: when the gas flow rate is smaller than the critical value, the bubble volume is insensitive to the flow rate, on the contrary, the bubble volume increases with the flow rate when the gas flow rate is greater than the critical value.

In this section 3.1, we focus on the regime of low gas flow rate where bubble formation is a quasi-static process, therefore it is possible to have an analytical approach for the process. In this regime, it has been found that wettability of the orifice material is an important factor that influences bubble volume [114]. The model of impact of wettablity is similar to the one of gas flow rate: wettability has no influence on bubble volume for small contact angles, however, bubble volume starts to increase dramatically with contact angle once contact angle exceeds a critical value. In existing literature, this phenomenon has been explained qualitatively [114] [115]. Nevertheless, we propose an alternative explanation by considering both capillary force and adhesive force, finally we obtain a formula to quantitatively describe this phenomenon [116].

As mentioned before, bubble growth at low gas flow rate is regarded as a quasi-static process. Based on this hypothesis, we consider the situation where a bubble does not spread over the horizontal solid surface, as shown in Fig. 3.1. In this case, a three-phase contact line is located at the orifice edge. Thus, referring to Fig. 3.1(a), the surface stresses in equilibrium satisfy [117]

$$\sigma_{LS}^{H} = -\sigma_{GL}\cos\alpha \tag{3.1}$$

$$\sigma_{GS}^{V} = \sigma_{GL}\sin\alpha, \tag{3.2}$$

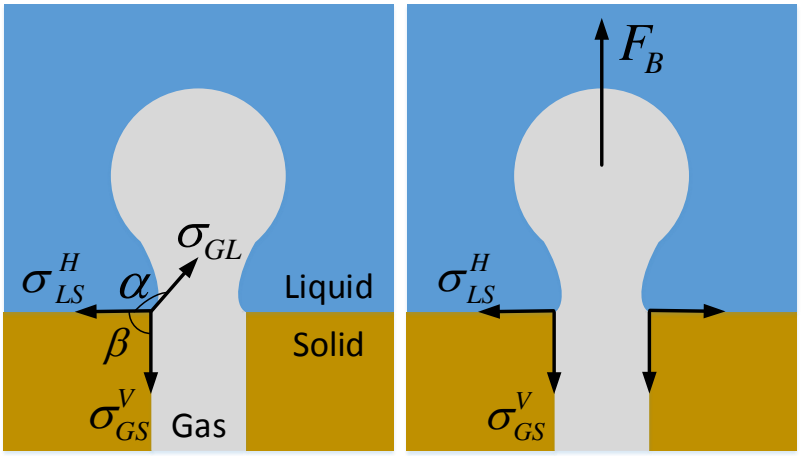

(a) (b)

FIGURE 3.1: A bubble that does not spread beyond the orifice edge. (a) The three surface stresses σ act on the triple line located at the orifice edge. α, β are the angles between the interfaces, and β is set to be $\pi/2$. (b) The gas-liquid surface stress σ_{GL} does not appear in the forces acting on the bubble as a whole. The liquid-solid surface stress σ_{LS}^{H} pulls the bubble outwards and may make the bubble spread over the horizontal surface. The gas-solid surface stress σ_{GS}^{V} resists the buoyancy force F_B.

where α is the contact angle, H, V stand for "Horizontal", "Vertical", respectively, and G, L, S stand for "Gas", "Liquid", "Solid", respectively. In this way, σ_{GL} is the gas-liquid surface stress, σ_{LS}^{H} is the surface stress at the horizontal liquid-solid interface and σ_{GS}^{V} is the surface stress at the vertical gas-solid interface.

In addition, both of the horizontal and vertical solid surfaces satisfy

$$\sigma_{GL}\cos\theta_H = \sigma_{GS}^{H} - \sigma_{LS}^{H} \tag{3.3}$$

$$\sigma_{GL}\cos\theta_V = \sigma_{GS}^{V} - \sigma_{LS}^{V}, \tag{3.4}$$

known as the Young equation, where θ is the contact angle on a perfectly flat and rigid surface. This angle also characterizes wettability of the surface: a small θ implies high wettabilty (hydrophilic surface), whereas a large θ signifies low wettability (hydrophobic surface). If the material of the horizontal and vertical surfaces is identical, from equations (3.1) (3.2) (3.3) (3.4), we have

$$\cos\left(\alpha - \frac{\pi}{4}\right) = \frac{\sqrt{2}}{2}\cos\theta, \tag{3.5}$$

where $\theta = \theta_H = \theta_V$. As a result, we obtain $\pi/2 < \alpha < \pi$ for $0 < \theta < \pi$, this obtuse contact angle α is observed during bubble pinch-off [118] [119]. In other words, the initial stage of bubble pinch-off, namely the formation of the bubble neck, may result from the fact that the three phases seek to attain equilibrium at the orifice edge.

Fig. 3.1(b) shows the forces acting on the bubble as a whole. Inside a tube, the capillary force per unit length is [120]

$$f_C = \sigma_{GS} - \sigma_{LS}. \tag{3.6}$$

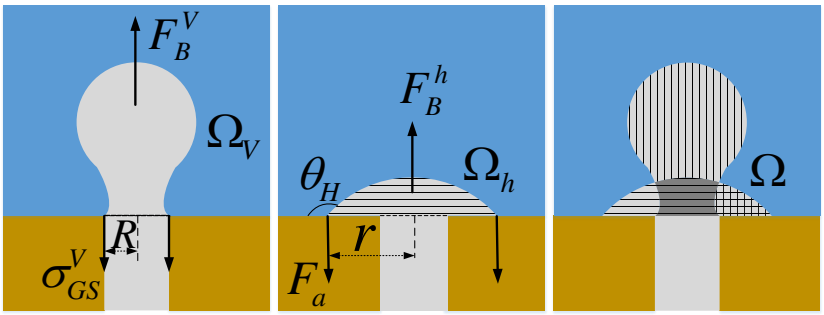

FIGURE 3.2: The method for calculating bubble volume. (a) Ω_V is the maximum gas volume that can be supported by the vertical gas-solid interface. (b) During bubble spreading, Ω_h is the gas volume that is held by the horizontal solid surface, its maximum value is $\Omega_H = (\Omega_h)_{\max}$. (c) The bubble volume is considered as a sum of the previous two maximum volumes. Noticing that the overlapping volume represented by the dark region appears twice in the total volume, thus the theoretical bubble volume is a little larger than the actual one.

However, liquid-solid surface stress is a horizontal force at the orifice edge, naturally, it does not appear in the vertical capillary force. Therefore, the capillary force per unit length at orifice edge is the gas-solid surface stress

$$f_C = \sigma_{GS}^V, \tag{3.7}$$

which resists the buoyancy force F_B. During bubble detachment, upward F_B and downward σ_{GS}^V will stretch the bubble to break up, which may explain the observations from Keim et al. [121]: "In the last stages (of bubble pinch-off), the air appears to tear instead of pinch". In horizontal direction, σ_{LS}^H tends to pull the bubble onto the horizontal solid surface. Consequently, the bubble may spread over the horizontal surface. In this case, the buoyancy force is met with resistance mainly from two forces: the surface stress σ_{GS}^V provided by the vertical gas-solid interface, and the adhesive force F_a provided by the horizontal gas-solid interface.

To calculate the maximum bubble volume Ω, we artificially divide the bubble into two parts. A "vertical part" that is supported by the vertical gas-solid interface, and a "horizontal part" that adheres to the horizontal solid surface, as shown in Fig. 3.2(a) and (b), respectively. Thus

$$\Omega = \Omega_V + (\Omega_h)_{\max}, \tag{3.8}$$

where Ω_V is the maximum volume of the vertical part, Ω_h is the volume of the horizontal part, its maximum value is $\Omega_H = (\Omega_h)_{\max}$.

By equating the corresponding buoyancy force

$$F_B^V = \Omega_V \Delta\rho g, \tag{3.9}$$

and the capillary force

$$F_C = 2\pi R \sigma_{GS}^V, \tag{3.10}$$

we estimate Ω_V in Fig. 3.2(a) as

$$\Omega_V = \frac{2\pi\sigma_{GS}^V}{\Delta\rho g}R, \tag{3.11}$$

where R is the orifice radius, $\Delta\rho$ is the density difference between liquid and gas, g is the gravitational acceleration.

To simplify the algebraic calculations, we suppose that the horizontal part has the shape of a spherical cap, thus

$$\Omega_h(\theta_H, r) = \frac{\pi(2 + 3\cos\theta_H - \cos^3\theta_H)r^3}{3\sin^3\theta_H}, \tag{3.12}$$

where r is the spreading radius on the horizontal surface, as shown in Fig. 3.2(b). The corresponding buoyancy force is

$$F_B^h = \Delta\rho g\Omega_h. \tag{3.13}$$

It is worth mentioning that the actual horizontal part is the spherical cap subtracted by the overlapping part, which is represented by the dark region in Fig. 3.2(c). In other words, the actual Ω_h depends on the orifice radius R. Nevertheless, the spherical cap can approximately represent the horizontal part by assuming that R is small enough, namely the overlapping volume is negligible.

To pull the horizontal part away from the horizontal surface, the required work per unit area is

$$\mathfrak{w}_H = \sigma_{GL} + \sigma_{LS}^H - \sigma_{GS}^H, \tag{3.14}$$

known as the work of adhesion [122]. Substituting equation (3.3) into (3.14), we have

$$\mathfrak{w}_H = \sigma_{GL}(1 - \cos\theta_H). \tag{3.15}$$

It has been found that the adhesive force per unit length is proportional to the work of adhesion [123] [124], hence we obtain

$$F_a = 2\pi r k_a \sigma_{GL}(1 - \cos\theta_H), \tag{3.16}$$

where k_a is a dimensionless coefficient relating the adhesive force to the work of adhesion.

To evaluate the competition between the corresponding buoyancy force and the adhesive force, we calculate the difference

$$\delta = F_B^h - F_a = c\left[r^3 - \frac{6k_a\sigma_{GL}}{\Delta\rho g}\frac{(1 - \cos\theta_H)\sin^3\theta_H}{2 + 3\cos\theta_H - \cos^3\theta_H}r\right], \tag{3.17}$$

where

$$c = \frac{\pi(2 + 3\cos\theta_H - \cos^3\theta_H)\Delta\rho g}{3\sin^3\theta_H} \tag{3.18}$$

is positive for $0 < \theta_H < \pi$. We plot δ versus r in Fig. 3.3, and we observe that for $r < r_{\max}$ the buoyancy force is smaller than the adhesive force. The bubble continues to spread over the horizontal surface until the spreading radius attains its maximum value

$$r_{\max} = \sqrt{\frac{6k_a\sigma_{GL}}{\Delta\rho g}\frac{(1 - \cos\theta_H)\sin^3\theta_H}{2 + 3\cos\theta_H - \cos^3\theta_H}}, \tag{3.19}$$

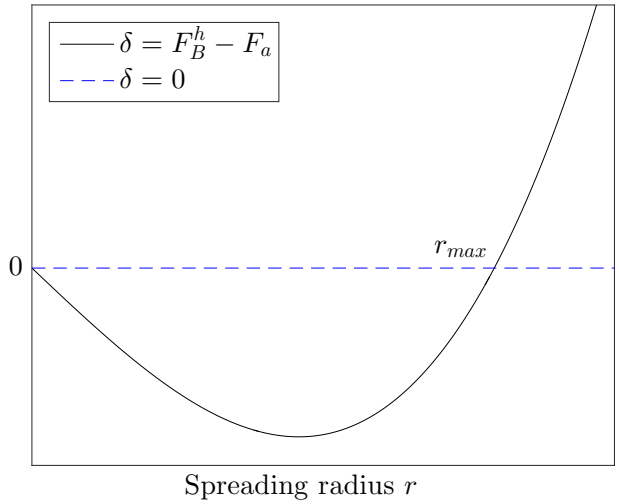

FIGURE 3.3: The difference between the buoyancy force F_B^h and the adhesive force F_a versus spreading radius r for the horizontal part. $\delta = 0$ indicates $F_B^h = F_a$, $\delta < 0$ indicates $F_B^h < F_a$. And $r_{\max}$ is the maximum spreading radius.

at which the buoyancy force F_B^h equals the adhesive force F_a. For $r > r_{\max}$, the buoyancy force is larger than the adhesive force, thus the bubble starts detaching.

The maximum volume of the horizontal part is estimated as $\Omega_H = \Omega_h(r_{\max})$ for a fixed θ_H. Together with equations (3.12) (3.19), we obtain

$$\Omega_H = \frac{\pi}{3}\left(\frac{6k_a\sigma_{GL}}{\Delta\rho g}\right)^{\frac{3}{2}}\left[\frac{(1-\cos\theta_H)^3\sin^3\theta_H}{2+3\cos\theta_H-\cos^3\theta_H}\right]^{\frac{1}{2}}, \tag{3.20}$$

a function of wettability of the horizontal surface θ_H. To analyze equation (3.20), we write

$$\varepsilon = \frac{\pi}{3}\left(\frac{6k_a\sigma_{GL}}{\Delta\rho g}\right)^{\frac{3}{2}}. \tag{3.21}$$

Subsequently, we plot Ω_H for different ε in Fig. 3.4, and we observe that Ω_H has a flat tail where Ω_H approximately equals zero. Furthermore, the size of this tail is determined by the parameter ε, a larger ε implies a smaller tail. In the context of bubble formation, this flat tail indicates that a bubble can hardly spread over a relatively hydrophilic surface (with small θ_H). Lin et al. [114] have described this phenomenon as: "the bubble growth on the hydrophobic surface is no longer taking place at the edge of the orifice as the case of hydrophilic surfaces. In fact, the contact base of the bubble started to spread beyond the orifice edge as the orifice surface became more hydrophobic."

Substituting equations (3.11) and (3.20) into (3.8), we obtain the total volume

$$\Omega(R,\theta_H) = \frac{2\pi\sigma_{GS}^V}{\Delta\rho g}R + \frac{\pi}{3}\left(\frac{6k_a\sigma_{GL}}{\Delta\rho g}\right)^{\frac{3}{2}}\left[\frac{(1-\cos\theta_H)^3\sin^3\theta_H}{2+3\cos\theta_H-\cos^3\theta_H}\right]^{\frac{1}{2}}. \tag{3.22}$$

Equation (3.22) explains the following observations made by Lin et al. [114]: "For orifice contact angles (θ_H) between 0 and 55°, the bubble volume is determined by

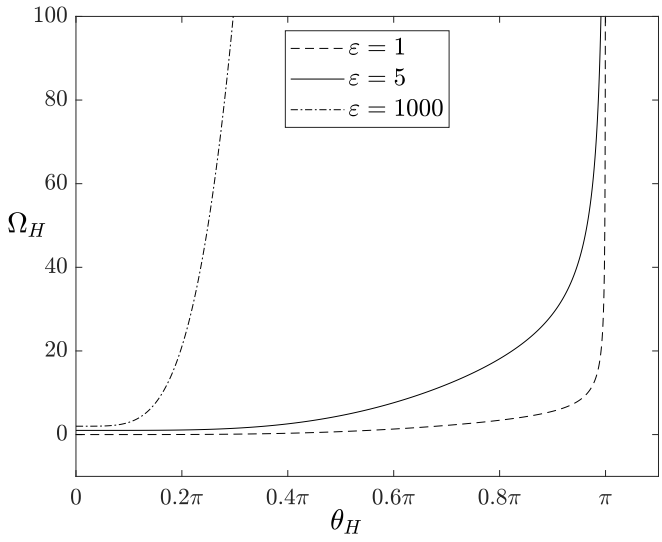

FIGURE 3.4: Function $\Omega_H = \varepsilon \left[\frac{(1-\cos\theta_H)^3 \sin^3\theta_H}{2+3\cos\theta_H - \cos^3\theta_H}\right]^{\frac{1}{2}}$ for different κ. The curves are slightly staggered for better visibility of the flat tails.

the orifice diameter and independent of the magnitude of the contact angle. However, when the orifice contact angle exceeds the threshold value of 55°, the air bubble volume increased with increasing contact angle due to spreading of the contact base."

Inspecting equation (3.22) we see that for small θ_H, the total volume is determined by the orifice size in the first term of equation (3.22), since the second term almost vanishes. Once the second term leaves the flat tail, it increases dramatically with increasing θ_H. As a result, the contribution of the second term to the total volume will become much larger than the first term, naturally, as described by [114]: "the contribution of orifice size to the bubble volume is important only for hydrophilic surfaces.".

Similar experimental results, i.e. constant bubble volume on hydrophilic surface and dramatical increase of bubble volume with contact angle on hydrophobic surface, are also been reported in other articles [125] [126] [127] [128] [129], they can also be explained in principle by equation (3.22).

Fig. 3.5 shows a quantitative comparison between the theoretical prediction (3.22) and the experimental data from Lin et al. [114]. The constants in equation (3.22) are determined as follows. We assume that Ω_H is 0 for $\theta_H = 0.087$, consequently, from $\Omega(R_1 = 0.275\ mm, \theta_H = 0.087) = 11\ \text{mm}^3$, we have

$$\frac{2\pi\sigma_{GS}^{V}}{\Delta\rho g} \approx 40\ \text{mm}^2. \tag{3.23}$$

This is a constant, since the material of the vertical solid surface does not change in the experiments. Subsequently, by minimizing the mean square error between the theoretical and experimental values for $R_1 = 0.275$ mm, we obtain

$$\frac{\pi}{3}\left(\frac{6k_a\sigma_{GL}}{\Delta\rho g}\right)^{\frac{3}{2}} \approx 85.4\ \text{mm}^3, \tag{3.24}$$

which is also invariant by assuming that k_a in equation (3.16) is a constant. With the

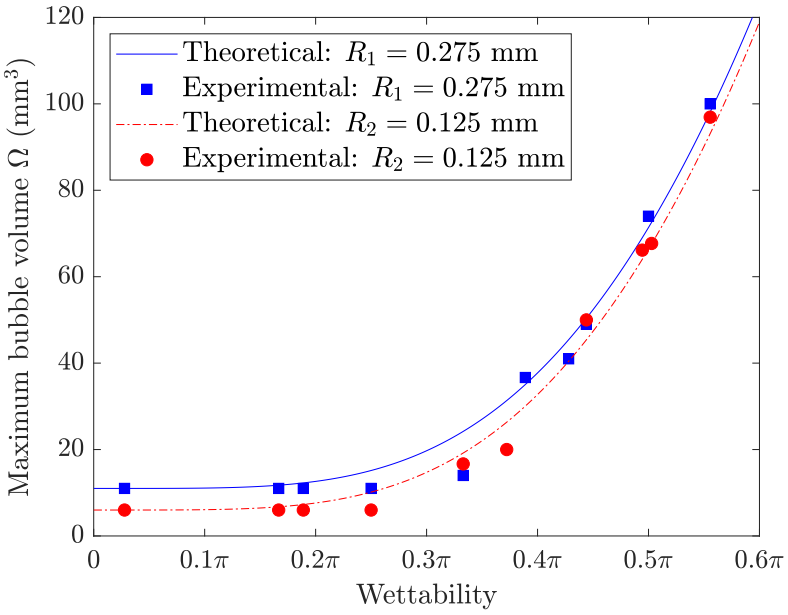

FIGURE 3.5: Maximum bubble volume Ω versus wettability θ_H: a comparison between the theoretical prediction (3.22) and the experimental data from Lin et al. [114]. The theory aligns well with the experiments for two orifice sizes, $R_1 = 0.275$ mm and $R_2 = 0.125$ mm.

constants obtained from $R_1 = 0.275$ mm, the established equation also predicts the experimental data correctly for the second orifice size, namely $R_2 = 0.125$ mm.

In addition, from equation (3.23), we have

$$\sigma_{GS}^{V} \approx 60 \text{ mJ/m}^2, \tag{3.25}$$

the surface energy of 304 stainless steel, i.e. the orifice material used in the experiments [114]. The surface energy of 304 stainless steel in other literature is about 50∼60 mJ/m^2 [130] [131], which confirms the value (3.25) deduced from our approach. This is another way for the validation of our approach.

3.2 Working principle of shadowgraphy

The objective of the experiments was to acquire the spatial and temporal informations about bubbles. By assuming that bubble shape is axisymmetric, the objective can be achieved by taking photos of bubble profile (i.e. projection of gas-liquid interface) at regular time intervals. Therefore, to highlight the gas-liquid interface in photograph, a shadowgraphy technique was chosen in our experiments. In principle, shadowgraphy is a backlighting technique, in other words, the subject is placed between the light source and the camera. Consequently, a shadow is generated due to the refraction of light in non-uniform transparent media [132]. For bubbly flow, collimated light will be refracted at the gas-liquid interface, as shown in Fig. 3.6.

According to Snell's law, the angle of refraction satisfies

$$\sin\theta_2 = \frac{\mathfrak{n}_1}{\mathfrak{n}_2}\sin\theta_1, \tag{3.26}$$

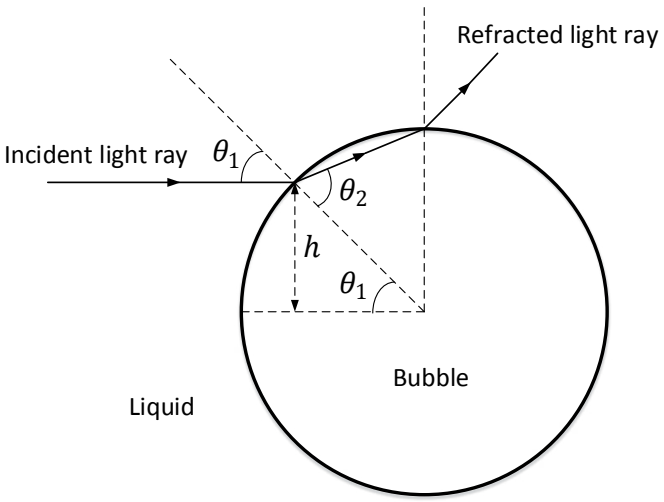

FIGURE 3.6: A light ray traveling in liquid will be refracted when it arrives at the gas-liquid interface.

where θ_1, θ_2 are angle of incidence, angle of refraction, respectively, and $\mathfrak{n}_1$, $\mathfrak{n}_2$ are the refractive index of liquid, gas respectively, which normally satisfies

$$\mathfrak{n}_1 > \mathfrak{n}_2, \tag{3.27}$$

since light travels faster in gas than in liquid. Therefore, we have

$$\theta_2 > \theta_1, \tag{3.28}$$

in other words, the parallel light beam in liquid diverges when it arrives at the interface. Besides, angle of incidence also satisfies

$$\sin\theta_1 = \frac{h}{r}, \tag{3.29}$$

where h is shown in Fig. 3.6, r is the radius of a spherical bubble. Substituting (3.29) into (3.26), we have

$$\sin\theta_2 = \frac{\mathfrak{n}_1}{\mathfrak{n}_2 r}h. \tag{3.30}$$

Therefore, the incident light ray is more deflected as it arrives at higher "latitude" of the bubble. As a consequence, the light rays that penetrate the central part of the bubble may still arrive at the image sensor of the camera, yet all the rest light rays passing through the bubble completely fan out, hence an annular-like shadow will appear on the recording plane, as shown in Fig. 3.7. In this way, the bubble profile is successfully recorded into the digital images as the borderline between dark and bright regions.

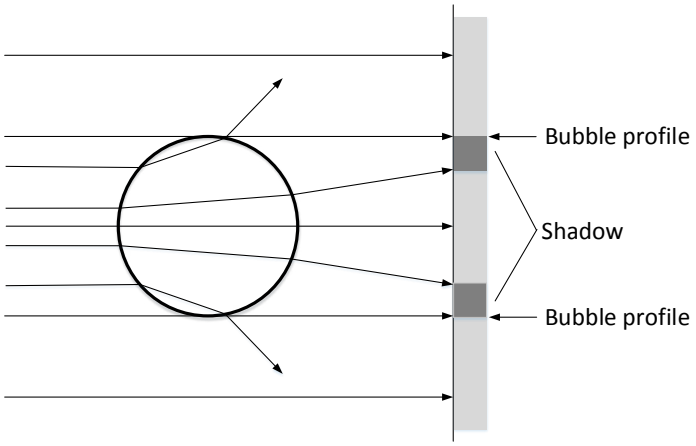

FIGURE 3.7: An annular-like shadow is formed on the recording plane when a light beam traveling in liquid meet a gas bubble due to the refraction.

3.3 Experimental setup

The experimental system was specially designed to support a long-term research on the physical and biological phenomena in photobioreactors, including this PhD project and the follow-up studies. For the present study, the experimental setup was mainly constituted of a photobioreactor, a gas injection system and a shadowgraphy measuring device, as shown in Fig. 3.8.

First of all, PIV experiments may be conducted in future investigations, thus a rectangular glass column was selected to be the photobioreactor, since a cylindrical reactor may cause optical distortion in the images [133]. The inner dimensions (width, depth and height) of the glass column were $28 \times 10 \times 60$ cm, respectively. The reactor walls were well cleaned before performing the experiments, in order to remove dust and grease that may stain the images. Afterwards, the reactor was filled with 30 cm of distilled water at 20 ± 1 °C.

Secondly, 9 brass chopper nozzles with inner diameter of 2 mm and 0.5 mm thick were uniformly distributed at the bottom, as shown in Fig. 3.9. And each nozzle was connected with an independent switching valve in order to investigate the influence of nozzle configuration on bubbling in the future. Nonetheless, in the present work, only the central nozzle was utilized to inject gas into liquid. And the gas flow rate was stabilized and regulated by a volumetric flow controller (VFC, range 0-500 mL/min, Bronkhorst F201-C).

Lastly, in the shadowgraphy equipment, a uniform light source (LED panel, 85×90 mm) and high speed camera (Phantom, V310) were arranged at the two sides of the reactor to record the bubbles with a rate of 200 fps (frame per second). The camera was triggered on turning on the VFC, thus the images also recorded the bubble train before its stabilization. For each flow rate condition, the images were recorded in triplicate and each recording lasted about one minute.

Besides, VFC was calibrated by bubble meter method [134], which requires only a graduated cylinder and a chronometer. The principle of measuring gas flow rate by bubble meter method is shown in Fig. 3.10.

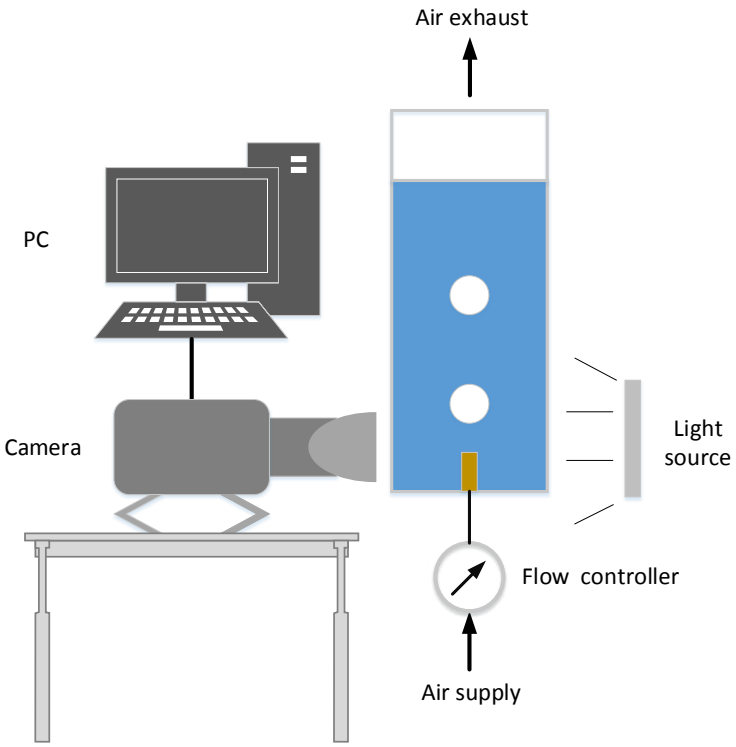

FIGURE 3.8: Schematic sketch of the experimental setup.

Therefore, the flow rate is

$$Q = \frac{V_i - V_f}{\Delta t}, \tag{3.31}$$

where V_i, V_f are the reading on the graduated cylinder before and after stopping injecting gas, respectively, Δt is the time interval recorded by the chronometer. The measurements were repeated 10 times for each VFC set point, and the results are reported in table 3.1. According to these results, the control of the gas flow rate was satisfactory, since the coefficient of variation of 10 measurements for each flow rate was less than 10%.

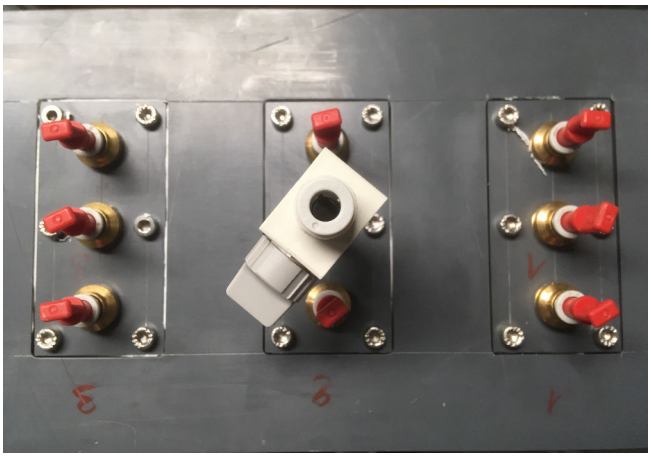

FIGURE 3.9: The 9 nozzles at the bottom of the reactor (the side connecting with gas source).

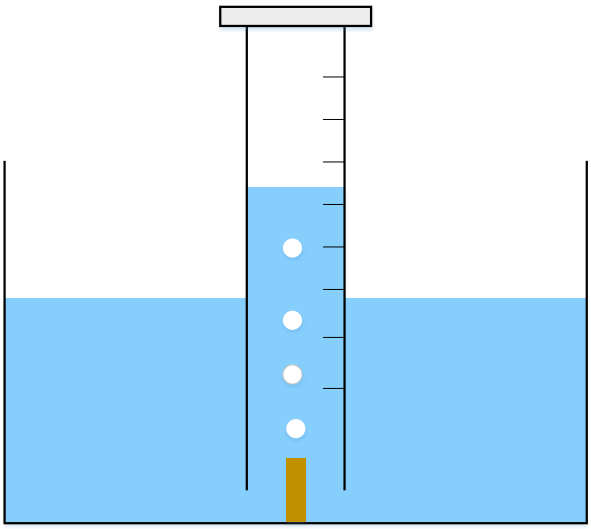

FIGURE 3.10: Bubble meter method to measure gas flow rate.

TABLE 3.1: Calibration of VFC.

Exp. No.	Percentage of full scale†	Measured flow rate* (mL/min)
FR1	1%	$\bar{X} = 80.3, \sigma = 5.8, c_v = 7.2\%$
FR2	3%	$\bar{X} = 110.2, \sigma = 1.9, c_v = 1.7\%$
FR3	6%	$\bar{X} = 145.5, \sigma = 1.3, c_v = 0.89\%$
FR4	9%	$\bar{X} = 179.1, \sigma = 2.3, c_v = 1.3\%$
FR5	12%	$\bar{X} = 216.8, \sigma = 4.4, c_v = 2.0\%$
FR6	20%	$\bar{X} = 314.6, \sigma = 8.1, c_v = 2.6\%$
FR7	30%	$\bar{X} = 428.1, \sigma = 20.2, c_v = 4.7\%$

† 100%: 1000 mL/min (theoretical)
* $\bar{X}$: mean, σ: standard deviation, c_v: coefficient of variation, sample size: 10

3.4 Image processing

Thanks to the shadowgraphy technique, bubbles were recorded in 12-bit grayscale images (intensity range $[0, 4095]$), image resolution was 800×400, an arbitrarily chosen raw image is shown as an example in Fig. 3.11(a). In the raw image, the liquid and the central part of a bubble are bright, whereas the peripheral part of a bubble is dark, which is the expected optical phenomenon according to the principle of shadowgraphy in section 3.2. The raw images were binarized by Otsu's method [135] [136]. This method assumes that an image contains two kinds of pixels: background and foreground. Then, based on the pixel intensity histogram, it determines the best threshold to segregate those two pixel populations. In our case, this method is particularly well-suited, since the two pixel populations were very distinct thanks to light uniformity, as shown in Fig. 3.12, the histogram of Fig. 3.11(a). And the binarized image is shown in Fig. 3.11(b). However, a bubble in the binarized images always included some white zones that are inherent in shadowgraphy. Therefore, the white zones were eliminated through *area opening* [137], which removes all the connected components (objects) with pixels lower than a given value, as shown in Fig. 3.11(c). Finally, the black and white pixels were inverted to make further analysis possible, as shown in Fig. 3.11(d), since it is the white pixels that were recognized as an object.

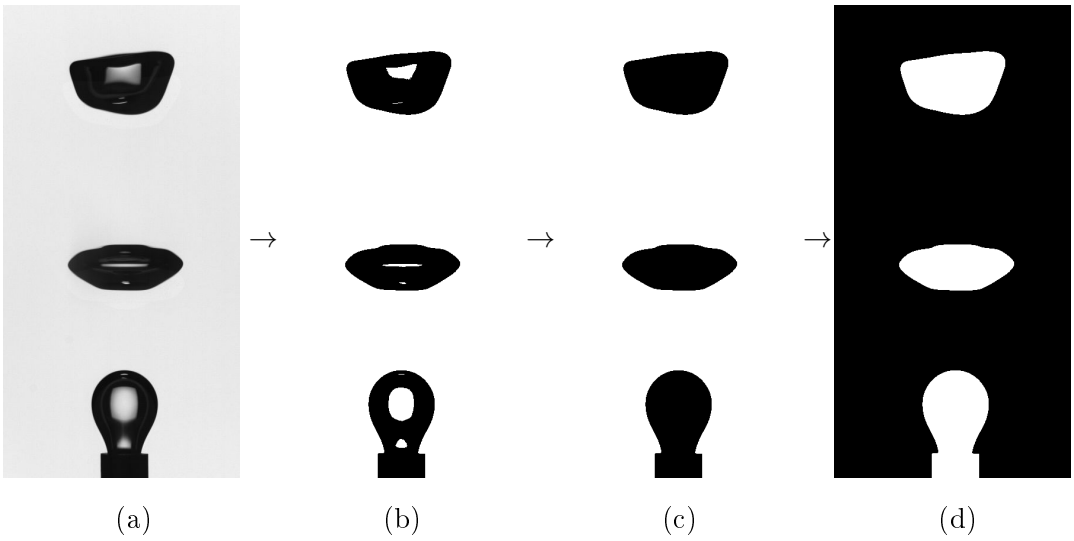

FIGURE 3.11: Image processing. (a) raw image, (b) binarized image, (c) white zones eliminated, (d) inverted image.

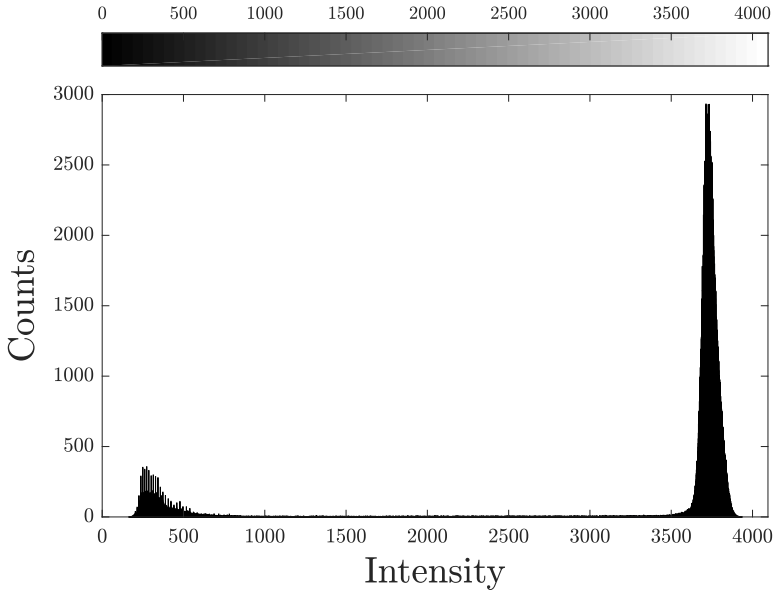

FIGURE 3.12: The histogram of Fig. 3.11(a), bin width: 1.

3.5 Image analysis

3.5.1 Counting bubbles

To count bubbles, a probe point was placed in the processed images (about 9 mm above the nozzle), in order to detect a bubble after its detachment from the nozzle, as shown in Fig. 3.13(a). The pixel intensity $\mathcal{I}$ at this probe point indicated whether a bubble reached the point:

$$\mathcal{I} = \begin{cases} 1, & \text{a bubble is present} \\ 0, & \text{absence of bubble} \end{cases} . \tag{3.32}$$

As a consequence, the pixel intensity $\mathcal{I}$ of a sequence of images formed a series of square pulses, one pulse implied a new bubble, as shown in Fig. 3.13(b). Therefore, the bubbles were counted by counting the pulses. Besides, in order to assess for the quality of this method, the influence of the probe point position on the bubble features (bubbling frequency, bubble volume and bubble shape factor) was investigated and shown not to be relevant as long as the probe point was not in contact with most of the bubbles before its detachment.

3.5.2 Bubbling frequency

With the "probe-point" method, the pulses were counted automatically by a code developed in Matlab. In other words, the temporal evolution of bubble number was obtained, as shown in Fig. 3.14(a). Subsequently, the bubbling frequency was also calculated by differentiating the bubble number with respect to time, as shown in Fig. 3.14(b). Inspecting Fig. 3.14(b), we found that the bubbling frequency became almost insensitive to time after a few seconds, which indicated that the bubbling steady state was reached after a period of fast changes in the bubbling frequency. This transient regime at the beginning was due to the pressure buildup in the tubing prior to the

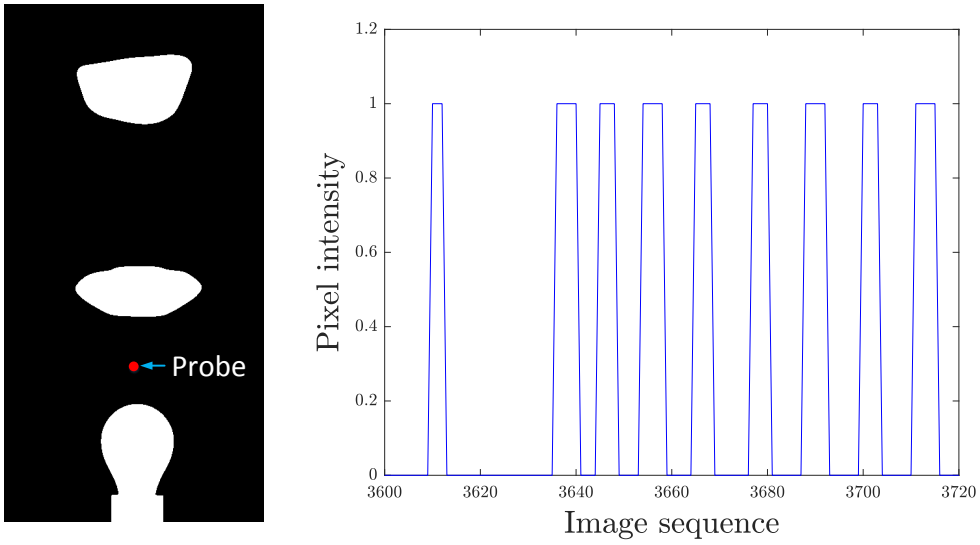

FIGURE 3.13: Counting bubbles at VFC 1%. (a) the probe point (red point), (b) pixel intensity of probe point over an image sequence.

opening of the VFC. Finally, bubbling frequency for all the flow rates is plotted in Fig. 3.15, and the mean bubbling frequency at steady state is reported in table 3.2, where we can see that the bubbling frequency at steady state increased with the flow rate, yet the fluctuation of bubbling frequency also increased with flow rate.

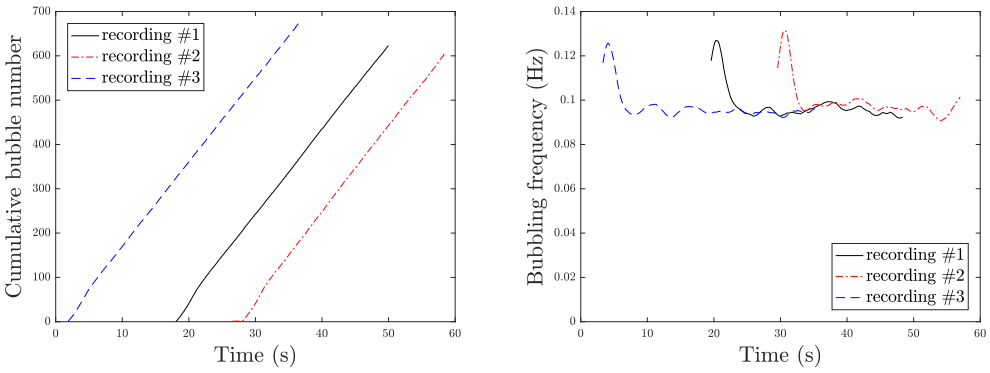

FIGURE 3.14: The evolution of (a) bubble number and (b) bubbling frequency for the triplicate recordings at VFC 1 %.

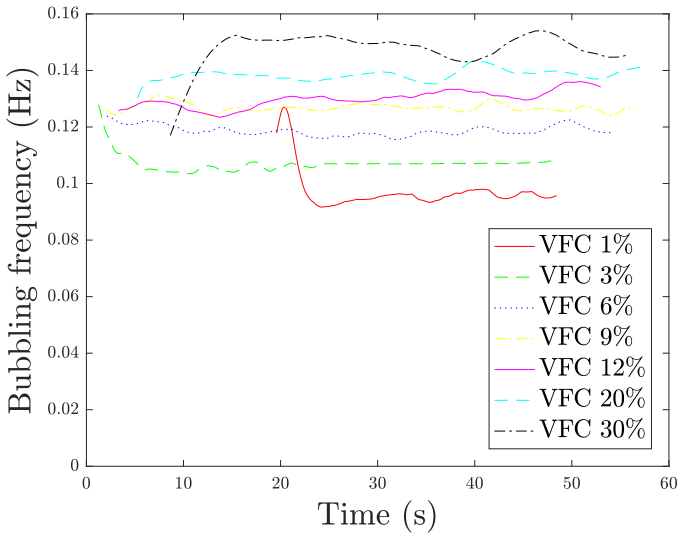

FIGURE 3.15: Bubbling frequency for all the flow rates.

TABLE 3.2: Mean bubbling frequency at steady state.

VFC set point	Bubbling frequency* (Hz)
1%	$\bar{X} = 0.0894, \sigma = 0.0232$, $c_v = 26.0\%$
3%	$\bar{X} = 0.1011, \sigma = 0.0247$, $c_v = 24.4\%$
6%	$\bar{X} = 0.1091, \sigma = 0.0322$, $c_v = 29.5\%$
9%	$\bar{X} = 0.1186, \sigma = 0.0311$, $c_v = 26.3\%$
12%	$\bar{X} = 0.1189, \sigma = 0.0392$, $c_v = 33.0\%$
20%	$\bar{X} = 0.1214, \sigma = 0.0465$, $c_v = 38.3\%$
30%	$\bar{X} = 0.1251, \sigma = 0.0538$, $c_v = 43.0\%$

* $\bar{X}$: mean, σ: standard deviation, c_v: coefficient of variation

3.5.3 Bubble volume

The bubble volume was calculated from a 2D processed image by the horizontal segmentation method (HSM) [138] [139]. The main algorithm of this method is to slice a bubble horizontally, and every slice is supposed to be a disc, as shown in Fig. 3.16.

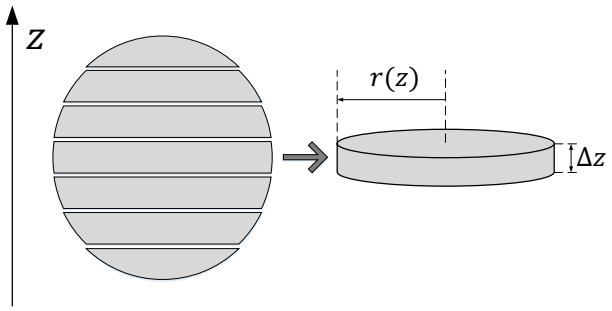

FIGURE 3.16: The horizontal segmentation method to calculate bubble volume.

The radius of a disc is a function of height $r(z)$, thus the bubble volume is expressed as:

$$V = \int \pi r^2(z) dz. \tag{3.33}$$

In reality, a disc has its thickness Δz, therefore the bubble volume is approximated as

$$V \approx \sum \pi r^2 \Delta z. \tag{3.34}$$

In this work, r was obtained by counting the pixel horizontally from the processed image, and Δz was equal to one pixel. A detached bubble normally had a diameter of about $10 \sim 100$ pixels. Consequently, even if few pixels were omitted at the gas-liquid interface due to the binarization, the relative error on the estimate of r was only a few percent, which is acceptable. At last, the bubble volume expressed in pixels was converted into cubic millimeter by using a spatial calibration factor.

Moreover, a bubble constantly changed its shape during rising, as shown in Fig. 3.17 (a). Therefore, we first investigated the sensitivity of HSM to bubble shape by applying HSM to the same bubble but in different frames (shapes). The result is plotted in Fig. 3.17(b), which shows that the bubble volume calculated by HSM in a series of consecutive frames was nearly insensitive to the bubble shape: the variation of the calculated volume is at the most 10 %. Therefore, the volume of a bubble can be estimated by taking the average of the volumes at different moments:

$$V_i = \frac{1}{m} \sum_{j=1}^{m} V(t_j), \tag{3.35}$$

where V_i indicates the volume of the i-th detached bubble, m is the number of frames including the same bubble, about $4 \sim 6$ in general.

Subsequently, the temporal distribution of all the V_i was obtained for VFC 1%, as shown in Fig. 3.18(a), where one dot corresponds to one bubble. The bubbling process consisted of two obviously different stages. The first stage, i.e. Ⓐ period in Fig. 3.18(a), had a strong raise followed by a sharp decrease of bubble volume, which corresponded to the unsteady gas flow regime that was already observed in Fig.

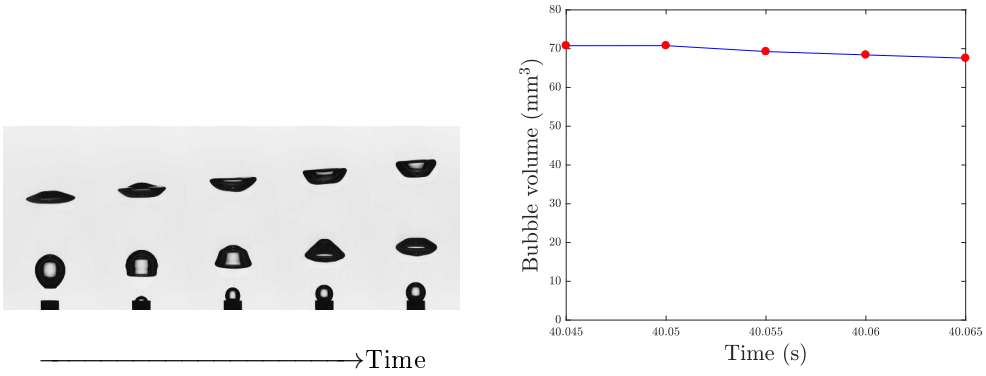

(a) (b)

FIGURE 3.17: (a) shape and (b) volume of a just detached bubble at different moments (VFC 1%).

3.14(b). After a few seconds, in a second stage, i.e. Ⓑ period in Fig. 3.18(a), the bubbling reached steady state, since the volume of each bubble was quasi constant. As revealed by Fig. 3.18(c), histogram of all the V_i at steady state at VFC 1%, more than 90% of bubbles at steady state were concentrated in a small range of volume: about $69 \sim 78$ mm^3, this is the major bubble population. It also existed a second minor bubble population, whose volume ranged approximately from 10 to 50 mm^3, and this population is clearly distinct from the previous one. These tiny bubbles appeared regularly in the bubbling as shown with the lower dots in Fig. 3.18(a), and were regularly visualized in the frames, such as Fig. 3.18(b). This population represents less than 10% of the bubbles at steady state. One could assume that the occurrence of such tiny bubbles may result from small variations of the gas flow rate despite the use of a gas flow controller.

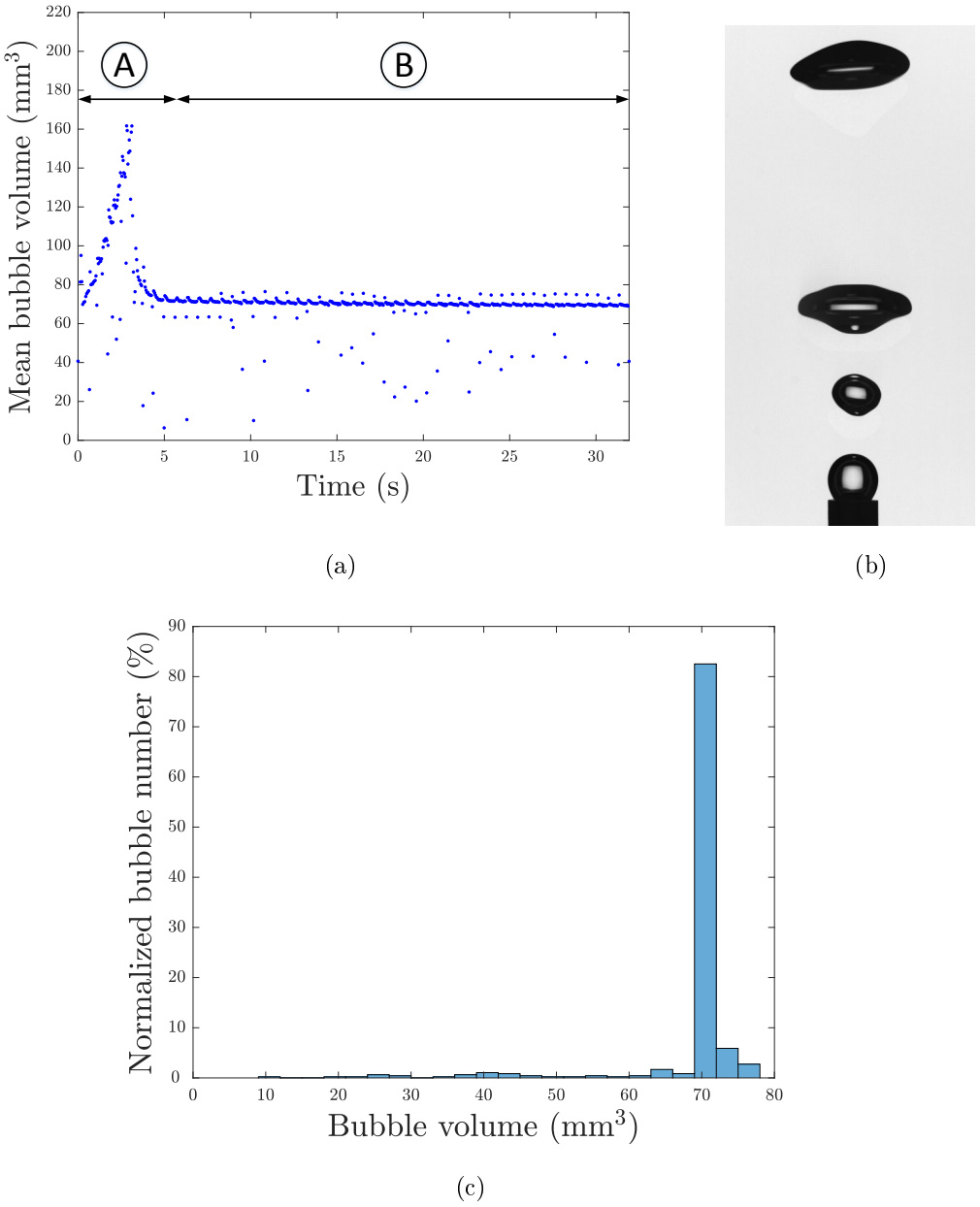

FIGURE 3.18: (a) the temporal distribution of bubble volume, (b) a small bubble occurred at $t = 10.1$ s at steady state, (c) histogram of bubble volume at steady state, bin width: 3 (VFC 1%).

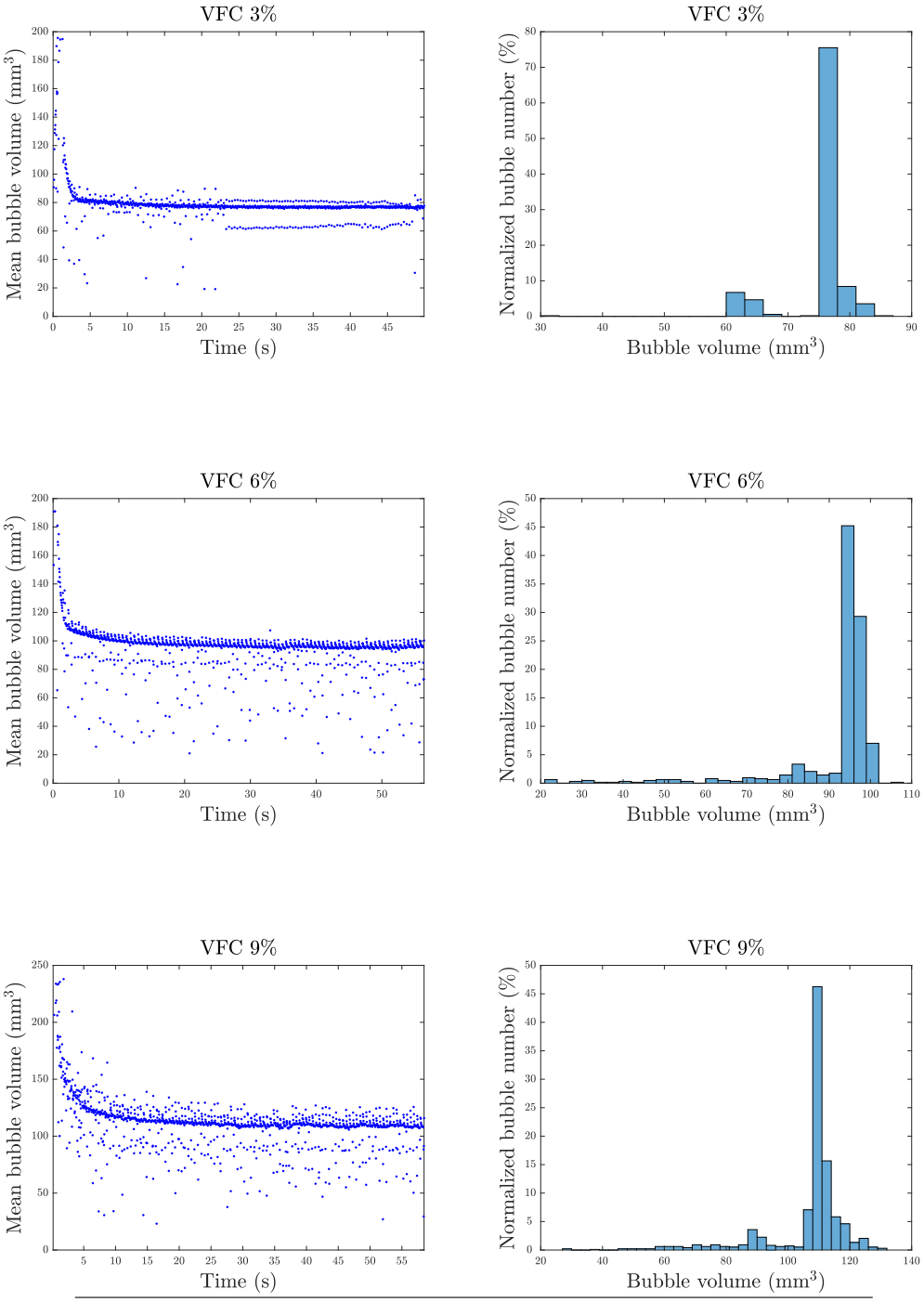

FIGURE 3.19: The temporal distribution (left column) and histogram (right column) of bubble volume at VFC 3%-9%, bin width: 3.

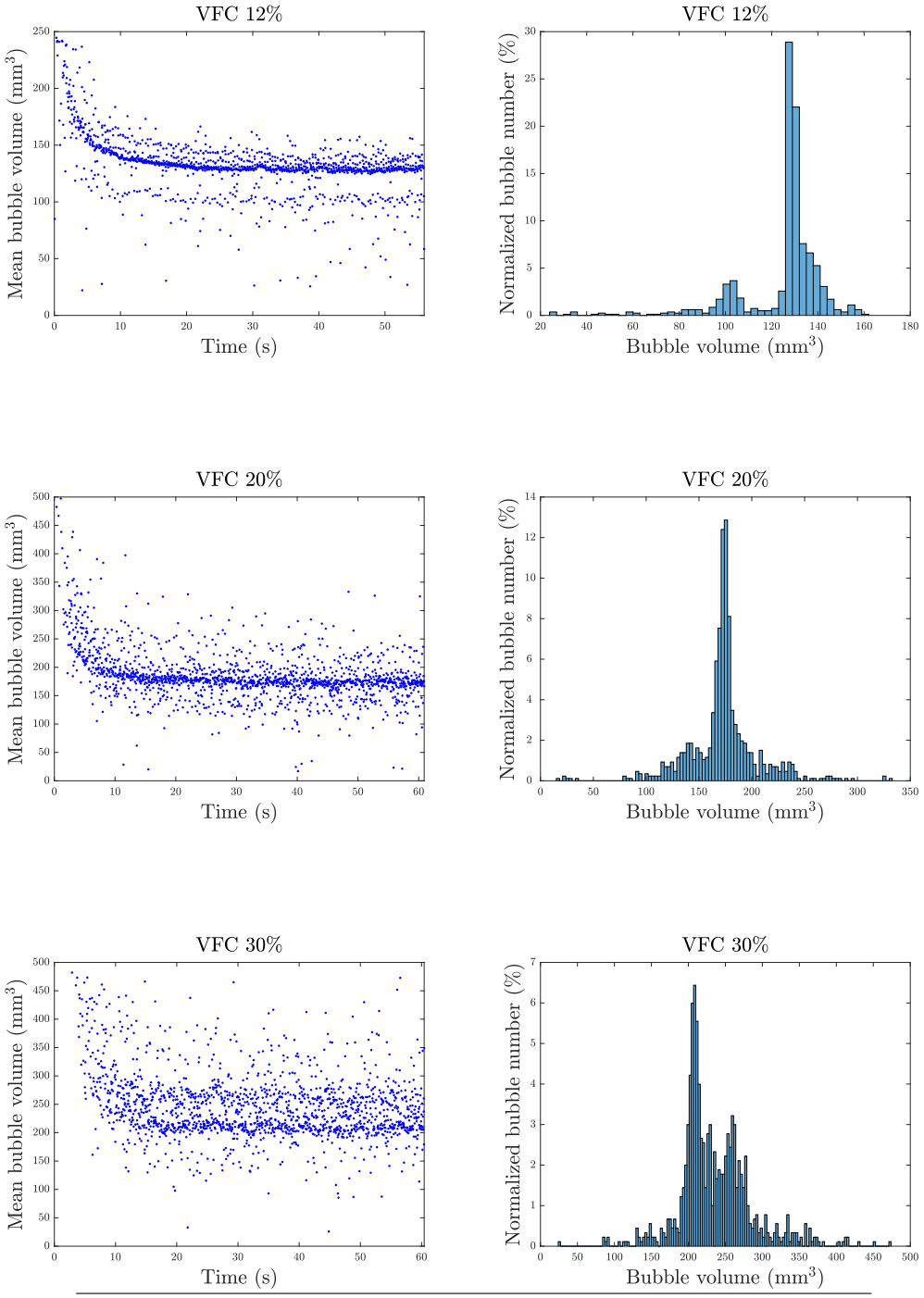

FIGURE 3.20: The temporal distribution (left column) and histogram (right column) of bubble volume at VFC 12%-30%, bin width: 3 .

Furthermore, the temporal distribution and histogram of bubble volume for other flow rates are also plotted in Fig. 3.19 and 3.20, where we observed that the bubbling always underwent the same unsteady-to-steady regime at whatever flow rate. We also found that bubble volume increased with flow rate. Besides, as the flow rate increased, the bubble volume was more and more distributed, and more distinct groups of bubbles were generated: about 2 groups at VFC 1 $\sim$ 9%, 3 groups at VFC 12 $\sim$ 20%, and 4 groups at VFC 30%. In other words, the temporal distribution of bubble volume was more scattered at higher flow rate, as indicated by the histograms: it became more spreading as the flow rate increased. The increased dispersion of bubble volume with flow rate may result from the more frequent bubble coalescence at higher flow rate. In order to more quantitatively evaluate the influence of flow rate on the bubble volume, we calculated the mean and standard deviation of all the V_i at steady state, as shown in Fig. 3.21. Both mean and standard deviation of bubble volume generally increased with flow rate, which confirmed our visual observations from Fig. 3.19 and 3.20.

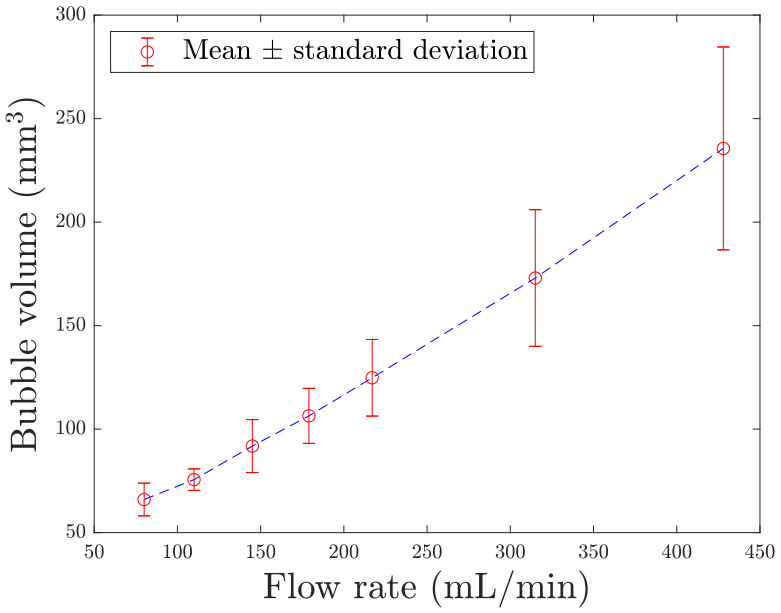

FIGURE 3.21: The mean and standard deviation of bubble volumes at steady state.

3.5.4 Bubble shape factors

Shape factors of bubbles are important indicators to evaluate the consistency between the experimental and numerical results [140]. First, a very common shape factor is the aspect ratio, which is defined as

$$A_R = \frac{h}{w}, \tag{3.36}$$

where h is the vertical height of the bubble and w is the horizontal width. The value of this shape factor could be lower or higher than unity, depending on the bubble oscillation.

Another often used factor is circularity, defined as

$$f_{\text{circ}} = \frac{4\pi A}{\mathscr{P}^2}, \tag{3.37}$$

where A is the projected area of the bubble, $\mathscr{P}$ is its corresponding perimeter. A and $\mathscr{P}$ were obtained directly by counting pixels in the image. The significance of this shape factor is the squared ratio of the perimeter of a circle having the same area as a 2D object to the perimeter of the 2D object:

$$f_{\text{circ}} = \left(\frac{\mathscr{P}_{\text{circle}}}{\mathscr{P}_{\text{object}}}\right)^2 = \left(\frac{2\pi\sqrt{\frac{A_{\text{object}}}{\pi}}}{\mathscr{P}_{\text{object}}}\right)^2 = \frac{4\pi A_{\text{object}}}{\mathscr{P}^2_{\text{object}}}. \tag{3.38}$$

The circularity can not be greater than 1, since a circle has the shortest perimeter among all the shapes with the same area. Therefore, only a perfectly spherical bubble would give

$$f_{\text{circ}} = 1. \tag{3.39}$$

In other cases, f_{circ} is smaller than 1, and the smaller f_{circ}, the more flattened (either horizontally or vertically) the bubble is.

In order to calculate the bubble shape factors from the processed images, a code was developed in Matlab based on equations (3.36) and (3.37). With this code, we first obtained the evolution of shape factors of a just detached bubble that was arbitrarily chosen from the major bubble population, as shown in Fig. 3.22(b). For this bubble, both circularity and aspect ratio generally decreased as the bubble rose in a very short period of time (≈ 25 ms). Actually, this trend was observed for all the bubbles whatever the gas flow rate. After the bubble flattened, it continued oscillating until bursting at the water surface. Bubble oscillation is a natural result of surface tension, as any object experiencing a tension force and perturbed from its equilibrium position tends to oscillate.

Furthermore, in consideration of the potential variability from bubble to bubble, we also calculated the shape factors for a population of similar bubbles, i.e. those in the major bubble population, refer to Fig. 3.18(a) and (c). The result is shown in Fig. 3.23, where two overlapping lines represent the evolution of the two shape factors of the same bubble before it left the field of view. Both shape factors were at maximum at the moment a bubble just detached, and they decreased as the bubble rose, as already observed in Fig. 3.22(b). Moreover, the circularity was quite repeatable for all the bubbles: its initial value was always close to 1 for each bubble, since a bubble appeared as almost perfectly rounded when it just escaped from the nozzle, and the circularity also decreased to approximatively 0.8 for each bubble. The repeatability and initial unity of circularity implies that the projected area and perimeter were correctly captured. On the contrary, the aspect ratio was less consistent than circularity: aspect ratio sometimes started at about 1.1 rather than 1, the theoretical value for a spherical bubble. Certainly, from another perspective, we can also think that aspect ratio was more sensitive to small variation of bubble shape: even though two bubbles were similar in terms of circularity, they were possibly quite different regarding aspect ratio, for example the second and third bubbles in Fig. 3.23. In other words, the circularity was more "error-tolerant" than the aspect ratio, since the circularity included much more spatial information than the aspect ratio.

(a)

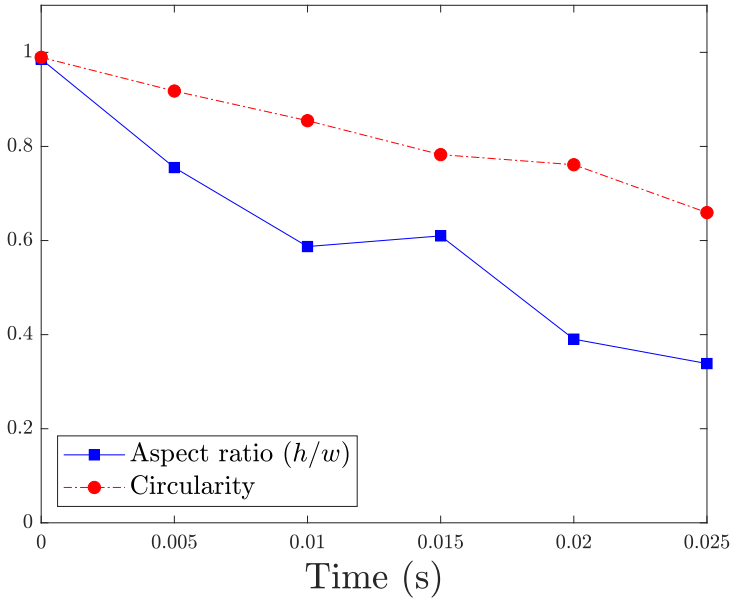

(b)

FIGURE 3.22: (a) a just detached bubble at steady state, and (b) its evolution of aspect ratio and circularity (VFC 1%).

Besides, as flow rate has significant influence on bubble volume, it is very likely that the bubble shape evolution at high flow rate may also be different from the one at low flow rate. Therefore, we also calculated the shape factors of a population of bubbles at steady state at VFC 30%, as shown in Fig. 3.24. At high flow rate, we found that larger aspect ratio occurred more frequently, which implies that the bubbles were generally more elongated than those at low flow rate, as shown in Fig. 3.25(a). The larger aspect ratio may also result from the false or authentic bubble coalescence due to the shorter distance between two bubbles at high flow rate, as shown in Fig. 3.25(b) and (c). In brief, bubble shape was less rounded, yet still exhibiting axisymmetry, and bubble coalescence was more frequent at high flow rate.

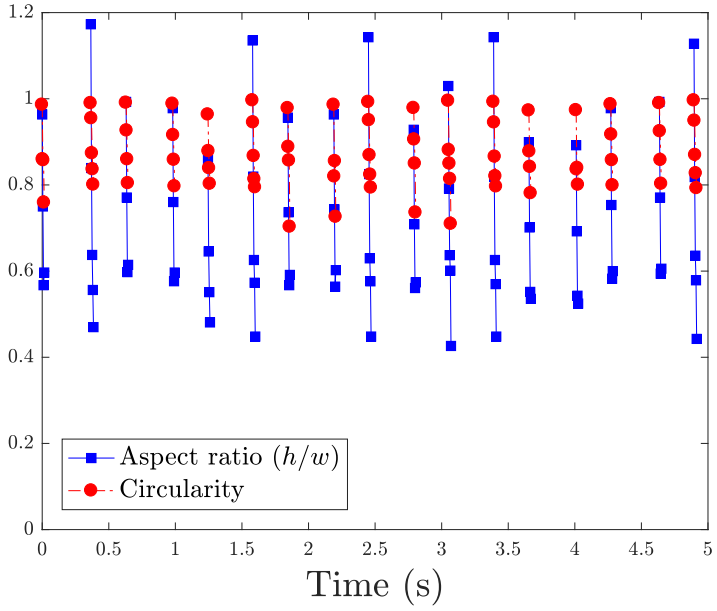

FIGURE 3.23: The evolution of aspect ratio and circularity of a population of bubbles at steady state (VFC 1%).

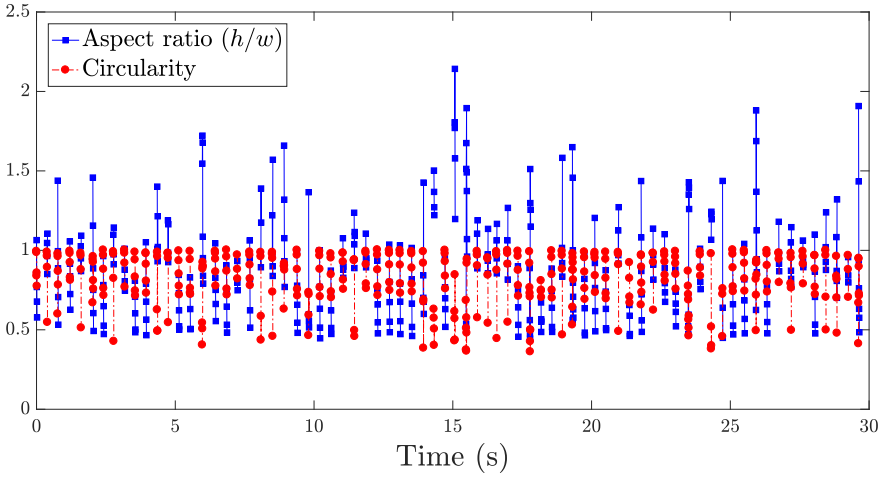

FIGURE 3.24: The evolution of aspect ratio and circularity of a population of bubbles at steady state (VFC 30%).

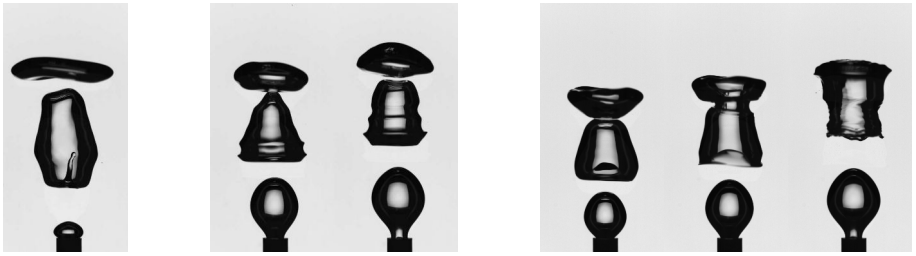

(a) (b) (c)

FIGURE 3.25: (a) an elongated bubble, (b) false bubble coalescence, (c) authentic bubble coalescence. (VFC 30%)

3.6 Conclusions

In this chapter, we first introduced the principle of shadowgraphy technique, which is based on the refraction of light when it passes from water into air. With shadowgraphy technique, bubbles were successfully captured into images. Furthermore, bubble behaviors at different flow rates were studied by images processing and analysis. First of all, we observed that bubbling frequency at each flow rate tended to be stable after a few seconds of response time of flow meter, and bubbling frequency at steady state increased with flow rate. Second, mean bubble volume increased with flow rate, and bubble volume distribution was quite monodisperse at low flow rate, yet it became more polydisperse at higher flow rate. Finally, the aspect ratio and circularity of most bubbles begun at 1 at low flow rate, implying that bubbles were rounder and gas-liquid interface was smoother at low flow rate, and one bubble was relatively distant from another one. On the contrary, a considerable amount of just detached bubbles had the aspect ratio greater than 1 at high flow rate, indicating that bubbles deformed more violently at its detachment and the bubble coalescence was significant.

Chapter 4

Numerical study

As mentioned in section 2.3, gas-liquid flow in a photobioreactor is a bubbly flow, thus it would be better that the numerical model can represent the dispersed bubbles. In consideration of this requirement, Volume of fluid (VOF) method was chosen to be the modeling framework since it can simulate discrete and deformable bubbles. Furthermore, the implementation of VOF method was made on an open source platform, OpenFOAM, which is becoming more and more popular in scientific research thanks to its versatility and flexibility. Subsequently, case setups were presented and experiments were reproduced numerically. Finally, the simulation results are discussed.

4.1 Introduction to VOF method

VOF method is a numerical technique that can track the interface of two or more immiscible fluids [141]. In VOF method, each fluid and interface is recognized by a volume fraction function that is between 0 and 1 [142] [143]. The temporal evolution of the volume fraction function is described by the classical advection equation [144]. With the volume fraction function, a single set of momentum equations can be obtained for the entire computational domain by volume-averaging the physical properties, such as viscosity, density, etc. [145].

4.1.1 Volume fraction function

VOF method treats only two fluids for a gas-liquid system.

Definition

First, we introduce an indicator function at a point in the numerical domain [146] [147] [148]:

$$\mathscr{F}(x,y,z) = \begin{cases} 1 & \text{point occupied by liquid} \\ \Lambda & \text{point on the interface} \\ 0 & \text{point occupied by gas} \end{cases}, \tag{4.1}$$

where Λ is a constant between 0 and 1. Consequently, the volume fraction of liquid in a control volume (C.V.) V is

$$\alpha_l = \frac{1}{V} \iiint_V \mathscr{F}(x,y,z) dV, \tag{4.2}$$

where x, y, z are the spatial coordinates. Meanwhile, the reverse relation of (4.2) is

$$\mathscr{F}(x,y,z) = \lim_{V \to 0} \alpha_l. \tag{4.3}$$

Understandably, the volume fraction of gas is

$$1 - \alpha_l. \tag{4.4}$$

From equations (4.1) (4.2) we can see that the value of α_l signifies

$$\alpha_l = \begin{cases} 1 & \text{C.V. occupied by liquid} \\ \in (0,1) & \text{C.V. including a segment of interface .} \\ 0 & \text{C.V. occupied by gas} \end{cases} \tag{4.5}$$

In computational fluid dynamics, the computational domain is usually divided into many cells. Each cell is considered as a C.V., thus the content of each cell can be known from equation (4.5). Consequently, the spatial information of both phases is obtained by reassembling all the cells, as shown in Fig. 4.1.

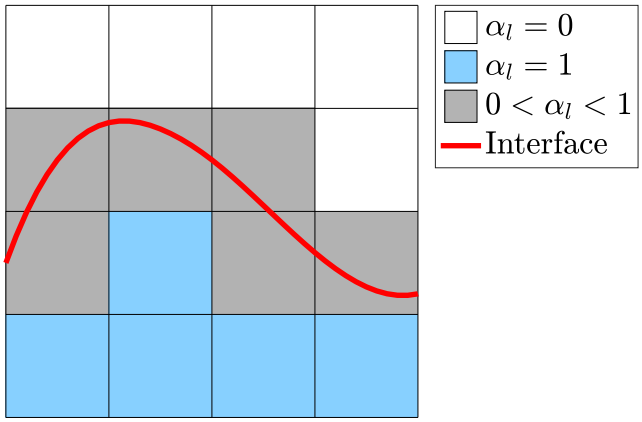

FIGURE 4.1: The value of α implies the distribution of two fluids in the computational domain.

Temporal evolution

In previous discussions, the two fluids are spatially represented by the volume fraction α_l. Therefore, the kinematics of the two fluids is given by the temporal evolution of α_l.

Both liquid and gas are locally conserved, thus α_l is also locally conserved. Any locally conserved scalar field is described by the advection equation, i.e. continuity equation. Therefore, α_l also satisfies the advection equation

$$\frac{\partial \alpha_l}{\partial t} + \nabla \cdot (\vec{u}\alpha_l) = 0, \tag{4.6}$$

which is also the temporal evolution of α. If both fluids are considered to be incompressible, the velocity field satisfies

$$\nabla \cdot \vec{u} = 0. \tag{4.7}$$

Accordingly, the advection equation of α_l is simplified to

$$\frac{\partial \alpha_l}{\partial t} + \vec{u} \cdot \nabla \alpha_l = 0. \tag{4.8}$$

However, the velocity field $\vec{u}$ in equation (4.8) is still an unknown quantity so far. Actually, $\vec{u}$ is obtained by solving the volume-averaged Navier-Stokes equations, which is discussed in section 4.1.2.

Normal vector of the interface

For a C.V. including a segment of interface, the gradient of α of this C.V. is closely related to the normal vector of this interface, as demonstrated below.

Supposing the C.V. is small enough, according to equation (4.3), the gradient of α is

$$\nabla \alpha_l \approx \nabla \mathscr{F}. \tag{4.9}$$

Meanwhile, according to equation (4.1), the equation for interface is

$$G(x, y, z) = \mathscr{F}(x, y, z) - \Lambda = 0. \tag{4.10}$$

Therefore, the normal vector at the interface is

$$\vec{n} = \nabla G = \nabla(\mathscr{F} - \Lambda) = \nabla \mathscr{F}. \tag{4.11}$$

From equations (4.9) (4.11), we have

$$\vec{n} \approx \nabla \alpha_l, \tag{4.12}$$

which implies that the normal direction of interface can be approximated by the gradient of volume fraction.

4.1.2 Momentum equations

In VOF method, the velocity field $\vec{u}$ is shared by both fluids, which means that VOF method solves only a single set of momentum equations for all the phases:

$$\frac{\partial}{\partial t}(\rho \vec{u}) + \nabla \cdot (\rho \vec{u} \vec{u}) = -\nabla p + \nabla \cdot \left[\eta \left(\nabla \vec{u} + \nabla \vec{u}^T\right)\right] + \rho \vec{g} + \vec{f_\sigma}, \tag{4.13}$$

where $\vec{f_\sigma}$ is the surface tension expressed as a volume force, and the material properties are given by

$$\rho = \alpha_l \rho_l + (1 - \alpha_l)\rho_g, \tag{4.14}$$

$$\eta = \frac{1}{\rho}\left[\alpha_l \rho_l \mu_l + (1 - \alpha_l)\rho_g \mu_g\right], \tag{4.15}$$

where ρ_l, ρ_g are the densities of liquid, gas, respectively, and η_l, η_g are the viscosities of the two fluids.

The surface tension in equation (4.13) is approximated by a CSF (Continuum Surface Force) model [141] [146]:

$$\vec{f_\sigma} = \sigma \kappa \vec{n} \left[\frac{\alpha_l \rho_l + (1 - \alpha_l)\rho_g}{\frac{1}{2}(\rho_l + \rho_g)}\right], \tag{4.16}$$

where $\vec{n}$ is the normal to the interface, given in equation (4.12), σ is the surface tension per unit length, κ is the curvature of the interface, defined as

$$\kappa = -\nabla \cdot \hat{n}, \tag{4.17}$$

where $\hat{n}$ is the unit normal vector to the interface

$$\hat{n} = \frac{\vec{n}}{|\vec{n}|}, \tag{4.18}$$

substituting (4.18) into (4.17), we have

$$\begin{aligned}
\kappa &= -\nabla \cdot \hat{n} \\
&= -\nabla \left(\frac{1}{|\vec{n}|} \cdot \vec{n} \right) \\
&= -\left[\frac{1}{|\vec{n}|} \nabla \cdot \vec{n} + \vec{n} \cdot \nabla \left(\frac{1}{|\vec{n}|} \right) \right] \\
&= -\left\{ \frac{1}{|\vec{n}|} \nabla \cdot \vec{n} + \vec{n} \cdot \left[\left(-\frac{1}{|\vec{n}|^2} \right) \nabla |\vec{n}| \right] \right\} \\
&= \frac{1}{|\vec{n}|} \left(\frac{\vec{n}}{|\vec{n}|} \nabla |\vec{n}| - \nabla \cdot \vec{n} \right).
\end{aligned} \tag{4.19}$$

With equations (4.16) (4.12) (4.19), the surface tension is finally expressed as a function of volume fraction:

$$\vec{f_\sigma} = \sigma \frac{\nabla \alpha_l}{|\nabla \alpha_l|} \left[\frac{\nabla \alpha_l}{|\nabla \alpha_l|} \nabla |\nabla \alpha_l| - \nabla \cdot (\nabla \alpha_l) \right] \left[\frac{\alpha_l \rho_l + (1 - \alpha_l) \rho_g}{\frac{1}{2}(\rho_l + \rho_g)} \right]. \tag{4.20}$$

4.1.3 Interface reconstruction

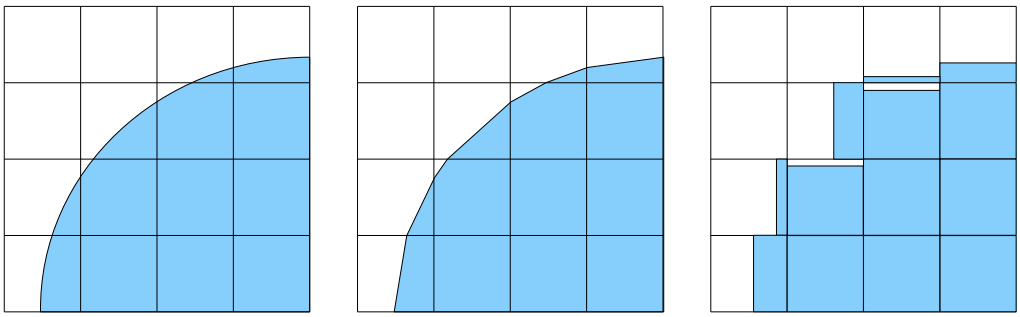

FIGURE 4.2: Comparison of algorithms for interface reconstruction. (a) actual interface, (b) piecewise linear interface calculation (PLIC), (c) simple line interface calculation (SLIC)/donor-acceptor (D-A).

Volume fraction can not reconstruct the interface alone, since volume fraction is a scalar, yet the interface is oriented in a certain direction (i.e. normal). Therefore, it requires some additional algorithms to reconstruct the interface. It exists mainly three algorithms, as shown in Fig. 4.2: simple line interface calculation (SLIC) [149], donor-acceptor (D-A) [142], and piecewise linear interface calculation (PLIC) [150]. According to SLIC and D-A, the interface can only be placed horizontally or vertically

in a computational cell [145]. Compared with the previous algorithms, PLIC had a significant improvement since it allows an oblique interface [151], whose normal is given by equation (4.12). Subsequently, the interface is parallelly transported until it meets the volume fraction of the cell [152], as shown in Fig. 4.3.

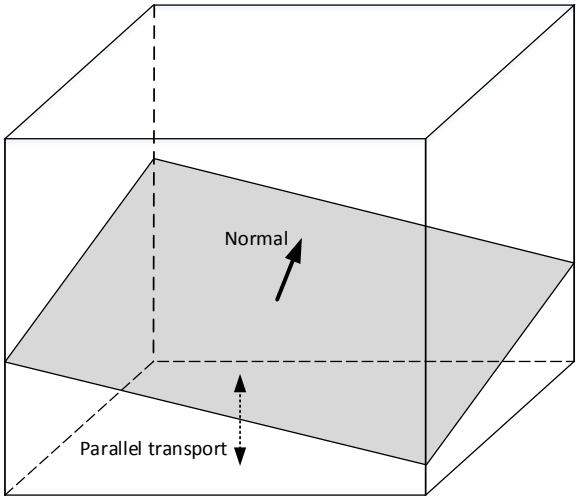

FIGURE 4.3: Two steps of PLIC: 1. the normal direction is approximated by $\nabla\alpha$, 2. parallel transport of the interface to satisfy the volume fraction.

4.1.4 Pros and cons

VOF method and Eulerian-Lagrangian model are the mainstream multiphase models that can capture the bubble behavior and its effects, they are compared in table 4.1. In comparison with E-L model, the main advantage of VOF is that more complicated and important bubble behaviors, such as bubble breakage and deformation, are calculated implicitly, as shown in Fig. 4.4. In fact, VOF method can handle merging and breakup of any fluid-fluid interface. Therefore, VOF is often applied to simulate jet breakup, dam break, the motion and deformation of large bubble in a liquid, etc. [141].

TABLE 4.1: Comparison of VOF and Eulerian-Lagrangian model

	Computing Time	Bubble size	Deformation/coalescence/breakage
VOF	Long	Calculated†	Calculated†
E-L	Medium	Supplied*	Supplied*

† Calculated: these quantities or phenomena are calculated by the model itself, no extra operation needed.
* Supplied: these quantities or phenomena can not be calculated or handled by the model, thus relevant data or algorithm should be additionally supplied.

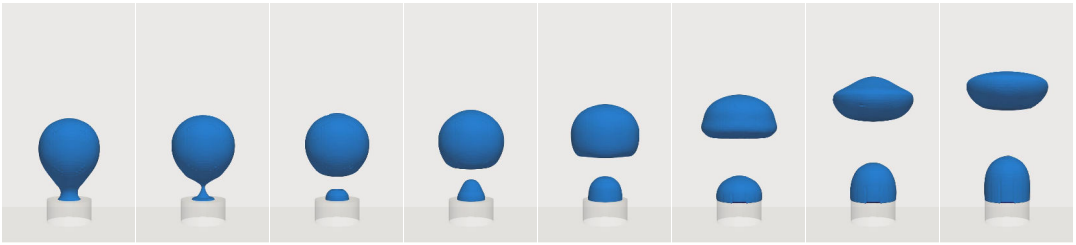

FIGURE 4.4: Bubble breakage and deformation calculated implicitly by VOF method, illustrations from our simulations (scale: exterior diameter of the nozzle is 3 mm).

In addition to the advantages, like any other numerical model, VOF also has some limitations. For example, as indicated in Fig. 4.1, the accuracy of the interface location strongly depends on the grid size: the interface is better resolved as the computational cells increase. More than the interface location, all the physical informations at sub-grid scale are completely blurred, which may lead to physically meaningless results if the mesh is too coarse. For example, the artificial coalescence may occur when the distance between two bubbles/droplets is less than the grid size [144]. Therefore, to obtain more accurate results, mesh is often very fine in serious studies, which means a huge computing task and a lot of CPU time, and this is actually another drawback of VOF method.

4.2 Introduction to OpenFOAM

OpenFOAM (Open source Field Operation And Manipulation) is an open source C++ library for numerical simulations in fluid (or continuum) mechanics [153]. C++ is an object-oriented language, which facilitates code reuse. OpenFOAM libraries has three main categories: pre-processing (e.g. meshing), solvers and post-processing (e.g. visualization) [154]. The most important are the two previous categories, pre-processing is in charge of the spacial discretization of fields and the definition of boundary conditions, while solvers give the solutions of the discretized PDEs. Each solver corresponds to a specific problem, thus a solver may be different from another one. Nonetheless, a solver can always be expressed in the form of a matrix equation [155]:

$$[A][x] = [b], \tag{4.21}$$

where $[A]$ is the matrix representing the discretized operators, $[b]$ is the vector of known fields and $[x]$ is the vector of unknown fields to be determined.

Although there are many different problems in fluid mechanics, just a few operators are often used, such as $\nabla\cdot$, ∇^2 and $\partial/\partial t$, thus they are written into reusable C++ classes in order to be shared by different problems. **fvm** and **fvc** are the namespaces that contain the functions representing those common operators. For example, $\nabla\cdot$ corresponds to **fvm::div()** or **fvc::div()**, ∇^2 corresponds to **fvm::laplacian()** or **fvc::laplacian()**, and $\partial/\partial t$ is represented as **fvm::ddt()** or **fvc::ddt()** in OpenFOAM [156]. The difference between these two namespaces is that **fvm** calculates implicit derivatives, whereas **fvc** calculates explicit ones [155].

$[x]$ and $[b]$ in equation (4.21) are also represented by C++ classes, known as field classes, for example **volScalarField**, **volVectorField** and **volTensorField**, which

defines a field at cell centers, and **surfaceScalarField**, **surfaceVectorField**, and **surfaceTensorField**, which defines a field at cell faces.

As discussed above, OpenFOAM is convenient to create new solvers for new problems by manipulating its libraries. In view of its versatility and flexibility, OpenFOAM has recently been applied to simulate many fluid phenomena, including two-phase flow. Among an important number of solvers that OpenFOAM possesses, the one that treats two-phase flow is *interFoam*, which is based on the VOF method. The performance of *interFoam* has been evaluated through several benchmark tests by previous researchers [157], they have shown that *interFoam* is able to capture the two-phase flow with sufficient accuracy. Specially, some other researchers have assessed its ability to simulate bubbles [140] [158] [159], which also showed that it can resolve bubble behavior with reasonable accuracy, as shown in Fig. 4.5 and 4.6. Besides, OpenFOAM also possesses a function called dynamic mesh, which allows a mesh refinement around the two-phase interface during computation [160], thus the interface can be better resolved with this function. The corresponding solver that can handle dynamic mesh is *interDyMFoam*, which is derived from *interFoam*, has been applied to simulate bubbles [161] [162] and droplets [163].

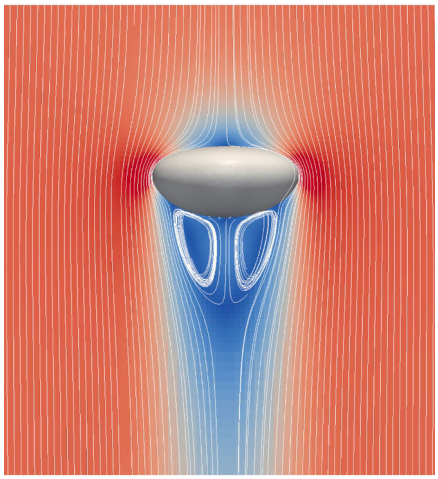

FIGURE 4.5: Simulation by *interFoam*: 3D rising bubble and velocity field around it, illustration from [158].

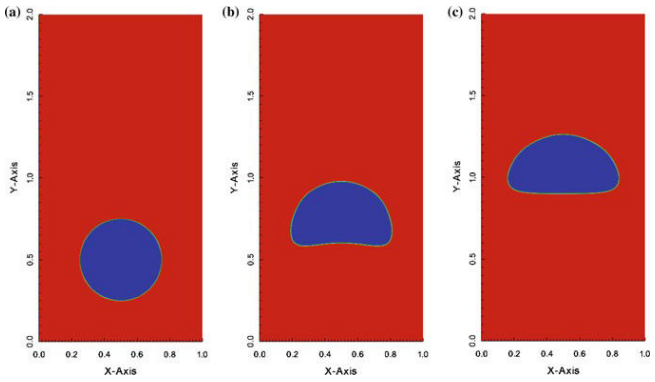

FIGURE 4.6: Simulation by *interFoam*: 2D rising bubble, illustration from [159].

4.3 2D simulations

In experiments, we need to adjust many experimental parameters to obtain significant results, thus we need to carry out a lot of tests on the experimental platform at the beginning of a series of experiments. It is the same case in CFD, tests are also necessary before running any meaningful simulation. There are two possible ways to carry out theses tests: 2D simulations or 3D simulations. However, as stated in section 4.1.4, VOF method is time-consuming, thus 3D simulations just for tests seems too extravagant. Therefore, 2D simulations are adopted to test the numerical parameters.

4.3.1 Numerical configurations

The 2D reactor for the tests is shown in Fig. 4.7. The configurations for 2D simulations are listed in table 4.2, and the boundary conditions in the language of OpenFOAM are listed in table 4.3.

TABLE 4.2: Configurations for 2D simulations

Parameter	Value
Geometry	2D rectangular
Dimensions	286 mm×580 mm (close to the experimental one)
Phases	air-water
Water height	500 mm
Sparger number	1
Sparger location	center of the bottom
Sparger size	diameter $d_s = 2$ mm (same as the experimental one)
Gas flow rate	0.4 L/s
Initial time step	0.001 s
Maximum Courant number	0.55, 0.75, 0.95
Mesh size	0.5 mm, 1 mm, 2 mm

TABLE 4.3: Boundary conditions for 2D simulations

	Volume fraction	Pressure	Velocity
Walls	*zeroGradient*	*fixedFluxPressure*	*fixedValue*
Atmosphere	*inletOutlet*	*totalPressure*	*pressureInletOutletVelocity*
Sparger	*inletOutlet*	*fixedFluxPressure*	*fixedValue*

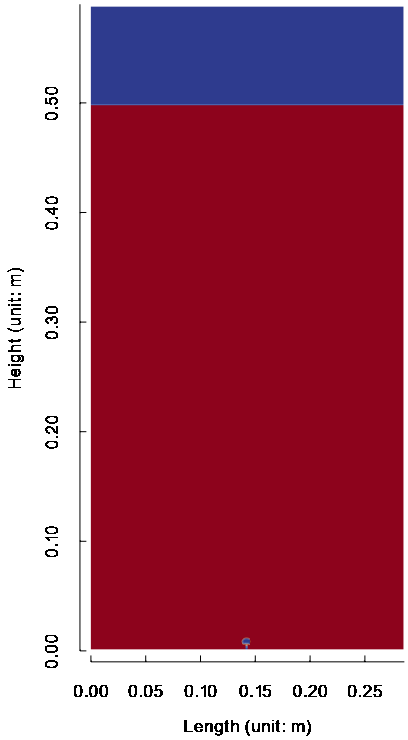

FIGURE 4.7: The dimensions of 2D simulations.

4.3.2 Numerical tests on Courant number

In numerical solutions of PDEs, Courant-Friedrichs-Lewy (CFL) condition is the necessary condition for convergence [164]. For one-dimensional problem, the CFL condition is

$$Co = \frac{|\vec{u}|\Delta t}{\Delta x} \leq Co_{\max}, \tag{4.22}$$

where Co is called Courant number, $|\vec{u}|$ is the magnitude of velocity, Δt is time step, Δx is mesh size, $Co_{\max}$ normally is 1 for explicit schemes, yet $Co_{\max}$ could be larger than 1 for implicit schemes. For example, we consider an one-dimensional advection equation

$$\frac{\partial \psi}{\partial t} + u\frac{\partial \psi}{\partial x} = 0, \tag{4.23}$$

if it is solved by explicit upwind scheme, then the modified equation is [165]

$$\frac{\partial \psi}{\partial t} + u\frac{\partial \psi}{\partial x} = \underbrace{\frac{u\Delta x}{2}(1 - Co)\frac{\partial^2 \psi}{\partial x^2}}_{\text{numerical diffusion}} + \mathcal{O}(\Delta^2 x), \tag{4.24}$$

where $\mathcal{O}$ is the truncation error, and (4.24) should satisfy

$$0 < Co \leq 1 \tag{4.25}$$

in order to converge the discretized advection equation.

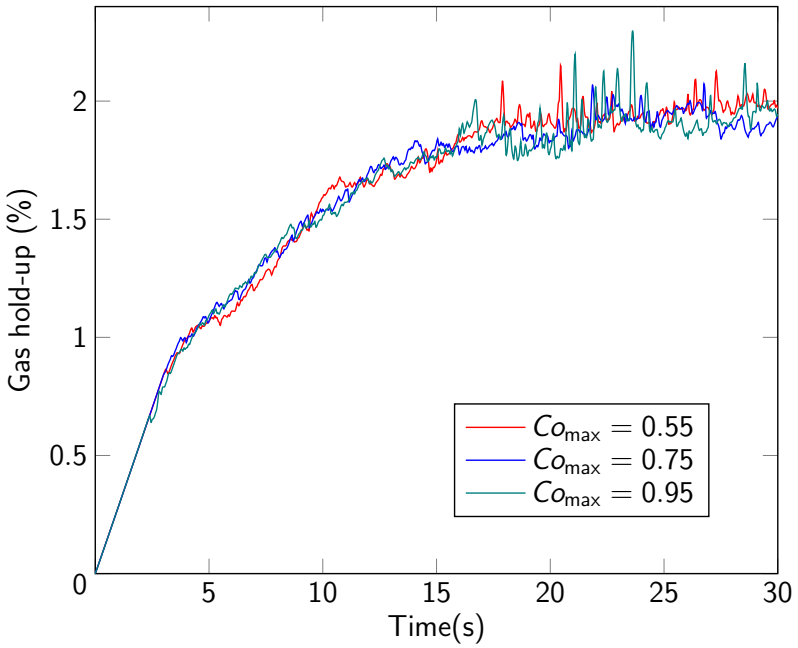

FIGURE 4.8: The influence of Courant number on gas hold-up, mesh size $\Delta x = 1$ mm.

Although Co needs to be less than 1, Co can not be too small either, since smaller Co implies smaller time step and larger numerical diffusion, consequently more computing time and larger error. Therefore, Co is an important parameter that should be regulated carefully. Fortunately, OpenFOAM is able to adjust time step automatically, in other words, OpenFOAM also possesses automatic adjustment of Co. However, $Co_{\max}$ is still undetermined, thus it should be tested by 2D simulations. Subsequently, we investigated the influences of $Co_{\max}$ on gas hold-up by fixing mesh size to 1 mm, as shown in Fig. 4.8, where we can see that $Co_{\max}$ has trivial influence on simulations. Therefore, we fixed

$$Co_{\max} = 0.75 \tag{4.26}$$

in order to investigate another numerical parameter: mesh size.

4.3.3 Numerical tests on mesh size

Mesh size is an important parameter in almost all sorts of the CFD simulations, since it can affect the accuracy of the results. For VOF method, the choice of mesh

size demands even more prudence, since an inappropriate mesh size may result in completely nonexistent results. For this reason, we tested different mesh sizes by virtue of the fixed maximum Courant number (4.26). In the entire computational domain, the only size that can be taken as a reference is the inner diameter of the sparger d_s, thus we tested three cases with mesh size

$$\Delta x = \begin{cases} 0.25d_s \\ 0.5d_s \\ d_s \end{cases}, \tag{4.27}$$

the results are shown in Fig. 4.9.

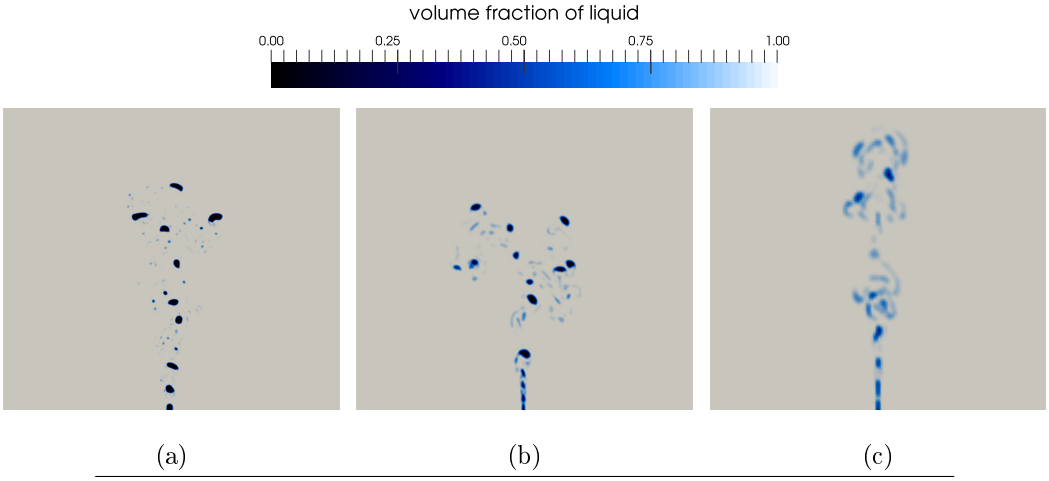

FIGURE 4.9: 2D simulations with different mesh sizes, at physical time $t = 1$ s. (a) $\Delta x = 0.25d_s$, (b) $\Delta x = 0.5d_s$, (c) $\Delta x = d_s$. d_s is the inner diameter of the sparger. (Scale: width of the numerical domain is 286 mm.)

In Fig. 4.9, we can observe the discrete bubbles when $\Delta x < d_s$, and the bubbles are certainly more distinct with smaller mesh size. However, discrete bubbles are hardly resolved when $\Delta x = d_s$, instead, the gas phase is more like "fumes" than bubbles, and we can also reasonably infer that the results will be even worse for $\Delta x > d_s$. Therefore, the conclusion is that mesh size[1] should be smaller than the inner diameter of the sparger in order to obtain genuine bubbles.

4.3.4 Preliminary validations

After the previous trials, we chose

$$Co_{\max} = 0.75, \Delta x = 0.5 \text{ mm} (= 0.25d_s) \tag{4.28}$$

for a relatively "formal" 2D simulation. Subsequently, we compared this 2D simulation with existing experimental data in order to have preliminary validations of the numerical approach by OpenFOAM. A feasible validation is to qualitatively compare bubble shape between simulations and experiments, since it exists an empirical map of shape regime for bubbles and drops [166], known as Grace diagram, as shown in Fig. 4.11. To identify the position of a simulated bubble in Grace diagram, we need

[1] or at least mesh size around sparger if it is not a uniform mesh

three dimensionless numbers

$$\mathrm{Eo} = \frac{(\rho_l - \rho_g) g d^2}{\sigma}, \tag{4.29}$$

$$\mathrm{Mo} = \frac{(\rho_l - \rho_g) g \eta_l^4}{\rho_l^2 \sigma^3}, \tag{4.30}$$

$$\mathrm{Re} = \frac{d|\vec{u}|}{\nu_l}, \tag{4.31}$$

where Eo is Eötvös number, which describes the ratio of buoyancy to surface tension forces [167], Mo is Morton number, which is used together with the Eötvös number to determine the shape of bubbles or drops moving in a surrounding fluid [168], Re is the Reynolds number for a moving bubble in liquid, which describes the ratio of bubble inertial to liquid viscosity [167], d is the equivalent spherical diameter.

Subsequently, we chose two bubbles from the 2D simulation, as shown in Fig. 4.10. For an air-water system, Morton number is about [169]

$$\mathrm{Mo} = 10^{-11}, \tag{4.32}$$

which is the same for both bubbles. And the equivalent diameter was

$$d_1 \approx 1.5 \text{ mm}, \tag{4.33}$$

$$d_2 \approx 4.5 \text{ mm}, \tag{4.34}$$

thus the Eötvös number for the two bubbles was

$$\mathrm{Eo}_1 = \frac{(\rho_l - \rho_g) g d_1^2}{\sigma} \approx \frac{1000 \times 10 \times (1.5 \times 10^{-3})^2}{70 \times 10^{-3}} \approx 0.3, \tag{4.35}$$

$$\mathrm{Eo}_2 = \frac{(\rho_l - \rho_g) g d_2^2}{\sigma} \approx \frac{1000 \times 10 \times (4.5 \times 10^{-3})^2}{70 \times 10^{-3}} \approx 3. \tag{4.36}$$

The bubble velocity was about the injecting gas velocity:

$$|\vec{u}_1| = |\vec{u}_2| \approx v_g = 0.2 \text{ m/s}, \tag{4.37}$$

thus the Reynolds number was

$$\mathrm{Re}_1 = \frac{d_1|\vec{u}_1|}{\nu_l} \approx \frac{1.5 \times 10^{-3} \times 0.2}{0.9 \times 10^{-6}} \approx 300, \tag{4.38}$$

$$\mathrm{Re}_2 = \frac{d_2|\vec{u}_2|}{\nu_l} \approx \frac{4.5 \times 10^{-3} \times 0.2}{0.9 \times 10^{-6}} \approx 1000. \tag{4.39}$$

Finally, we can find the corresponding location of each simulated bubble in Grace diagram, as shown in Fig. 4.11. We observed that bubble 1 was in spherical regime of Grace diagram, and it was indeed a stable spherical bubble according to simulation results in Fig. 4.10; bubble 2 was in wobbling regime of Grace diagram, and it also ceaselessly oscillated in the simulation. In brief, the shape of simulated bubbles met the one in the empirical diagram. Therefore, we can preliminarily conclude that OpenFOAM is able to consistently catch bubble behaviors.

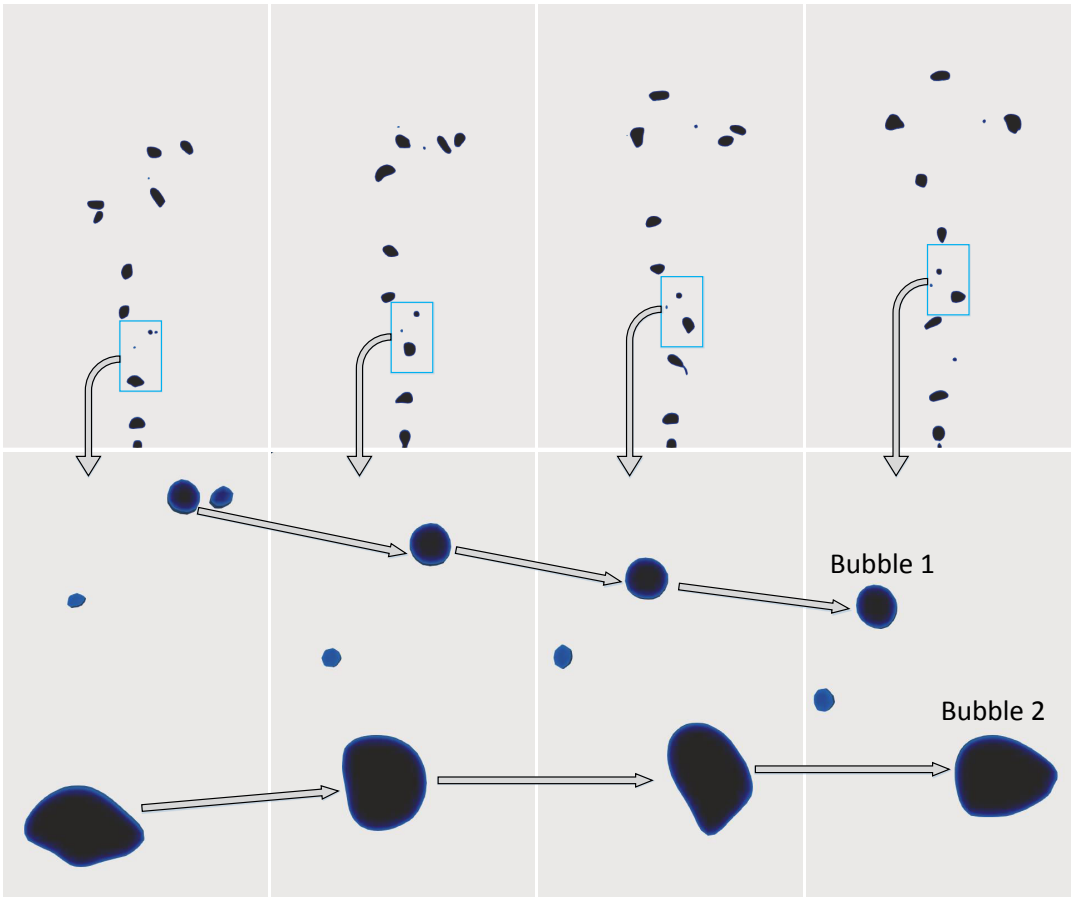

FIGURE 4.10: Two bubbles in different shape regime. Conditions: $Co_{\max} = 0.75$, $\Delta x = 0.5$ mm, injecting gas velocity $v_g = 0.2$ m/s. The equivalent diameter $d_1 \approx 1.5$ mm, $d_2 \approx 4.5$ mm.

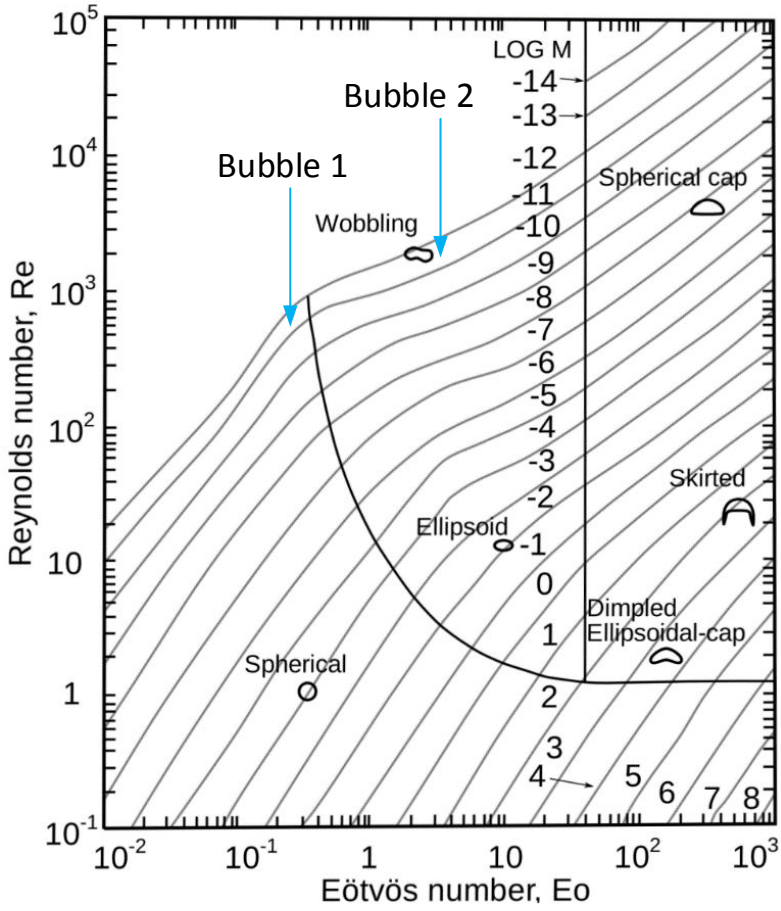

FIGURE 4.11: Shape regime map for bubbles and drops [166], illustration from [170].

4.4 3D simulations

In previous discussions, we achieved some preparatory investigations by 2D simulations. Even though 2D simulations were already able to reveal some facts about bubbles, it has been found that 2D simulations may have obvious discrepancy with experiments in terms of some hydrodynamic characteristics of bubbles [58] [171] [172]. Therefore, explorations in 2D are not sufficient, we should continue carrying out the real 3D simulations. In this section, bubble behaviors at different gas flow rate were studied by 3D simulations.

4.4.1 Numerical configurations

For 3D simulations, we could only investigate a small volume around the sparger due to the time-consuming feature of VOF method, and the dimensions (length, width and height) of the 3D numerical domain were approximately reduced by a factor of 20 relative to the dimensions of the lab reactor, yet the dimensions of the nozzle kept the same, as shown in Fig. 4.12. Simulations in this small volume are still reliable, since the rest of liquid almost has no influence on bubble formation, and the effect of liquid level is also negligible [173]. Moreover, even though the computational domain was reduced, the amount of computation is still too huge for a PC. Therefore, the computing tasks were performed on the supercomputer Mésocentre[2] by running in parallel, which is implemented in OpenFOAM by domain decomposition.

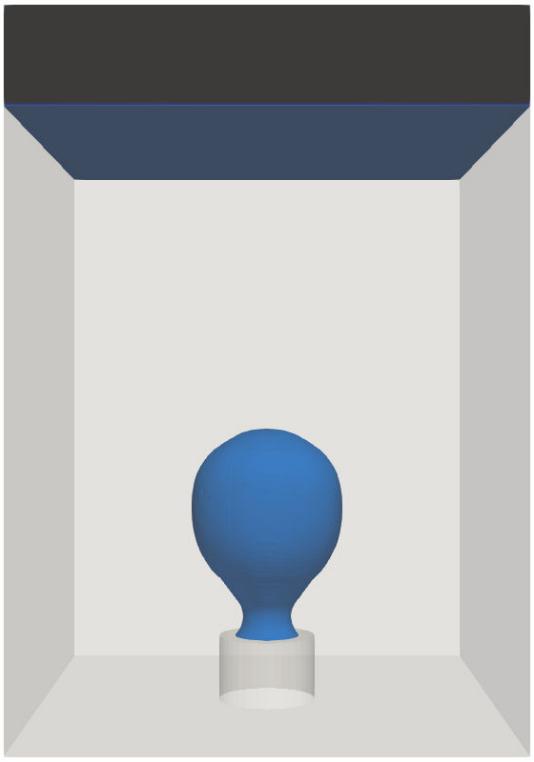

FIGURE 4.12: The mini-reactor in 3D simulations. (Numerical domain: $14 \times 14 \times 20$ mm, exterior diameter of the nozzle: 3 mm.)

[2]Computing center of CentraleSupélec and École Normale Supérieure Paris-Saclay supported by CNRS and Région Île-de-France (http://mesocentre.centralesupelec.fr/).

In the 3D simulations, the sparger kept the same dimensions as the real one in the experiments. Besides, the water height was reduced to 17 mm since we would like to track the bubble in a numerical window whose area was close to the recording window of the video camera. Physical properties were as the one of ultra-pure 20 °C water, as it was used for the experiments (Ref. Tab. 1). More detailed configurations for 3D simulations are summarized in table 4.4.

The computational domain was initially filled with still water, leading to the subsequent initial conditions

$$\vec{u} = \vec{0}, \tag{4.40}$$
$$p = 101325 + \rho_{\text{water}} g h, \tag{4.41}$$
$$\alpha_l = 1. \tag{4.42}$$

The velocities of injecting gas were calculated from the measured flow rate in table 3.1. Therefore, the following boundary conditions were applied at the inlet (sparger):

$$\vec{u} \cdot \hat{n} = -\frac{Q}{A_{\text{inlet}}}, \tag{4.43}$$
$$\nabla p \cdot \hat{n} = 0, \tag{4.44}$$
$$\alpha_l = 0, \tag{4.45}$$

where $\hat{n}$ was defined in equation (4.18). While the following ones governed the outlet (atmosphere):

$$\nabla \vec{u} \cdot \vec{n} = \vec{0}, \tag{4.46}$$
$$p = 101325 \text{ Pa}, \tag{4.47}$$
$$\nabla \alpha_l \cdot \vec{n} = 0. \tag{4.48}$$

The expressions of these boundary conditions in OpenFOAM are still those in table 4.3.

Based on the experience with 2D tests, we assigned smaller mesh size to the region around the sparger, as shown in Fig. 4.13. Besides, dynamic mesh is also turned on in order to better resolve the gas-liquid interface, as shown in Fig. 4.14.

TABLE 4.4: Configurations for 3D simulations

Parameter	Value
Geometry	3D rectangular
Dimensions	14 mm×14 mm×20 mm
Phases	air-water
Water height	17 mm
Sparger number	1
Sparger location	center of the bottom
Sparger dimensions	inner diameter: 2 mm outer diameter: 3 mm height: 2 mm
Gas flow rate	those in table 3.1
Initial time step	0.0001 s
Maximum Courant number	0.75
Initial mesh cell number	663350
Cell shape	hexahedral
Dynamic mesh	yes
Processor number	24
Computing time	≈ 1 week for 1 detached bubble

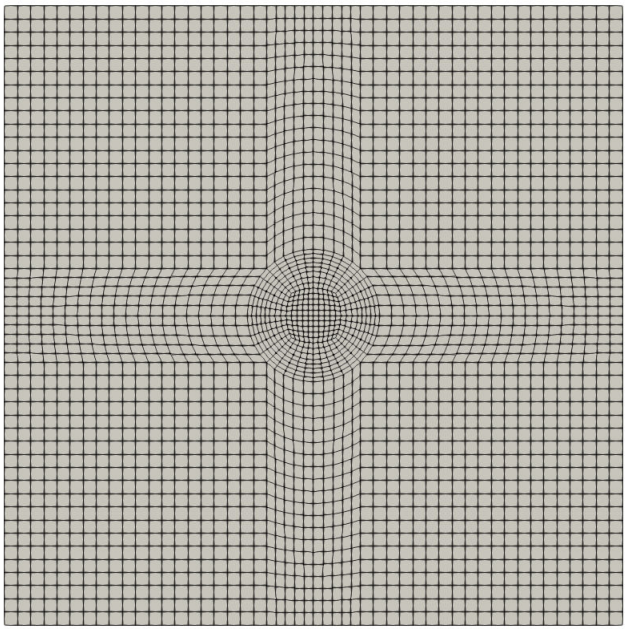

FIGURE 4.13: The bottom view of the meshed computational domain.

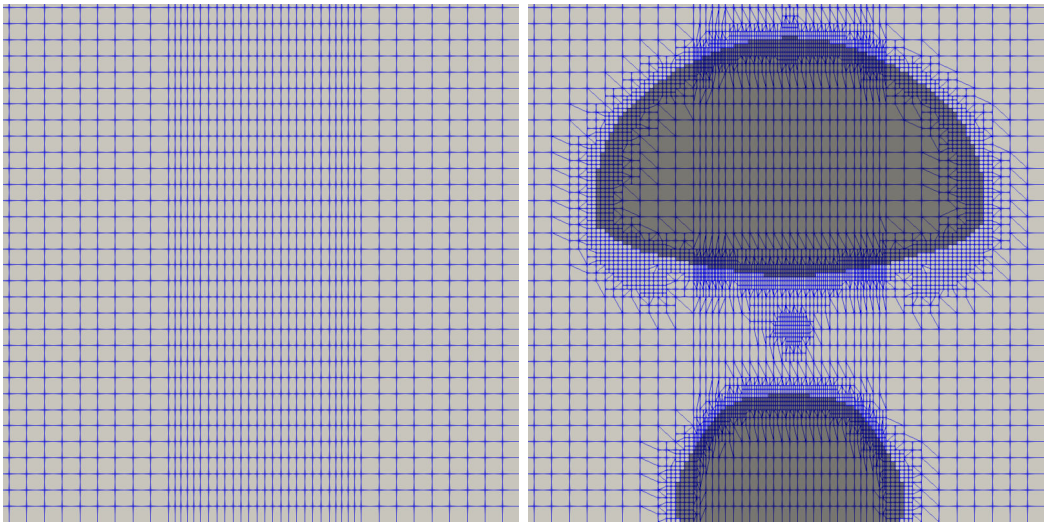

FIGURE 4.14: Dynamic mesh is "activated" as soon as the mesh meet the interface, illustration from simulation with VFC 3%.

4.4.2 Visual validations

After a long computation on the supercomputer (about one month for one flow condition), we obtained about $2 \sim 4$ bubbles for each flow rate, which should be validated by the experiments. Therefore, first we visually compared the temporal evolution of bubbles in simulations and experiments, as shown in Fig 4.15-4.22. From the visual comparisons, we observed that bubble evolutions in simulations were basically in agreement with those in experiments over a wide range of flow rate, i.e. VFC $1\% \sim 20\%$. At higher flow rate, e.g. VFC 30%, two adjacent bubbles were very close, consequently, two possible situations could take place in simulations. First situation was that two bubbles appeared to merge, yet actually not, which captured well the corresponding situation in experiments, as shown in Fig 4.21. Second situation was that two bubbles coalesced into a single larger bubble, as shown in Fig. 4.22, which was not really the case in experiments: two bubbles did approach each other, yet they did not finally merge. The discrepancies that are observed in terms of local curvature can be related to a well known problem of OpenFOAM VOF solver *interFoam*. Indeed, its weak coupling of the surface tension effect into the momentum balance can lead to inaccuracies for capillarity dominated phenomena. Several techniques to better resolve the interface or implicitly compute surface tension in the force balance have been proposed in the literature [174] [171] [175]. We did not apply those techniques because, in our case, the flow is controlled by buoyancy.

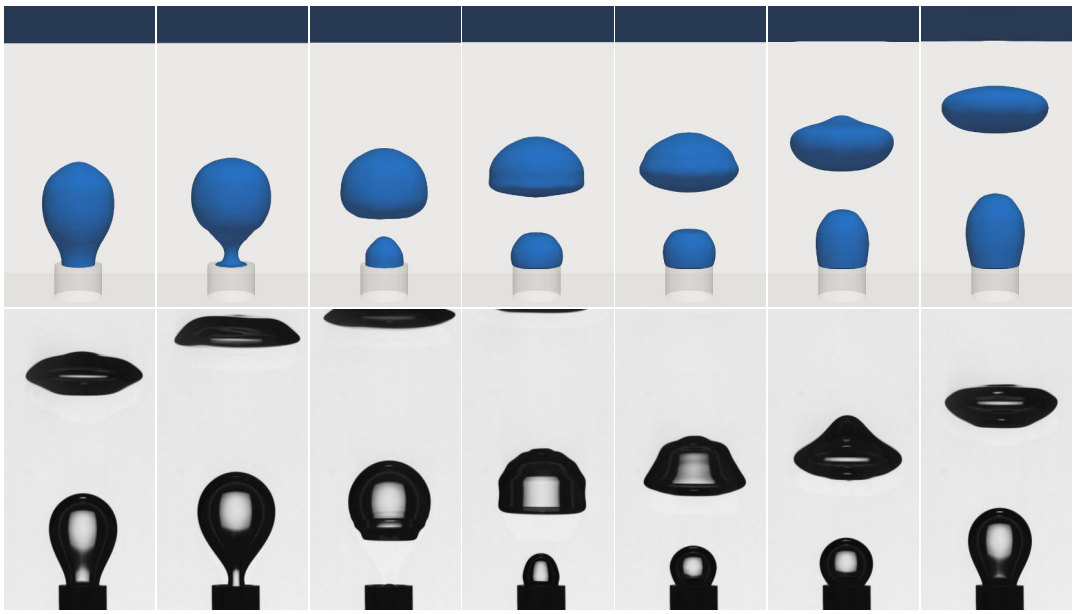

FIGURE 4.15: Comparison of bubble evolution in simulations and in experiments. Upper images are from simulations, lower images are from experiments, they have the same scale: 3 mm = 126 pixels. The nozzle diameter in simulations is the same as the one in experiments, i.e. 3 mm. Time interval between images in upper and lower row is similar. VFC: 1%.

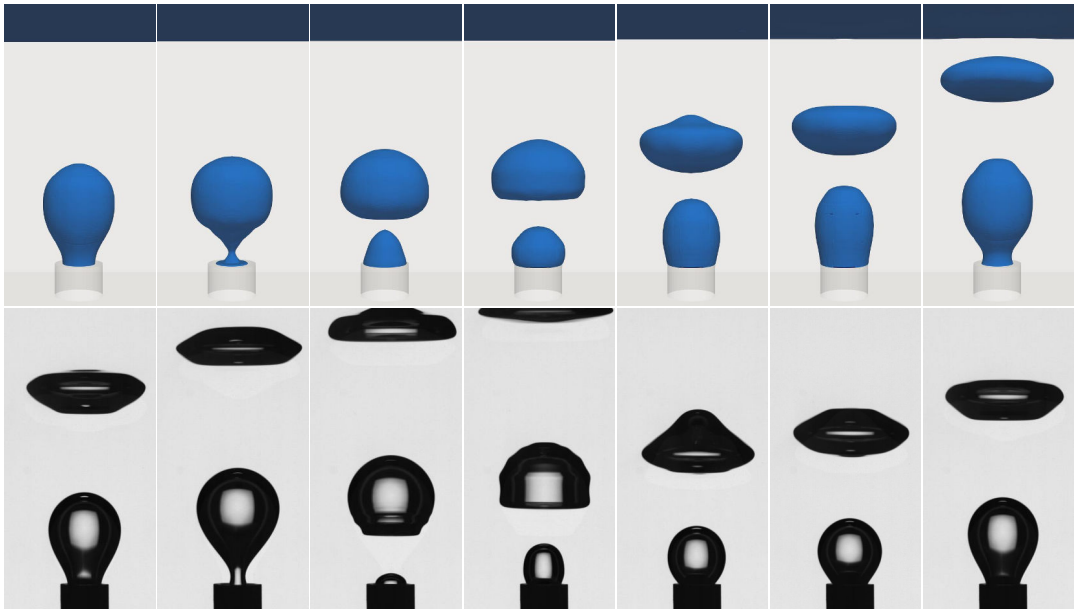

FIGURE 4.16: Comparison of bubble evolution in simulations and in experiments. Upper images are from simulations, lower images are from experiments, they have the same scale: 3 mm = 126 pixels. The nozzle diameter in simulations is the same as the one in experiments, i.e. 3 mm. Time interval between images in upper and lower row is similar. VFC: 3%.

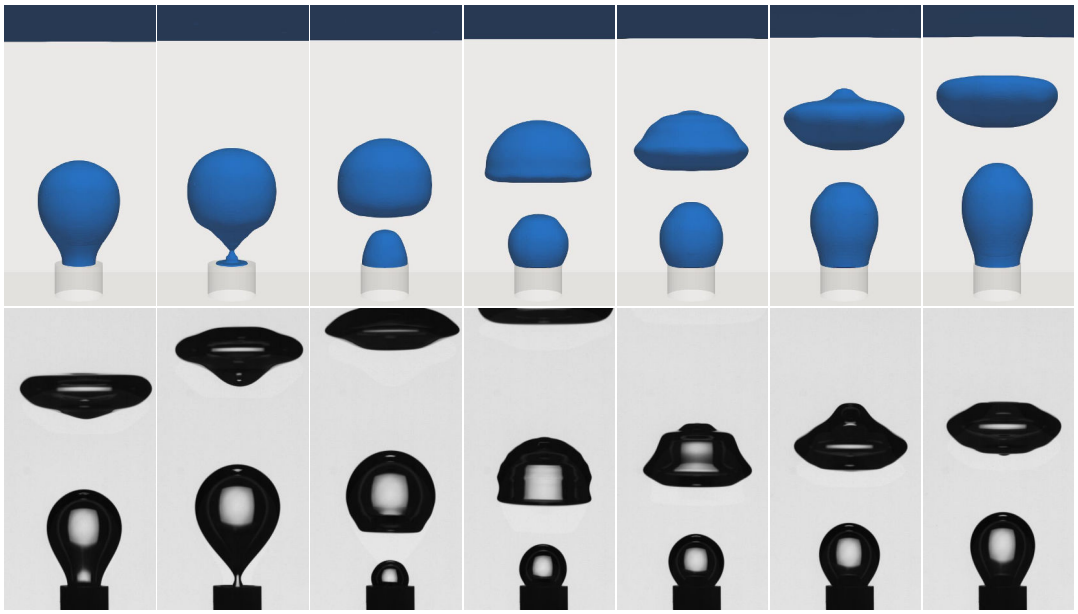

FIGURE 4.17: Comparison of bubble evolution in simulations and in experiments. Upper images are from simulations, lower images are from experiments, they have the same scale: 3 mm = 126 pixels. The nozzle diameter in simulations is the same as the one in experiments, i.e. 3 mm. Time interval between images in upper and lower row is similar. VFC: 6%.

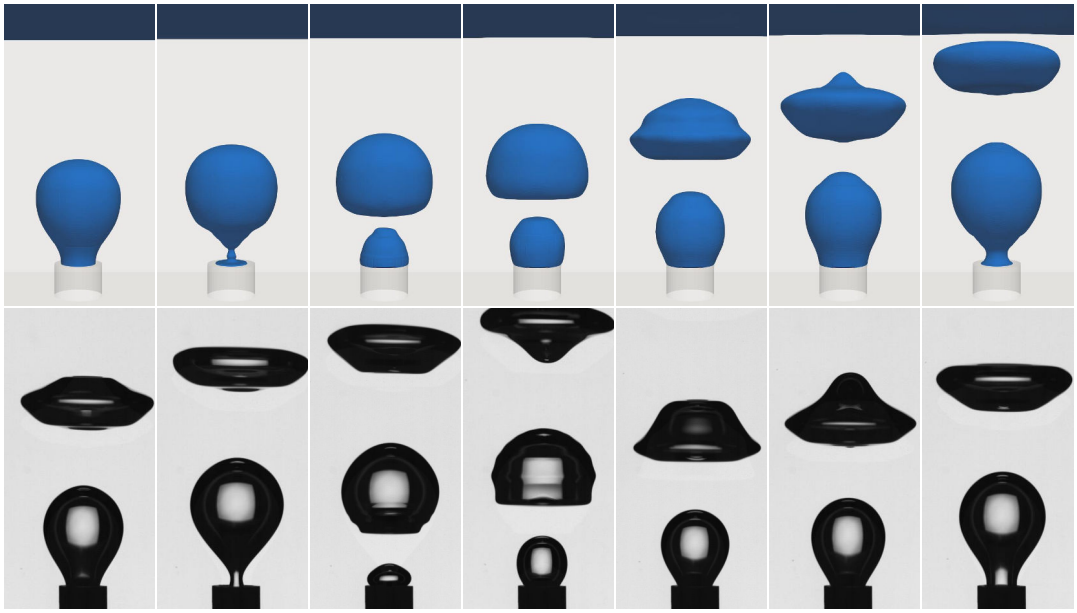

FIGURE 4.18: Comparison of bubble evolution in simulations and in experiments. Upper images are from simulations, lower images are from experiments, they have the same scale: 3 mm = 126 pixels. The nozzle diameter in simulations is the same as the one in experiments, i.e. 3 mm. Time interval between images in upper and lower row is similar. VFC: 9%.

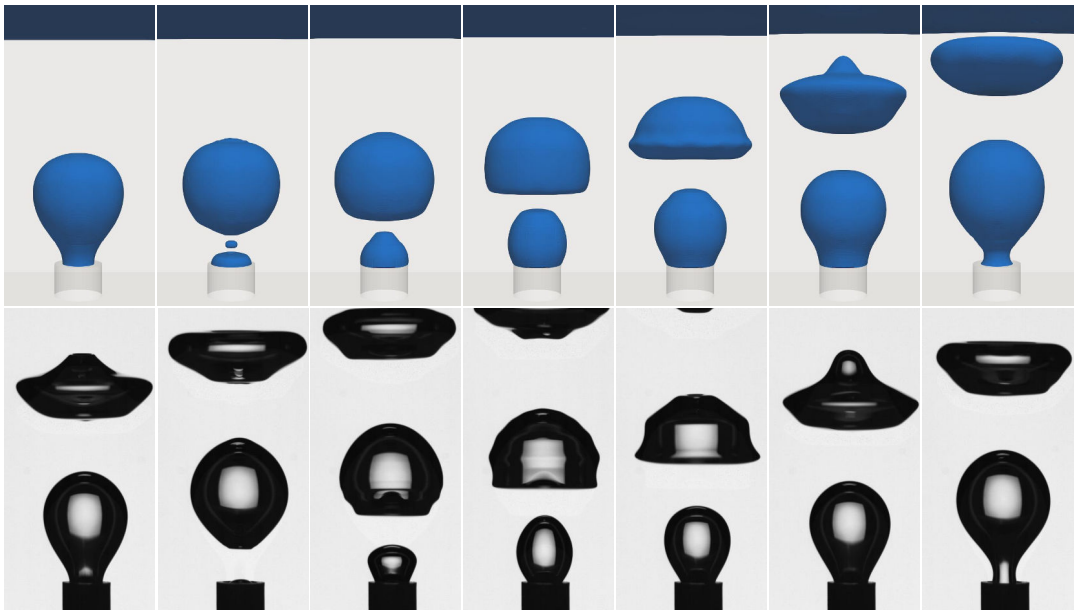

FIGURE 4.19: Comparison of bubble evolution in simulations and in experiments. Upper images are from simulations, lower images are from experiments, they have the same scale: 3 mm = 126 pixels. The nozzle diameter in simulations is the same as the one in experiments, i.e. 3 mm. Time interval between images in upper and lower row is similar. VFC: 12%.

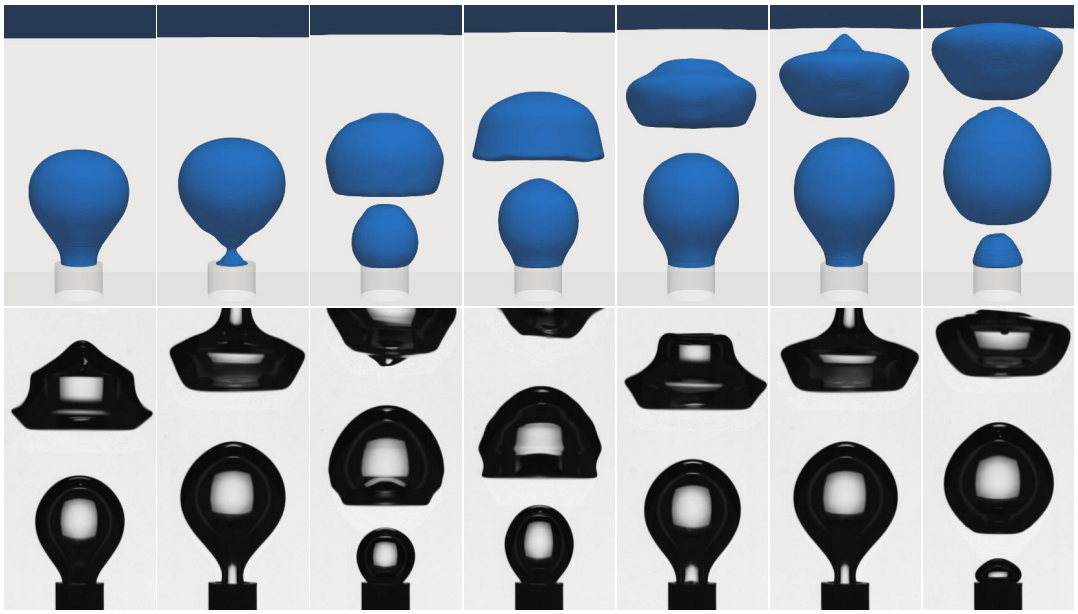

FIGURE 4.20: Comparison of bubble evolution in simulations and in experiments. Upper images are from simulations, lower images are from experiments, they have the same scale: 3 mm = 126 pixels. The nozzle diameter in simulations is the same as the one in experiments, i.e. 3 mm. Time interval between images in upper and lower row is similar. VFC: 20%.

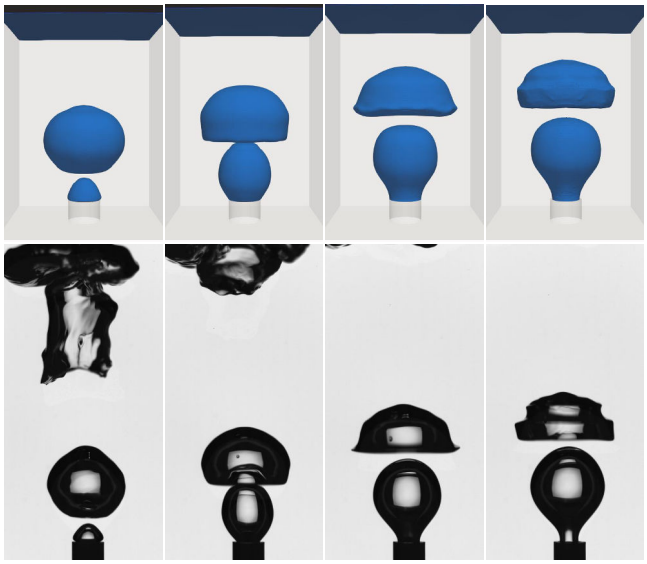

FIGURE 4.21: Comparison of bubble evolution in simulations and in experiments. Upper images are from simulations, lower images are from experiments, they have the same scale: 3 mm = 80 pixels. The nozzle diameter in simulations is the same as the one in experiments, i.e. 3 mm. Two bubbles did not finally merge in both simulations and experiments. Time interval between images in upper and lower row is similar. VFC: 30%.

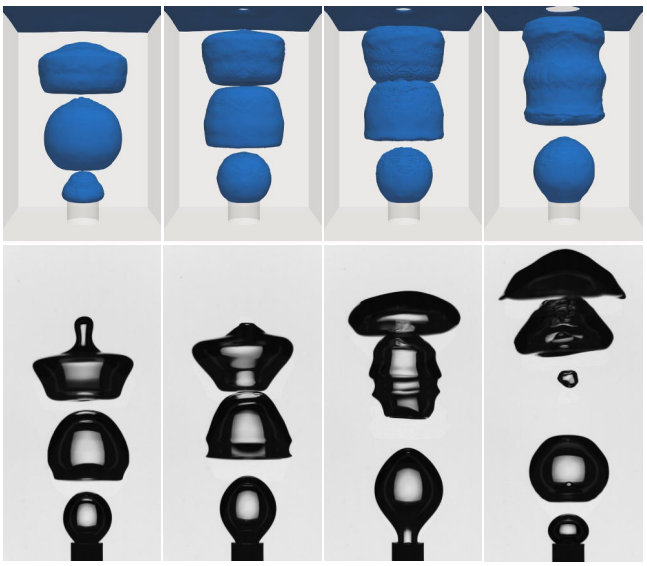

FIGURE 4.22: Comparison of bubble evolution in simulations and in experiments. Upper images are from simulations, lower images are from experiments, they have the same scale: 3 mm = 80 pixels. The nozzle diameter in simulations is the same as the one in experiments, i.e. 3 mm. Two bubbles finally merged in simulations, not in experiments. Time interval between images in upper and lower row is similar. VFC: 30%.

4.4.3 Bubble volume

In previous discussions, 3D simulations were validated by visual comparisons with experiments, yet they are not sufficient for more quantitative validations. Therefore, we should also compare simulations with experiments in terms of some important parameters of bubble behaviors. We begun this quantitative comparison with bubble volume, since bubble volume has important influence on cell growth as mentioned in in section 2.7.

The bubble volume were obtained from simulations by post-processing of OpenFOAM. First of all, we observed that the volume of simulated bubbles increased a little bit for the first bubbles until reaching a constant value, which has already been observed in other research [113]. Second, we also calculated the averaged volume V_{sim} of the bubbles generated at each flow rate. Subsequently, bubble volume V_{sim} and V_{img} (from experiments) were compared for different flow rates, as shown in Fig. 4.23. The bubble volume from simulations were in good agreement with the one from experiments, since their relative difference was less than 15%. And the discrepancies between experimental and numerical values were not statistically significant as their error bars overlapped.

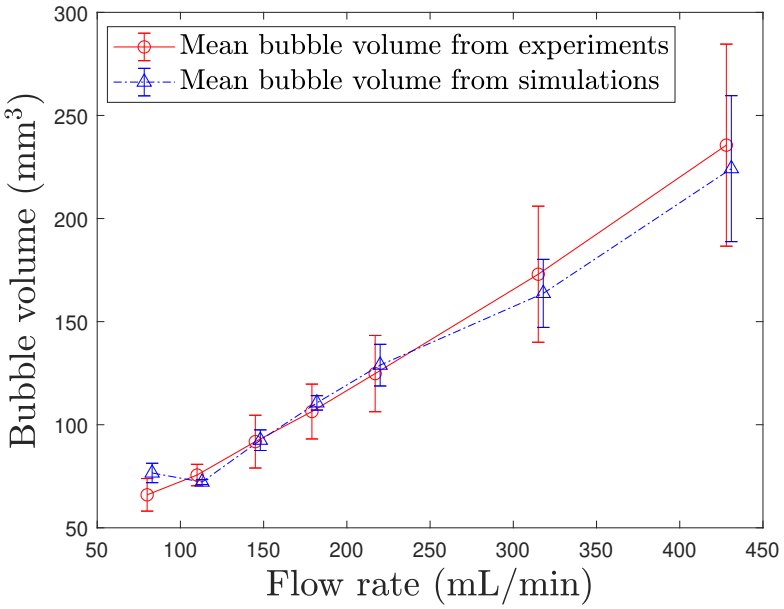

FIGURE 4.23: Comparison of bubble volumes obtained from simulations (V_{sim}) and experiments (V_{img}). The vertical bar is the standard deviation. The curve for simulations are slightly shifted to the right to better distinguish the two curves.

However, 3D simulations could not reproduce the experimental results in very detail. For example, in section 3.5.3, the results showed that the bubble volume was distributed, which could be revealed only after analyzing thousands of bubbles. In simulations, due to the high computing time, only a few bubbles were calculated. Therefore, the numerical tool was not able to represent the polydispersity of the bubble volume within the constraint of the present computing power.

Besides, as the bubble volume was correctly computed by simulations for each flow rate, the bubbling frequency obtained from simulations would also be in accordance

with the experimental one, since bubbling frequency can be estimated by

$$\mathfrak{f} = \frac{Q}{V}. \tag{4.49}$$

Therefore, we may conclude that the proposed numerical tool is capable of properly capturing a train of bubbles in terms of bubble volume and bubbling frequency.

4.4.4 Bubble shape evolution

The evolution of bubble shape factors is another important way to quantitatively validate the simulations. Note that a code was already developed in Matlab to calculate the bubble shape factors from the experimental images, thus the same code was reused to calculate the shape factors of simulated bubbles. Subsequently, an experimental bubble and a simulated bubble should be chosen in order to carry out this validation. The experimental bubble for the validation was arbitrarily chosen from the highest bar in Fig. 3.18(a), since the shape factors were quite similar for all the bubbles in this bar, as shown in Fig. 3.23. It was the similar situation for the few simulated bubbles: their evolutions of shape factors were also close, thus the first detached bubble was chosen as the simulated bubble for the validation, just for the sake of a clearer representation. In addition, the start and end frames might not be strictly corresponding between simulations and experiments, since the frame rate in simulations was higher than the one in experiments due to the limited memory of the video camera.

Similarly, the bubble shape factors in simulations and experiments for different flow rates were compared in Fig. 4.24-4.30. We can see that the simulation correctly represents the trend of bubble shape evolution observed by the video camera with a relative difference of about 10%. Specially, in experiments at VFC 30%, aspect ratio and circularity had a sharp change (there was a plateau in the evolution of bubble shape factors) due to the contact between bubbles (not coalescence, since they were separated finally), which was also properly represented by OpenFOAM, as shown in Fig. 4.30. These results show that OpenFOAM is both appropriate for and efficient in representing the bubble shape evolution with sufficient accuracy.

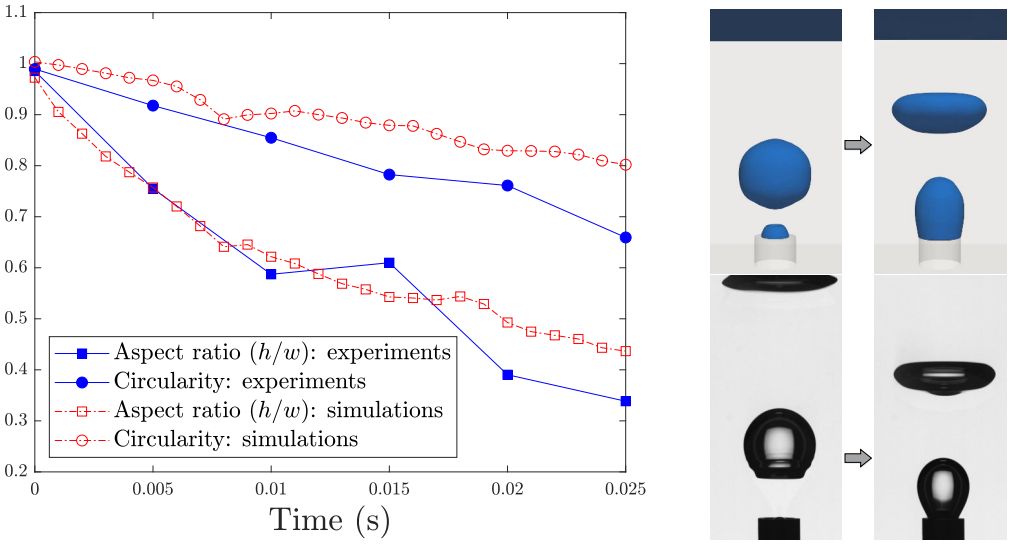

FIGURE 4.24: Evolution of bubble shape factors. The images have the same scale : 3 mm = 126 pixels. VFC: 1%.

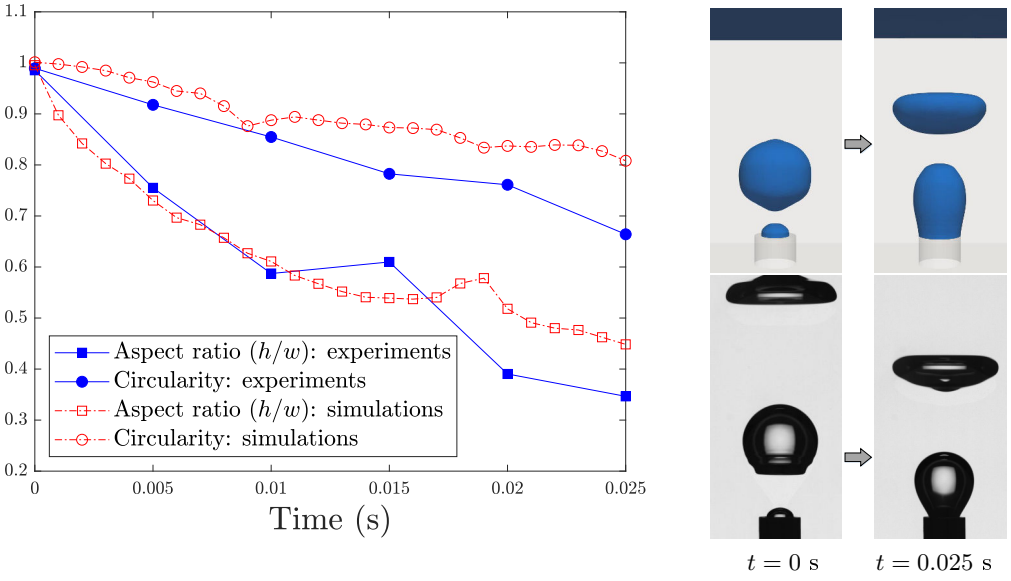

FIGURE 4.25: Evolution of bubble shape factors. The images have the same scale : 3 mm = 126 pixels. VFC: 3%.

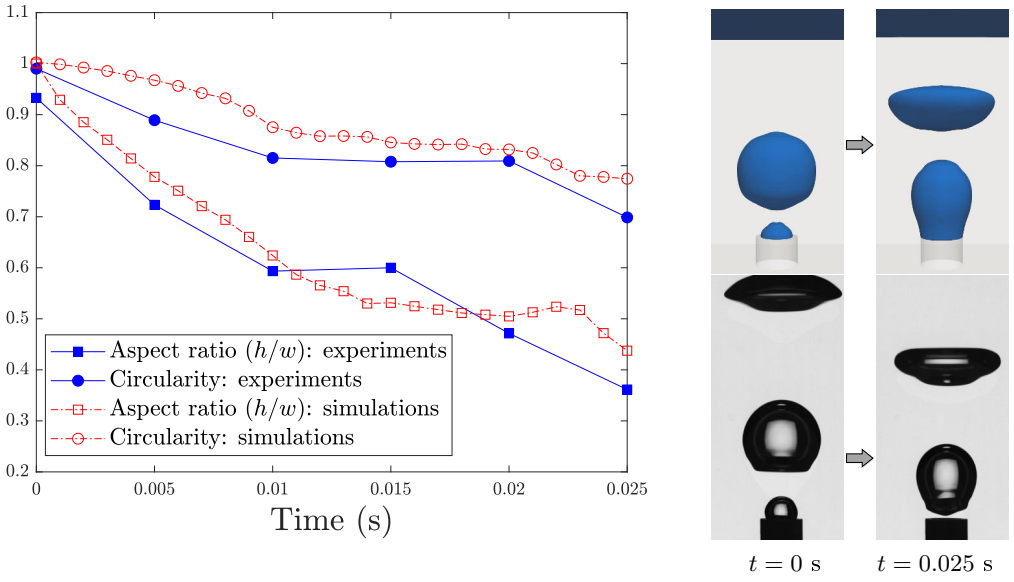

FIGURE 4.26: Evolution of bubble shape factors. The images have the same scale : 3 mm = 126 pixels. VFC: 6%.

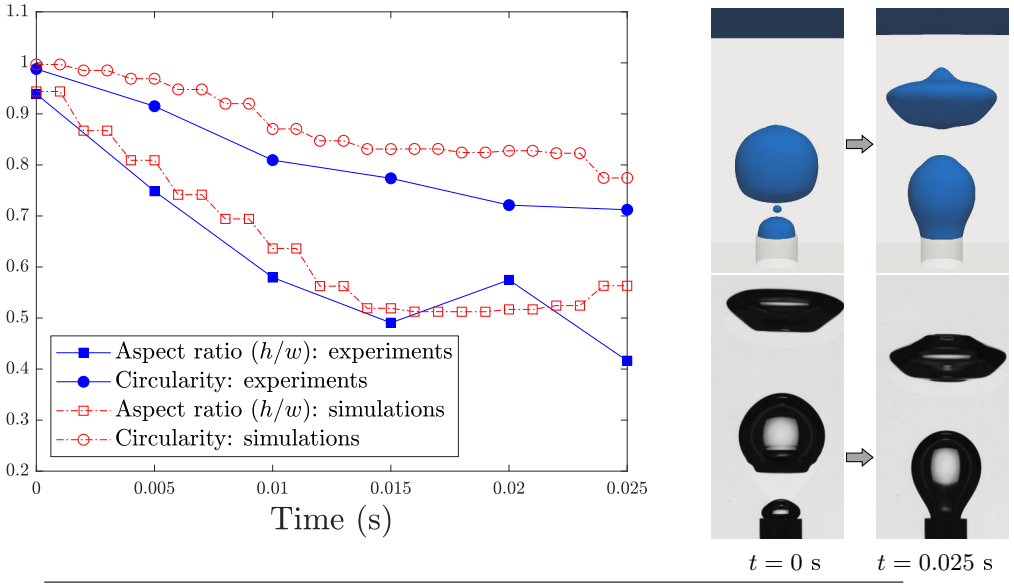

FIGURE 4.27: Evolution of bubble shape factors. The images have the same scale : 3 mm = 126 pixels. VFC: 9%.

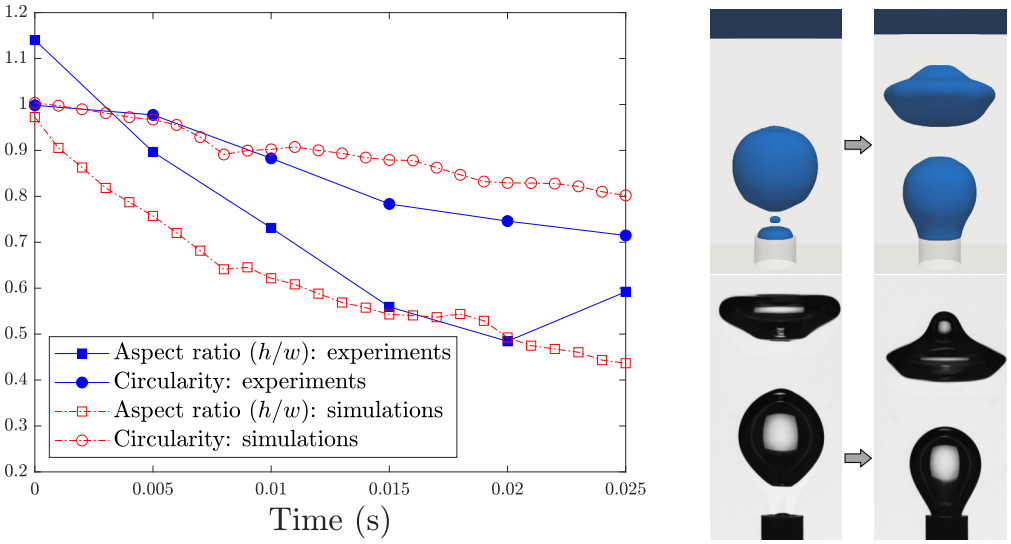

FIGURE 4.28: Evolution of bubble shape factors. The images have the same scale : 3 mm = 126 pixels. VFC: 12%.

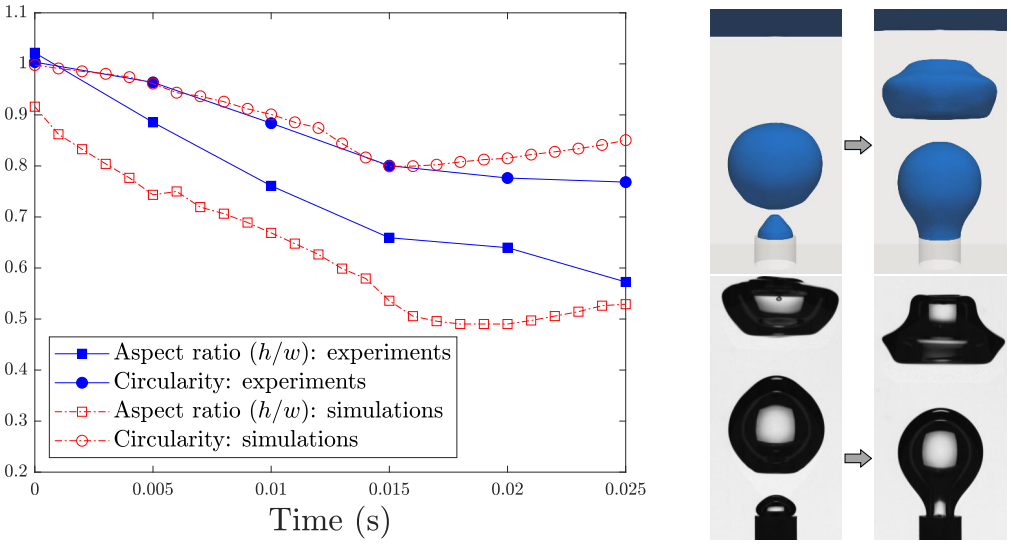

FIGURE 4.29: Evolution of bubble shape factors. The images have the same scale : 3 mm = 126 pixels. VFC: 20%.

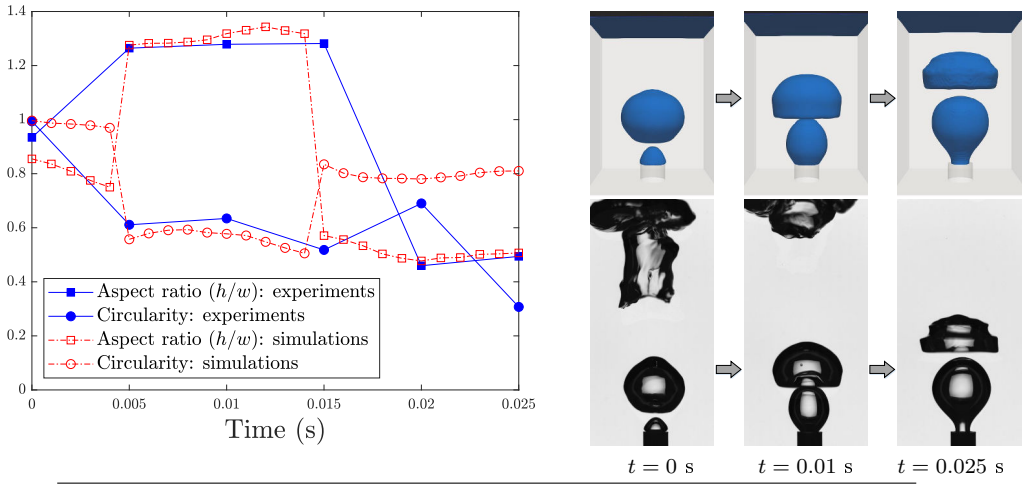

FIGURE 4.30: Evolution of bubble shape factors. The images have the same scale : 3 mm = 80 pixels. VFC: 30%.

4.5 Conclusions

In this chapter, we first introduced the fundamentals of VOF method and OpenFOAM, which were the numerical tools adopted in our work to simulate bubbly flow. Subsequently, we carried out several 2D numerical tests on the proposed numerical tool in order to obtain the appropriate numerical parameters. We found that the influence of maximum Courant number was trivial, yet the the influence of mesh size was crucial: it should be less than the inner diameter of the sparger, otherwise the results would be unreal. With the experiences in 2D simulations, we successfully performed complete 3D simulations, whereafter we found that the bubble behaviors, such as bubble volume, bubble shape evolution in 3D simulations were in good agreement with the experimental ones. In brief, the proposed numerical tool proved to be capable of correctly representing the bubble behaviors over a relatively wide range of gas flow rate.

Chapter 5

Preparing a complete model

In the previous chapters, we mainly investigated the bubble behaviors under different flow conditions. In this chapter, we first test the competence of the numerical tool in simulating the hydrodynamics of the two-phase flow in order to prepare a complete model of a photobioreactor. Furthermore, other essential kernels for preparing such complete model are also discussed.

5.1 Quasi-steady state of two-phase flow

Before the injection of gas, the liquid is obviously in a steady state (stagnant condition). However, this steady state will be broken from the moment that gas is injected, since the bubbles will start to stir the liquid. Nevertheless, after a certain time of bubbling, the two-phase flow will arrive a quasi-steady state, which implies that some physical quantities are almost time-independent. For example, the volume-averaged momentum

$$\overline{\mathfrak{p}} = \frac{1}{V}\int [\rho_l \alpha_l + \rho_g(1-\alpha_l)]|\vec{u}|dV \tag{5.1}$$

may become constant in the quasi-steady state.

FIGURE 5.1: The cylindrical reactor used for the investigation of hydrodynamics.

The minimum time required to obtain the quasi-steady state is an important parameter of a photobioreactor. However, it is not easy to carry out experiments to investigate this parameter, since it may require the knowledge of several vector and scalar fields in the whole reactor. Therefore, a more practical way is the CFD simulations. In order to identify the quasi-steady state, *interDyMFoam*, the OpenFOAM solver for two-phase flow, was modified to include the $\overline{\mathfrak{p}}$ into the numerical results. Afterwards, $\overline{\mathfrak{p}}$ was computed by this modified solver for a cylindrical reactor with the volume of 1 L, as shown in Fig. 5.1, since a cylindrical shape is more common in the industrial reactors [176] [177]. The numerical setup for the cylindrical reactor is reported in table 5.1.

TABLE 5.1: Numerical setup for the cylindrical reactor

Parameter	Value
Geometry	3D cylindrical
Dimensions	$D = 100$ mm, $H = 127$ mm
Volume	1 L
Volume of culture medium	0.8 L
Phases	air-water
Sparger number	1
Sparger location	center of the bottom
Sparger dimensions	inner diameter: 2 mm outer diameter: 4 mm height: 2 mm
Gas flow rate	179.1 L/min (VFC 9%)
Initial time step	0.0001 s
Maximum Courant number	0.75
Initial mesh cell number	4635580
Cell shape	tetrahedral
Dynamic mesh	yes
Processor number	24
Computing time	$\approx$ 1 week for 2 s physical time

The evolution of $\overline{\mathfrak{p}}$ is shown in Fig. 5.2, where we observe that $\overline{\mathfrak{p}}$ tends to be constant after about 4 s. This result, in terms of characteristic time, is well-known

for any biologist. Therefore, apart from bubbling, the numerical tool is also capable of reproducing some hydrodynamic phenomena of two-phase flow.

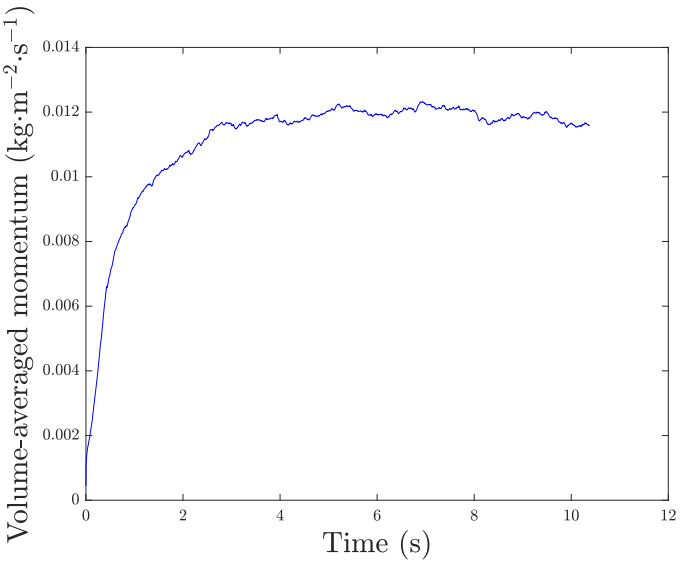

FIGURE 5.2: The evolution of volume-averaged momentum.

5.2 Scalar transport

In order to have a complete physical-biological model, it is necessary to study the transport of some scalar quantities, such as the temperature, pH of the liquid, and the concentration of some chemical substances necessary for the algal growth. A liquid tracer transports only in liquid phase, and its transport is described by the convection-diffusion equation

$$\frac{\partial(\alpha_l\psi_l)}{\partial t} + \underbrace{\nabla\cdot(\alpha_l\psi_l\vec{u})}_{\text{convection}} = \underbrace{\mathcal{D}\nabla^2(\alpha_l\psi_l)}_{\text{diffusion}}, \tag{5.2}$$

where ψ_l is the scalar that characterizes the liquid tracer, $\mathcal{D}$ is the diffusivity of tracer in the liquid phase. However, a gaseous tracer, such as CO_2, can transport in both phases, thus its transport is described by [156]

$$\frac{\partial\psi_g}{\partial t} + \nabla\cdot(\psi_g\vec{u}) = \nabla\cdot\left[\mathcal{D}_e\frac{1-H}{\alpha_l H + (1-\alpha_l)}\nabla(\alpha_l\psi_g)\right], \tag{5.3}$$

where ψ_g is the scalar that characterizes the gaseous tracer, H is the Henry coefficient, and $\mathcal{D}_e$ is the volume-weighted diffusivity

$$\mathcal{D}_e = \frac{\mathcal{D}_l\mathcal{D}_g}{\alpha_l\mathcal{D}_g + (1-\alpha_l)\mathcal{D}_l}, \tag{5.4}$$

where $\mathcal{D}_l, \mathcal{D}_g$ is the diffusivity of gaseous tracer in liquid phase, gas phase, respectively.

The transport of liquid tracer in liquid phase is also known as the mixing in the liquid phase. A good mixing, i.e. uniformly distributed scalar quantities in the liquid phase, is one of the major objectives in the design of a photobioreactor. Only after entering a quasi-steady state, the homogenization becomes possible for some initially

heterogeneous scalar fields. The time required to attain homogeneous state is called mixing time, which is another important parameter for the design and operation of a photobioreactor [178]. To evaluate this mixing time, a common technique is to distribute an amount of tracer at one point, and mixing time can be obtained from the variation of the concentration of the tracer at the tracer source or another point [179]. This technique can also be easily carried out by the CFD simulations.

In our case, the reactor was still the one in Fig. 5.1, and a droplet of liquid tracer was added into the liquid phase at quasi-steady state, as if it was dropped from the top of the reactor, as shown in Fig. 5.3. Subsequently, we followed the normalized variance - i.e. variance divided by its initial value - of this tracer concentration over the liquid phase. Fig. 5.4 reports the evolution of this quantity. As one can see, less than 0.5 second is required for the normalized variance to fall below 5%. This duration is far below any relevant microbiological characteristic time. Therefore, it can be concluded that the mixing of this photobioreactor is well-suited for microalgae growth. This also illustrates the capability of the proposed numerical tool to assess for the quality of a photobioreactor mixing.

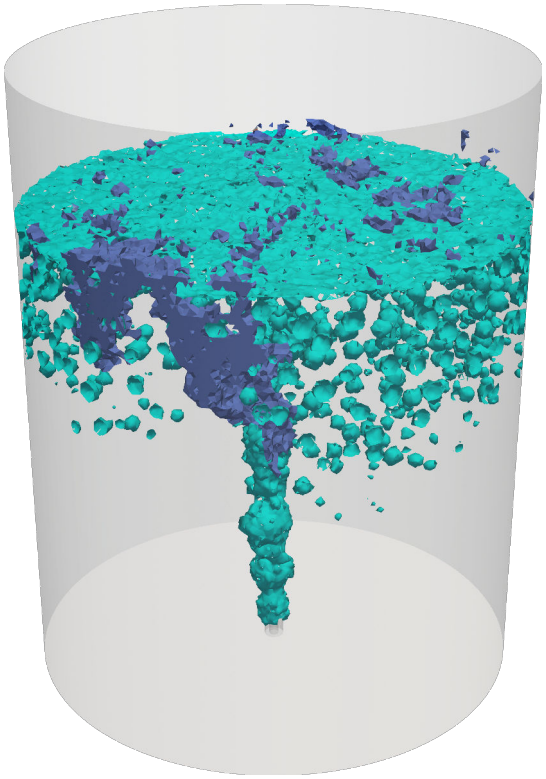

FIGURE 5.3: What the photobioreactor look like 0.1 s after tracer injection. Green: bubble interface, blue: tracer.

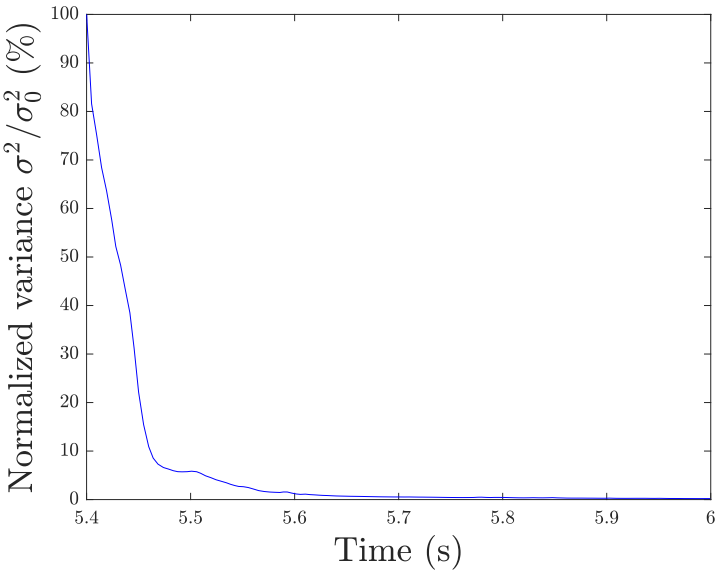

FIGURE 5.4: The evolution of normalized variance. The start time is the moment that tracer is injected, and the liquid already reaches quasi-steady state at that moment.

5.3 Lagrangian transport and PIV

Besides scalar transport, another essential element to establish the complete model is Lagrangian transport, namely the movement of Lagrangian tracers, such as microalgal cells, in the liquid phase. To simulate this gas-liquid-solid flow, the usual way is to couple Lagrangian method with VOF method [180] [181]. Regarding experiments, PIV is an appropriate method to study the Lagrangian transport, since tracer particles for PIV would behave just like the microalgal cells.

5.3.1 Working principle of PIV

PIV is a laser optical technique which enables non-intrusive and instantaneous measurement of velocity field in fluids [182]. A standard PIV measures two velocity components in a plane, while a stereo or tomographic PIV allows to measure all the three velocity components. The working principle of PIV is quite straightforward. First of all, the flow is seeded with light-scattering particles, which are illuminated by a light sheet. Subsequently, a camera records the scattered light by the particles at a regular time interval Δt. Finally, the displacement Δr of a group of particles is obtained by analyzing the cross-correlation of two successive images. Therefore, the velocity is calculated as

$$v = \frac{\Delta r}{\Delta t}. \tag{5.5}$$

In addition, the optical axis of the camera is generally orthogonal to the light sheet in order to record the illuminated plane, as shown in Fig. 5.5.

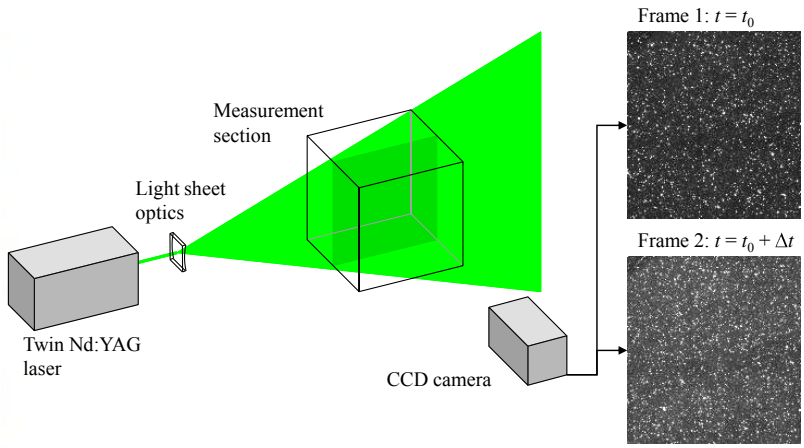

FIGURE 5.5: Schematic sketch of a PIV system, illustration from [183].

5.3.2 PIV setup

A typical PIV experiment consists of several components [184]:

- Hardware:
  - tracer particles: should be easily visible and follow the flow perfectly, moderate number density.
  - pulsed laser: the time interval between two pulses should not be longer than the one between two consecutive images.
  - light sheet optics: to produce a light sheet from a collimated light ray.
  - high speed camera: better to have a high frame rate to ensure that the same particles appear in two consecutive images.
- Software:
  - calibration: to convert distance in pixels into real distance.
  - evaluation: to find the most probable displacement of a group of particles.
  - post-processing: to remove the spurious measurements.

5.3.3 Cross-correlation of images

PIV does not track every single tracer particle, rather, it tracks several particles in a small region known as the interrogation area (IA). The displacement of these particles is obtained by calculating the cross-correlation function of two consecutive IAs. The cross-correlation of two consecutive IAs with resolution $w \times h$ is defined as

$$\Phi_{\mathfrak{k}}(l,m) = \sum_{j=1}^{h}\sum_{i=1}^{w} \mathcal{I}_{\mathfrak{k}+1}(i,j) \cdot \mathcal{I}_{\mathfrak{k}}(i+l, j+m), \tag{5.6}$$

where $\mathcal{I}$ is the data matrix of the IA, $\mathfrak{k}$ indicates the $\mathfrak{k}$-th frame. By trying different (l,m) to maximize $\Phi_{\mathfrak{k}}$, we are actually exploring how far $\mathcal{I}_{\mathfrak{k}}$ has to be moved relative to $\mathcal{I}_{\mathfrak{k}+1}$ in order that the white dots (tracer particles) in the two IAs overlap as best as possible [185]. Therefore, (l,m) that maximizes $\Phi_{\mathfrak{k}}$ is also the most probable displacement in pixels of the particles. The real displacement is subsequently obtained

by applying the calibration factor. Cross-correlation is a statistical concept, thus PIV is essentially a statistical technique, which actually makes the PIV measurement more robust than other particle-tracking techniques.

5.3.4 Potential application in the follow-up study

PIV technique has been widely applied to multiphase systems, as summarized in [186]. For a bubbly flow, PIV was often used together with shadowgraphy in order to record simultaneously liquid velocity field and bubble behaviors [60] [187] [188] [189]. For example, bubble size distributions, gas-liquid interfacial areas, gas holdups and flow velocities were measured simultaneously in [190]. Besides, PIV was sometimes used along with a LIF (Laser-Induced Fluorescence) technique to better distinguish the two phases [191] [192]. Thanks to PIV, the investigation in the interaction between bubbles and liquid phase becomes possible. For example, the influence of a single rising bubble on the velocity field of surrounding liquid was discussed in [193]. And bubble-induced turbulence in liquid phase were investigated for a cylindrical tank [194] [195] and a rectangular one [196].

In this PhD project, bubble behaviors were thoroughly investigated by both experiments and simulations. With this knowledge of bubble behaviors, plus PIV technique, we can investigate how the bubble behaviors influence the liquid velocity field, and thereby also the Lagrangian transport of microalgal cells in the follow-up study. Moreover, we may be also able to choose an appropriate turbulence model for the future numerical investigation in hydrodynamics according to the velocity field measured by PIV.

5.4 Light model

Light intensity distribution has important impact on the efficiency of a photobioreactor, thus radiative transfer in the culture medium should also be studied in the future. For time-independent monochromatic radiation in a radiatively participating medium, the radiative transfer equation (RTE) is [197]

$$\frac{dI(\vec{r},\hat{s})}{ds} = \underbrace{j_e}_{\text{emission}} - \underbrace{\kappa_a I(\vec{r},\hat{s})}_{\text{absorption}} - \underbrace{\sigma_s I(\vec{r},\hat{s})}_{\text{out-scattering}} + \underbrace{\frac{\sigma_s}{4\pi}\int_0^{4\pi} I(\vec{r},\hat{s}')\Psi(\hat{s},\hat{s}')d\Omega'}_{\text{in-scattering}}, \tag{5.7}$$

where $I(\vec{r},\hat{s})$ is the specific intensity at position $\vec{r}$ and in the direction $\hat{s}$, j_e is the emission coefficient, κ_a is the (linear) absorption coefficient, σ_s is the scattering coefficient, $I(\vec{r},\hat{s}')$ is the specific intensity of ambient radiation, $\Psi(\hat{s},\hat{s}')$ is the scattering phase function that describes the probability of scattering from direction $\hat{s}'$ into direction $\hat{s}$, $\hat{s}'$ and Ω' are dummy integration variables. In addition, the two negative terms in (5.7) are often combined, and consequently derive the so-called extinction coefficient

$$\beta_e = \kappa_a + \sigma_s. \tag{5.8}$$

Equation (5.7) is an integro-differential equation, for which an exact solution is usually impossible in three-dimensional cases. Therefore, several methods have been developed to approximately solve the RTE, such as discrete ordinates method (DOM) [198] and Monte Carlo method (MCM) [199], which are often applied to simulate radiative transfer in a photobioreactor. For example, DOM has been applied to study the light intensity distribution inside an open pond in [200] and the advances of MCM

in solar applications which is the leading community for this kind of developpement have been summarized in [201].

The main idea of DOM is to divide the continuous direction $\hat{s}'$ in range of $[0, 4\pi]$ into a set of discrete directions $\hat{s}_i$ [197]. Consequently, the integral term in (5.7), which is the prime factor that renders (5.7) unsolvable, is approximated by

$$\int_0^{4\pi} I(\vec{r}, \hat{s}')\Psi(\hat{s}, \hat{s}')d\Omega' \approx \sum_{i=1}^{n} q_i I(\vec{r}, \hat{s}_i)\Psi(\hat{s}, \hat{s}_i), \tag{5.9}$$

where q_i is the quadrature weight associated with the direction $\hat{s}_i$. This method yields a field of illumination throughout the scene. Hence, from a Lagrangian model perspective, lighting can be treated as any other field (concentration, temperature, ...) that provides a continuous model. Given the fact that DOM approach is very computation-intensive, it is relevant to use it when knowing the whole field is important. Furthermore, in cases where radiation is not strongly coupled with fluid flows, it is a common practice to compute the radiative fields less often than the fluid ones.

Compared to DOM, MCM is more like a "brute force" technique: it does not mathematically solve the RTE (5.7), rather, it mimics the process of emission, absorption and scattering by tracing numerous individual photons or photon packets from emergence to extinction. In MCM, optical path length, scattering angle, the new direction after scattering etc. are all generated by random number [202]:

$$\tau = -\frac{1}{\kappa_a}\ln(\mathcal{R}_\tau), \tag{5.10}$$

$$\theta = 2\pi\mathcal{R}_\theta, \tag{5.11}$$

$$\phi = \cos^{-1}(1 - 2\mathcal{R}_\phi), \tag{5.12}$$

where $\mathcal{R}$ are random numbers in $[0, 1]$, τ is the optical path length, θ, ϕ is the azimuthal, polar scattering angle, respectively. Therefore, MCM can simulate radiative transfer for any geometry, incident light, scattering phase function, etc., as long as the amount of random number, i.e. traced photons, is large enough. Nonetheless, MCM still requires the essential parameters, viz. the absorption coefficient, the scattering coefficient and the scattering phase function to determine whether a photon is absorbed, scattered or survives. MCM methods yield a "probe value", meaning that illumination is known at a point, or as an average over a surface or volume. In the case of a Lagrangian model coupling, it means that a MCM computation has to be made for every tracer. Even though MCM methods are relatively fast compared to DOM ones, their use is relevant when few tracers are used.

5.5 Conclusions

In this chapter, we first investigated the hydrodynamics of a cylindrical photobioreactor by the numerical tool proposed in the previous chapter. We found that the volume-averaged momentum of the two-phase flow tended to be constant after a certain time, which is a well-known fact among the biologists. The numerical tool was also capable of representing the scalar transport including mixing. Afterwards, we introduced the other essential components to achieve a full description of a photobioreactor, such as PIV and light modeling. By assembling all these elements appropriately, the complete model for a photobioreactor should be feasible in the future.

Chapter 6

General conclusions

Bubbles provide both kinetic energy and carbon source for microalgal cultivation in a photobioreactor. Therefore, bubble behaviors greatly affect mixing, mass transfer, and cell distribution in a reactor. In consideration of their importance, this thesis investigated bubble behaviors under different flow conditions by both experimental and numerical methods.

In the experimental part, we first developed a brand new photobioreactor for this PhD thesis and latter studies. With this device, both shadowgraphy and PIV can be carried out. Specially for this thesis, a shadowgraphy equipment was set up around the reactor in order to take high-quality images of bubbles. Subsequently, bubble behaviors were obtained by processing and analyzing the raw images. From the experimental results, we found that both bubbling frequency and average bubble volume increased with gas flow rate at steady state. In addition, bubble population became more disperse in terms of bubble volume when increasing gas flow rate. Besides, bubble shape is also highly sensitive to gas flow rate: bubbles at low flow rate were relatively rounded, on the contrary, elongated bubbles frequently appeared at high flow rate. The distance between two adjacent bubbles was shorter at high flow rate, which sometimes gave rise to even longer bubble due to bubble coalescence.

In the numerical part, we proposed VOF method and OpenFOAM as the numerical tools to simulate bubbles. 2D cases were set up to test the tools and 3D cases were prepared for formal simulations. Subsequently, those cases were performed on supercomputer Mésocentre. And the bubble behaviors were acquired from the post-processing of the simulations. First of all, 2D simulations demonstrated that Courant number had no significant impact on the numerical results, while mesh size played a decisive role in the numerical results: it should be less than the nozzle size, otherwise the results were physically meaningless. Subsequently, 3D simulations were validated with experiments: bubble volume and bubble shape evolution from simulations were in accordance with those from experiments. However, limited by the computing power, the polydispersity of bubble population were not able to be represented by the numerical tools.

With the methods proposed in this thesis, bubble behaviors in a photobioreactor were quantitatively studied, which consequently makes it possible to investigate how bubble behaviors determine mass transfer, cell distribution, etc. Subsequently, a better understanding of bubble behaviors and their effect on other phenomena would allow us to find an optimal condition for microalgal cultivation in a photobioreactor. Moreover, the validated simulation tool may speed up the design of a photobioreactor since sophisticated experiments are no more needed. Besides, the present work could also help to study other types of reactors, such as chemical reactor, as long as bubbly flow exists in such equipment.

This thesis placed great importance on the gas phase of the two-phase flow, thus further research is needed to investigate the liquid phase, i.e. the hydrodynamics in

a photobioreactor. Another step is to calculate the irradiance in different zone of the reactor. Finally, a physical-biological coupling model would also be required to describe cell growth in a moving liquid.

Appendix A

Representative studies on gas-liquid flow in a reactor

Table A.1 summarizes different methods applied to study gas-liquid flow in a bubble column, it extends the table **??**.

TABLE A.1: A summary of representative literature aiming to investigate gas-liquid flow in a bubble column.

Ref.	Objective	Numerical	Experimental	Main conclusions	Strength & Limitation
[46] (1994)	To study the gas-liquid flow in a rectangular bubble column by both simulation and experiments. Experimental study for the influence of the type and location of the gas sparger on the hydrodynamics.	2D,Eulerian-Eulerian,laminar	Rectangular bubble column: 500×2000×80 mm. Liquid velocity: LDA with a small gas hold-up. Bubble velocity: Double-channel fibre, optical probe. Gas hold-up: electro-conductivity probe. Bubble size: Photo-electrical suction probe.	The calculated liquid velocity field (vortices) agreed with the measured one qualitatively for non-coalescing bubbly flow regime	Strength: velocity field was investigated by both experiments and simulation. Limitation: the bubbles were not captured.
[47] (1999)	To obtain the knowledge of the hydrodynamics in chemical reactors and finally to improve the efficiency of the reactor.	2D vs 3D, Eulerian-Eulerian, laminar vs $k-\epsilon$ turbulence model, software: CFX4.2	Rectangular bubble column: 200×450 (water height)×50 mm. Different sparger situations: 1.one left, 2.one center, 3.three uniformly distributed. Liquid velocity: LDA and PIV.	2D simulations were not able to show the periodic bubble hose movement observed in reality due to an overprediction of the turbulent energy in the fluid. Laminar simulations did not reproduce the behavior of the test case, a turbulence model had to be considered. The turbulence dampened the dynamic of the bubble. 3D simulation with a sufficient fine resolution is necessary for accurate results.	Strength: 2D and 3D were compared, with and without turbulence model were compared. Limitation: the bubbles were not captured.
[49] (2001)	To apply large eddy simulation to the modeling of gas-liquid flow. To compare $k-\epsilon$ and large eddy turbulence model.	3D, Eulerian-Eulerian, $k-\epsilon$ vs large eddy turbulence model, software: CFX4.3.	Rectangular bubble column: 0.15×1×0.15 m. Water height: 0.45 m. Liquid velocity: PIV.	LES simulation captured the strong transient movement of the bubble plume, which were observed in the experiment. Both the velocity and velocity fluctuations were in quantitative agreement with the measurement data.	Strength: Another turbulence model (LES) was used in this study. Limitation: absence of bubbles in simulations.

Ref.	Objective	Numerical	Experimental	Main conclusions	Strength & Limitation
[50] (2002)	To understand better the mixing in bubble column reactor, we have to know better the dynamic characteristics. The effect of gas flow rate and sparger configuration on dynamics of gas-liquid flow were studied numerically and experimentally.	3D,Eulerian-Eulerian, single/multi-group models, software: FLUENT4.5.	Rectangular bubble column: 0.2×1.2×0.05 m. Water height: 0.45 m. 1-butanol was added in water as a coalescence inhibitor. Measurements of wall pressure fluctuations by pressure transducers, high speed camera to measure bubble size.	The plume oscillation periods measured by wall pressure fluctuation were in good agreement with LDA measurements from literature. Bubble plume comprising of smaller bubbles led to faster oscillations than those comprising of larger bubbles. Coalescence is more pre-dominant than breakage because of lower turbulence. Lower axial upward averaged velocity resulted in longer residence time, lower bubble concentration.	Strength: flow pattern and plume oscillation periods were well investigated. Limitation: no explicit bubbles.
[51] (2005)	To model variations in the bubble size distribution due to bubble coalescence and breakup	2D, Eulerian-Eulerian coupled with Population Balance Model, solving the equations by Classes Method and (Direct) Quadrature Method of Moments, mixture $k-\epsilon$ turbulence model, software: FLUENT 6.0.	None	Even at low gas flow velocity, bubble size distribution changes. At least 12-18 classes are required to accurately model the entire range of bubble diameters in a typical bubble column. QMOM requires lower CPU time than CM.	Strength: bubble size distribution were studied with relatively less computing time. Limitation: no their own experiments.
[48] (2007)	To investigate bubble column reactor at high superficial velocity ($U_G \leq 0.4$).	3D,Eulerian-Eulerian, standard $k-\epsilon$ vs RNG $k-\epsilon$ turbulence model, software: FLUENT6.2.	Acrylic cylindrical bubble column: $d = 0.2$ m, $h = 2$ m. Water height: 1 m. Bubble size and bubble velocity: electrical resistivity probe (conductivity probe). Measurement of mixing time: to measure the conductivity of NaCl solution by a standard conductivity electrode along with a digital conductivity meter.	The conductivity probes were used to measure local time-averaged gas hold-up, bubble size distribution, bubble velocity distribution, and interfacial area distribution within the column. The CFD model showed good agreement with experimental data for time-averaged flow properties.	Strength: both experiments and simulations for gas hold-up, bubble velocity and bubble size. Limitation: only simulations for velocity field, no PIV measurements.
[58] (2007)	To study the influence of superficial gas velocity and distributors on gas hold-up and interfacial area. the authors have used VOF method, which was used for single bubble before, in this paper the VOF is used for a continuous bubble chain.	2D vs 3D, VOF, $k-\epsilon$ turbulence model, software: FLUENT6.1	Cylindrical bubble column: $d = 10$ cm, $h = 100$ cm. Bubble rise velocity, volume averaged gas hold-up: four point optical probe.	Lower superficial gas velocity resulted in smaller bubbles and lower bubble rise velocity. Leading bubble was bigger than trailing bubble which might be due to less effects of wall and other surface forces on the trailing bubble. Bubble rise velocities in 2D were $\sim$ 30% lower than those in 3D, maybe because the 3D wake cannot be accurately modeled with 2D. 3D bubble rise velocity had a good agreement with Deckwer equation [73]. Same superficial gas velocity, smaller size distributor resulted in smaller bubbles and lower bubble rise velocity. Gas hold-up from 3D VOF simulation had good agreement with experiments.	Strength: VOF method is used for studying a bubble swarm. Limitation: more bubble behaviors should be detailed.
[52] (2008)	To predict bubble size distribution, volume fraction and velocity field taking account of bubble breakup and coalescence.	3D, Eulerian-Eulerian coupled with Population Balance Model, solved by Classes Method, dispersed $k-\epsilon$ turbulence model, software: OpenFOAM.	None	Good agreement between simulations and experiments. Eleven classes is a good compromise between reasonable computational effort and precision.	Strength: E-E and PBM are coupled in OpenFOAM, an open source software. Limitation: no experimental validation.

Ref.	Objective	Numerical	Experimental	Main conclusions	Strength & Limitation
[59] (2011)	To simulate turbulent bubbly flow in complex systems by Eulerian-Lagrangian approach.	3D Eulerian-Lagrangian, LES turbulence model, bubble growth/collapse was modeled by the Rayleigh–Plesset equation, cylindrical and rectangular reactor	None	The approach is suitable for simulation of subgrid bubble dynamics in complex flows without cavitation as well as small-scale bubbly cavitating flows. The approach is suitable for simulation of up to million bubbles in a turbulent flow.	Strength: a through numerical study of bubbly flow by Eulerian-Lagrangian model with bubble coalescence kernel. Limitation: there is no their own experimental validation.
[54] (2014)	To develop a CFD nodel coupled with a population balance model for the biological phase for lab-scale and industrial scale bioreactors.	3D Eulerian-Eulerian, coupled with population balance model, $k-\epsilon$ and LES turbulence model, cylindrical reactor (70 L and 70 m^3).	None	Cell growth was essentially sensitive to the volume average concentrations, whereas substrate assimilation was more sensitive to the spatial distribution of the substrates. The biological rates are not algebraically linked to the local concentrations.	Strength: the heterogeneity of cells in liquid phase was taken into account. Limitation: omitting the influence of bubble behaviors on the heterogeneity of cells.
[45] (2015)	To study the liquid phase velocity in homogeneous regime at low gas flow rates.	3D, Eulerian-Lagrangian, $k-\epsilon$ turbulence model, an average about 100 to 150 bubbles are present in the domain for the range of superficial gas velocities considered.	Rectangular bubble column: 267×600×15 mm, made of Plexiglas. Water height: 500 mm. Liquid velocity: PIV.	This article has mainly compared the measured and the simulated vertical and horizontal time-averaged liquid velocity profiles. At low gas flow rate (0.1 L/min), it had a reasonable agreement, but at relatively high gas flow rate (0.2 L/min), the discrepancy was larger.	Strength: velocity field was investigated by both PIV and 3D turbulent E-L simulation. Limitation: low gas flow rate, bubble coalescence or breakup was not taken into account.
[53] (2016)	To investigate mixing in a stirred bioreactor taking into account of bubble coalescence and breakup	3D, Eulerian-Eulerian coupled with Population Balance Model, $k-\epsilon$ turbulence model, software: FLUENT 14.	None	Near the impeller region, bubble size was smaller, and hence mass transfer was more effective. An optimum impeller was obtained to achieve maximum mixing without creating excessive cell damage.	Strength: mixing in a bioreactor was studied by a economic and effective way. Limitation: no their own experiments.
[55] (2018)	To develop a CFD model for simulating cell cultivation in an industrial-scale reactor.	3D Eulerian-Eulerian, taking into account mass transfer and bacterial activity, realizable $k-\epsilon$ turbulence model, software: ANSYS	OKTOP®9000 cylindrical reactor, volume: around 1000 m^3.	Concentration of species in simulations were in agreement with the one measured in a similar scale reactor. The CFD modeling was proved to be a reliable tool for design of industrial aerobic fermenters.	Strength: it studied most phenomena in a bioreactor, like mass transfer, fermentation kinetics, turbulence, etc. Limitation: hydrodynamics was not validated by experiments.
[56] (2018)	To investigate hydrodynamics, oxygen transfer and oxygen uptake in bubble-column and airlift bioreactors by simulations	3D Eulerian-Eulerian, cylindrical reactor, mass transfer and oxygen consumption were also added in the model, software: OpenFOAM	None	The simulation result for gas holdup and gas-liquid mass transfer were in good agreement with experiments and engineering correlations from the bubble-column literature.	Strength: a thorough numerical study of bioreactor. Limitation: no their own experimental validation.

Ref.	Objective	Numerical	Experimental	Main conclusions	Strength & Limitation
[57] (2018)	To investigate the influence of the impeller speed in revolutions and crossover frequency between the light and the dark zones on the growth of microalgae in a stirred tank photobioreactor by CFD.	3D Eulerian, cylindrical reactor, $k-\epsilon$ turbulence model, taking into account radiative transfer, software: ANSYS-Fluent.	None	The cell particles followed the fluid trajectory. The crossover frequency between the dark and light zones is critical for cell growth.	Strength: radiative transfer was coupled with CFD. Limitation: no enough experimental validation.
[203] (2018)	To investigate the details of the cells' movements and multiphase flow hydrodynamics during microalgae culturing in a cylindrical split airlift photobioreactor by an advanced radioactive particle tracking technique	None	Plexiglas cylindrical airlift photobioreactor (split column), $d = 12.7$ cm, $h = 150$ cm, radioactive particle tracking applied to measure the flow field.	The results obtained help for advancing the fundamentals knowledge required for split internal-loop photobioreactor analysis to improve microalgae growth system.	Strength: liquid velocity field and cell trajectory were studied by non-intrusive technique. Limitation: gas phase was not well studied.

Appendix B

Matlab code for image processing and analysis

The following code can be directly applied to treat gray scale images from experiments. As for colorful images from simulations, we just need to convert the RGB images into gray scale images before running the code.

```
close all
clear all

Calibration=3/80;  % mm/pixels
timeCali=1/200; % second/frame

cd D:\DirectoryWithImages;
ImSeq=struct2cell(dir('*.tif'));
[k,n]=size(ImSeq);

boundarySeq=cell(1,n);
probe=zeros(1,n);
peri=zeros(1,n);
area=zeros(1,n);
bound=zeros(n,4);

% probe point
px=200;
py=500;

%% image processing
for i=1:n
    single=ImSeq{1,i};
    seq=imread(single);
    crop=imcrop(seq,[1 1 400 700]); % cut nozzle
    thresh=imbinarize(crop);
    % obtain the threshold for small objects
    CCthres = bwconncomp(thresh);
    ca = regionprops(CCthres,'Centroid','Area');
    areaThres = cat(1,ca.Area);
    [row,~]=size(areaThres);
    % delete small objects
    if row>1
        sortA=sort(areaThres);
        SmallThresh=sortA(end-1)+1;
        fill=bwareaopen(thresh,SmallThresh);
    else
        fill=thresh;
```

```
    end
    invert=imcomplement(fill);
    probe(i)=invert(py,px);
    invert=im2double(invert);
    % for bubble volume
    [B,~] = bwboundaries(invert,'noholes');
    boundarySeq{1,i}=B;
    % for bubble shape factors
    CCinvert = bwconncomp(invert);
    cp = regionprops(CCinvert,'Area','Perimeter','BoundingBox');
    pe = cat(1,cp.Perimeter);
    ar = cat(1,cp.Area);
    bbox = cat(1,cp.BoundingBox);
    idx = find( (bbox(:,2)<=py) & (bbox(:,4)+bbox(:,2)-1>=py) & ...
                (bbox(:,1)<=px) & (bbox(:,3)+bbox(:,1)-1>=px) );

    if ~isempty(idx) & ( size(idx,1) == 1 )
        peri(i)=pe(idx);
        area(i)=ar(idx);
        bound(i,:)=bbox(idx,:);
    end
    cir=4*pi*area./(peri.^2); % circularity
end
ratio=bound(:,4)./bound(:,3); % aspect ratio

% plot probe pulses
figure(1)
plot(1:n,probe)
ylim([0 1.5])
xlabel('Image sequence','FontSize',18,'Interpreter','latex')
ylabel('Value at a probe point','FontSize',18,'Interpreter','latex')

%% pick begining and ending frame of the same bubble
f=[];
for j=2:(n-1)
    if probe(j)==1 & ...
       ((probe(j-1)==0 & probe(j+1)==1) | (probe(j-1)==1 & probe(j+1)==0))
        f=[f;j];
    end

end

% pick bubble group with complete begining and end frames
% to make sure the size of fbu is an even number
if probe(f(1)-1)==1 & probe(f(1)+1)==0
    f=f(2:end);
end
if probe(f(end)-1)==0 & probe(f(1)+1)==1
    f=f(1:(end-1));
end

%% bubble number
hf=f(1:2:end);
[sf,~]=size(hf);
bNum=1:sf;
figure(2)
plot(hf*timeCali,bNum,'k-')
```

```
xlabel('Time (s)','Interpreter','latex','FontSize',18)
ylabel('Cumulative bubble number','Interpreter','latex','FontSize',18)

%% derivative of bubble number
nc=30;
bDiff=zeros(sf,1);
for i=(nc+1):(sf-nc)
    der=fit( hf( (i-nc):(i+nc) ),bNum( (i-nc):(i+nc) )','poly2');
    coefs=coeffvalues(der);
    bDiff(i)=2*coefs(1)*hf(i)+coefs(2);
end
figure(3)
plot(hf((nc+1):(sf-nc))*timeCali,bDiff((nc+1):(sf-nc)),'k-')
xlabel('Time (s)','Interpreter','latex','FontSize',18)
ylabel('Bubbling frequency (Hz)','Interpreter','latex','FontSize',18)

%% bubble volume
meanv=zeros(sf,1);
for ib=1:sf
    vol=[]; % a bubble volume during rising
    for q=f(ib):f(ib+1)
        bounCell=boundarySeq{1,q}; %all the boundaries inside one frame
        [m,~]=size(bounCell);
        for h=1:m
            bj=bounCell{h};
            yj=bj(:,1);
            xj=bj(:,2);
            if (min(yj)<=py)&&(py<=max(yj)&&min(xj)<=px)&&(px<=max(xj))
                % pick out the boundary including probe point
                boundary=bounCell{h};
            end
        end
        yp=boundary(:,1);
        xp=boundary(:,2);
        Ymax=max(yp);
        Ymin=min(yp);
        d=Ymax-Ymin+1;
        r=zeros(d,1);
        for j=Ymin:Ymax
            % pick out two end points at the same height level
            logi=(yp==j);
            xpi=xp(logi);
            xpisort=sort(xpi);
            r(j-Ymin+1)=(xpisort(end)-xpisort(1))/2;
        end
        vol=[vol;sum(pi*r.^2)*Calibration^3]; % volume
    end
    meanv(ib)=mean(vol);
end

% flow rate, the last bubble is discarded to have correct time interval
totv=sum(meanv(1:(end-1)))*1e-3; % unit: mL
time=(f(end-1)-f(1))*timeCali/60; % unit: minute
Q=[num2str(totv/time),' mL/min'] % flow rate, unit: mL/min

% plot mean bubble volume
bf=-hf(1); % frame number not included
```

```
153 figure(4)
154 plot((hf+bf)*timeCali,meanv,'b.')
155 xlabel('Time (s)','FontSize',18','Interpreter','latex')
156 ylabel('Mean bubble volume (mm$^3$)','FontSize',18','Interpreter','latex')
157
158 % plot bubble shape factors
159 hz=10; % plot every 'hz' bubbles
160 for ic=1:hz:sf
161     figure(5)
162     hd=plot( ((f(ic):f(ic+1))+bf)*timeCali,ratio(f(ic):f(ic+1)),'bs-',...
163     ((f(ic):f(ic+1))+bf)*timeCali,cir(f(ic):f(ic+1)),'ro-.');
164     hold on
165     set(hd, {'MarkerFaceColor'}, {'b';'r'});
166     legend({'Aspect ratio ($h/w$)','Circularity'},'Interpreter','latex',...
167     'FontSize',13,'Location','southwest');
168     xlabel('Time (s)','FontSize',18','Interpreter','latex')
169 end
```

Bibliography

[1] British Petroleum. *BP statistical review of world energy*. London: British Petroleum, 2017.

[2] Shahriar Shafiee and Erkan Topal. "When will fossil fuel reserves be diminished?" In: *Energy policy* 37.1 (2009), pp. 181–189.

[3] Nasir Khalid. "Efficient Energy Management: Is Variable Frequency Drives the Solution". In: *Procedia-Social and Behavioral Sciences* 145 (2014), pp. 371–376.

[4] Jong-Chao Yeh and Chih-Hsiang Liao. "Impact of population and economic growth on carbon emissions in Taiwan using an analytic tool STIRPAT". In: *Sustainable Environment Research* 27.1 (2017), pp. 41–48.

[5] Bert Metz, Ogunlade Davidson, Heleen De Coninck, Manuela Loos, and Leo Meyer. *IPCC special report on carbon dioxide capture and storage*. Tech. rep. Intergovernmental Panel on Climate Change, Geneva (Switzerland). Working Group III, 2005.

[6] Amit Kumar, Sarina Ergas, Xin Yuan, Ashish Sahu, Qiong Zhang, Jo Dewulf, F Xavier Malcata, and Herman Van Langenhove. "Enhanced CO 2 fixation and biofuel production via microalgae: recent developments and future directions". In: *Trends in biotechnology* 28.7 (2010), pp. 371–380.

[7] Richard Sayre. "Microalgae: the potential for carbon capture". In: *Bioscience* 60.9 (2010), pp. 722–727.

[8] Philip T Pienkos and AL Darzins. "The promise and challenges of microalgal-derived biofuels". In: *Biofuels, Bioproducts and Biorefining* 3.4 (2009), pp. 431–440.

[9] Pauline Spolaore, Claire Joannis-Cassan, Elie Duran, and Arsène Isambert. "Commercial applications of microalgae". In: *Journal of bioscience and bioengineering* 101.2 (2006), pp. 87–96.

[10] Razif Harun, Manjinder Singh, Gareth M Forde, and Michael K Danquah. "Bioprocess engineering of microalgae to produce a variety of consumer products". In: *Renewable and Sustainable Energy Reviews* 14.3 (2010), pp. 1037–1047.

[11] CU Ugwu, H Aoyagi, and H Uchiyama. "Photobioreactors for mass cultivation of algae". In: *Bioresource technology* 99.10 (2008), pp. 4021–4028.

[12] Niels T Eriksen, Bjarne R Poulsen, and JJ Lønsmann Iversen. "Dual sparging laboratory-scale photobioreactor for continuous production of microalgae". In: *Journal of Applied Phycology* 10.4 (1998), pp. 377–382.

[13] Bei Wang, Christopher Q Lan, and Mark Horsman. "Closed photobioreactors for production of microalgal biomasses". In: *Biotechnology advances* 30.4 (2012), pp. 904–912.

[14] Roselei Claudete Fontana, Tomás Augusto Polidoro, and Mauricio Moura da Silveira. "Comparison of stirred tank and airlift bioreactors in the production of polygalacturonases by Aspergillus oryzae". In: *Bioresource technology* 100.19 (2009), pp. 4493–4498.

[15] Bo Kong. "Experimental and computational study of turbulent mixing in a confined rectangular jet". PhD thesis. Iowa State University, 2011.

[16] Guan Wang, Wenjun Tang, Jianye Xia, Ju Chu, Henk Noorman, and Walter M Gulik. "Integration of microbial kinetics and fluid dynamics toward model-driven scale-up of industrial bioprocesses". In: *Engineering in life sciences* 15.1 (2015), pp. 20–29.

[17] Chun-Yen Chen, Kuei-Ling Yeh, Rifka Aisyah, Duu-Jong Lee, and Jo-Shu Chang. "Cultivation, photobioreactor design and harvesting of microalgae for biodiesel production: a critical review". In: *Bioresource technology* 102.1 (2011), pp. 71–81.

[18] Iris Perner-Nochta and Clemens Posten. "Simulations of light intensity variation in photobioreactors". In: *Journal of Biotechnology* 131.3 (2007), pp. 276–285.

[19] Xinyu Zhang and Goodarz Ahmadi. "Eulerian–Lagrangian simulations of liquid–gas–solid flows in three-phase slurry reactors". In: *Chemical Engineering Science* 60.18 (2005), pp. 5089–5104.

[20] Thierry Lebeau and Jean-Michel Robert. "Diatom cultivation and biotechnologically relevant products. Part I: Cultivation at various scales". In: *Applied Microbiology and Biotechnology* 60.6 (2003), pp. 612–623.

[21] Kiyomi Akita and Fumitake Yoshida. "Bubble size, interfacial area, and liquid-phase mass transfer coefficient in bubble columns". In: *Industrial & Engineering Chemistry Process Design and Development* 13.1 (1974), pp. 84–91.

[22] Amol A Kulkarni. "Mass transfer in bubble column reactors: effect of bubble size distribution". In: *Industrial & Engineering Chemistry Research* 46.7 (2007), pp. 2205–2211.

[23] Bei Wang, Yanqun Li, Nan Wu, and Christopher Q Lan. "CO2 bio-mitigation using microalgae". In: *Applied microbiology and biotechnology* 79.5 (2008), pp. 707–718.

[24] Ismail Rawat, R Ranjith Kumar, Taurai Mutanda, and Faizal Bux. "Biodiesel from microalgae: a critical evaluation from laboratory to large scale production". In: *Applied energy* 103 (2013), pp. 444–467.

[25] Teresa M Mata, Antonio A Martins, and Nidia S Caetano. "Microalgae for biodiesel production and other applications: a review". In: *Renewable and sustainable energy reviews* 14.1 (2010), pp. 217–232.

[26] Amanda Khuu. "Innovation Policies in Alberta's Oil Sands". PhD thesis. Faculty of Graduate Studies, 2014.

[27] Zhijie Chen, Xinru Zhang, Zeyi Jiang, Xuehui Chen, Hongzhou He, and Xinxin Zhang. "Light/dark cycle of microalgae cells in raceway ponds: Effects of paddlewheel rotational speeds and baffles Installation". In: *Bioresource technology* 219 (2016), pp. 387–391.

[28] Alessandro Concas, Giovanni Antonio Lutzu, Massimo Pisu, and Giacomo Cao. "Experimental analysis and novel modeling of semi-batch photobioreactors operated with Chlorella vulgaris and fed with 100%(v/v) CO2". In: *Chemical engineering journal* 213 (2012), pp. 203–213.

[29] Bikram K Nayak, Shantonu Roy, and Debabrata Das. "Biohydrogen production from algal biomass (Anabaena sp. PCC 7120) cultivated in airlift photobioreactor". In: *international journal of hydrogen energy* 39.14 (2014), pp. 7553–7560.

[30] Mohammad Arjomandzadegan, Poorya Rafiee, Mostafa Keshavarz Moraveji, and Maryam Tayeboon. "Efficacy evaluation and kinetic study of biosorption of nickel and zinc by bacteria isolated from stressed conditions in a bubble column". In: *Asian Pacific journal of tropical medicine* 7 (2014), S194–S198.

[31] Ana P Carvalho, Luís A Meireles, and F Xavier Malcata. "Microalgal reactors: a review of enclosed system designs and performances". In: *Biotechnology progress* 22.6 (2006), pp. 1490–1506.

[32] Otto Pulz. "Photobioreactors: production systems for phototrophic microorganisms". In: *Applied microbiology and biotechnology* 57.3 (2001), pp. 287–293.

[33] Johan U Grobbelaar. "Factors governing algal growth in photobioreactors: the "open" versus "closed" debate". In: *Journal of applied phycology* 21.5 (2009), p. 489.

[34] Liam Brennan and Philip Owende. "Biofuels from microalgae—a review of technologies for production, processing, and extractions of biofuels and coproducts". In: *Renewable and sustainable energy reviews* 14.2 (2010), pp. 557–577.

[35] Josef Kuneš. *Dimensionless physical quantities in science and engineering*. Elsevier, 2012.

[36] Shih-Hsin Ho, Chun-Yen Chen, Duu-Jong Lee, and Jo-Shu Chang. "Perspectives on microalgal CO2-emission mitigation systems—a review". In: *Biotechnology advances* 29.2 (2011), pp. 189–198.

[37] Prabuddha L Gupta, Seung-Mok Lee, and Hee-Jeong Choi. "A mini review: photobioreactors for large scale algal cultivation". In: *World Journal of Microbiology and Biotechnology* 31.9 (2015), pp. 1409–1417.

[38] Arun K Vuppaladadiyam, Pepijn Prinsen, Abdul Raheem, Rafael Luque, and Ming Zhao. "Microalgae cultivation and metabolites production: a comprehensive review". In: *Biofuels, Bioproducts and Biorefining* 12.2 (2018), pp. 304–324.

[39] Hu-Ping Luo and Muthanna H Al-Dahhan. "Analyzing and modeling of photobioreactors by combining first principles of physiology and hydrodynamics". In: *Biotechnology and Bioengineering* 85.4 (2004), pp. 382–393.

[40] Qingshan Huang, Fuhua Jiang, Lianzhou Wang, and Chao Yang. "Design of photobioreactors for mass cultivation of photosynthetic organisms". In: *Engineering* 3.3 (2017), pp. 318–329.

[41] Michael H Huesemann, J Van Wagenen, T Miller, A Chavis, S Hobbs, and B Crowe. "A screening model to predict microalgae biomass growth in photobioreactors and raceway ponds". In: *Biotechnology and bioengineering* 110.6 (2013), pp. 1583–1594.

[42] Christopher Earls Brennen. *Fundamentals of multiphase flow*. Cambridge university press, 2005.

[43] Yue Hao and Andrea Prosperetti. "A numerical method for three-dimensional gas–liquid flow computations". In: *Journal of Computational Physics* 196.1 (2004), pp. 126–144.

[44] JP Bitog, I-B Lee, C-G Lee, K-S Kim, H-S Hwang, S-W Hong, I-H Seo, K-S Kwon, and E Mostafa. "Application of computational fluid dynamics for modeling and designing photobioreactors for microalgae production: a review". In: *Computers and Electronics in Agriculture* 76.2 (2011), pp. 131–147.

[45] S Besbes, Mahmoud El Hajem, H Ben Aissia, Jean-Yves Champagne, and J Jay. "PIV measurements and Eulerian–Lagrangian simulations of the unsteady gas–liquid flow in a needle sparger rectangular bubble column". In: *Chemical Engineering Science* 126 (2015), pp. 560–572.

[46] Sokolichin Becker, A Sokolichin, and G Eigenberger. "Gas—liquid flow in bubble columns and loop reactors: Part II. Comparison of detailed experiments and flow simulations". In: *Chemical Engineering Science* 49.24 (1994), pp. 5747–5762.

[47] D Pfleger, S Gomes, N Gilbert, and H-G Wagner. "Hydrodynamic simulations of laboratory scale bubble columns fundamental studies of the Eulerian–Eulerian modelling approach". In: *Chemical Engineering Science* 54.21 (1999), pp. 5091–5099.

[48] Mohan R Rampure, Amol A Kulkarni, and Vivek V Ranade. "Hydrodynamics of bubble column reactors at high gas velocity: experiments and computational fluid dynamics (CFD) simulations". In: *Industrial & Engineering Chemistry Research* 46.25 (2007), pp. 8431–8447.

[49] Niels Gerbrand Deen, Tron Solberg, and Bjørn Helge Hjertager. "Large eddy simulation of the gas–liquid flow in a square cross-sectioned bubble column". In: *Chemical Engineering Science* 56.21-22 (2001), pp. 6341–6349.

[50] Vivek V Buwa and Vivek V Ranade. "Dynamics of gas–liquid flow in a rectangular bubble column: experiments and single/multi-group CFD simulations". In: *Chemical Engineering Science* 57.22-23 (2002), pp. 4715–4736.

[51] Jay Sanyal, Daniele L Marchisio, Rodney O Fox, and Kumar Dhanasekharan. "On the comparison between population balance models for CFD simulation of bubble columns". In: *Industrial & Engineering Chemistry Research* 44.14 (2005), pp. 5063–5072.

[52] Rachid Bannari, Fouzi Kerdouss, Brahim Selma, Abdelfettah Bannari, and Pierre Proulx. "Three-dimensional mathematical modeling of dispersed two-phase flow using class method of population balance in bubble columns". In: *Computers & chemical engineering* 32.12 (2008), pp. 3224–3237.

[53] Jayati Sarkar, Lalita Kanwar Shekhawat, Varun Loomba, and Anurag S Rathore. "CFD of mixing of multi-phase flow in a bioreactor using population balance model". In: *Biotechnology progress* 32.3 (2016), pp. 613–628.

[54] Jérôme Morchain, Jean-Christophe Gabelle, and Arnaud Cockx. "A coupled population balance model and CFD approach for the simulation of mixing issues in lab-scale and industrial bioreactors". In: *AIChE Journal* 60.1 (2014), pp. 27–40.

[55] Dmitry Gradov, Mei Han, Petri Tervasmäki, Marko Latva-Kokko, Johanna Vaittinen, Arto Pihlajamäki, and Tuomas Koiranen. "Numerical simulation of biomass growth in OKTOP® 9000 reactor at industrial scale". In: *Industrial & Engineering Chemistry Research* (2018).

[56] Mohammad J Rahimi, Hariswaran Sitaraman, David Humbird, and Jonathan J Stickel. "Computational fluid dynamics study of full-scale aerobic bioreactors: Evaluation of gas-liquid mass transfer, oxygen uptake, and dynamic oxygen distribution". In: *Chemical Engineering Research and Design* (2018).

[57] Raj Kumar Saini, Pramod P Wangikar, and Manaswita Bose. "CFD analysis of the flow dynamics of microorganisms in dilute cultures in stirred tank photobioreactors". In: *Bioresource Technology Reports* (2018).

[58] Abid Akhtar, Vishnu Pareek, and Moses Tadé. "CFD simulations for continuous flow of bubbles through gas-liquid columns: Application of VOF method". In: *Chemical Product and Process Modeling* 2.1 (2007).

[59] Ehsan Shams, J Finn, and SV Apte. "A numerical scheme for Euler–Lagrange simulation of bubbly flows in complex systems". In: *International Journal for Numerical Methods in Fluids* 67.12 (2011), pp. 1865–1898.

[60] R Lindken and W Merzkirch. "A novel PIV technique for measurements in multiphase flows and its application to two-phase bubbly flows". In: *Experiments in fluids* 33.6 (2002), pp. 814–825.

[61] JA Medrano, F Gallucci, F Boccia, N Alfano, and M van Sint Annaland. "Determination of the bubble-to-emulsion phase mass transfer coefficient in gas-solid fluidized beds using a non-invasive infra-red technique". In: *Chemical Engineering Journal* 325 (2017), pp. 404–414.

[62] WAS Kumara, G Elseth, BM Halvorsen, and MC Melaaen. "Comparison of Particle Image Velocimetry and Laser Doppler Anemometry measurement methods applied to the oil–water flow in horizontal pipe". In: *Flow measurement and Instrumentation* 21.2 (2010), pp. 105–117.

[63] Mark P Wernet. "Temporally resolved PIV for space–time correlations in both cold and hot jet flows". In: *Measurement Science and Technology* 18.5 (2007), p. 1387.

[64] FJ Tavera, R Escudero, and JA Finch. "Gas holdup in flotation columns: laboratory measurements". In: *International Journal of Mineral Processing* 61.1 (2001), pp. 23–40.

[65] Hans Dieter Baehr and Karl Stephan. *Heat and mass transfer, 1998.*

[66] Kamiel S Gabriel. *Microgravity Two-phase flow and heat transfer.* Springer, 2007.

[67] Ovid Baker et al. "Design of pipelines for the simultaneous flow of oil and gas". In: *Fall Meeting of the Petroleum Branch of AIME.* Society of Petroleum Engineers. 1953.

[68] Geoffrey Frederick Hewitt and DN Roberts. *Studies of two-phase flow patterns by simultaneous x-ray and flast photography.* Tech. rep. Atomic Energy Research Establishment, Harwell, England (United Kingdom), 1969.

[69] Mishima Kaichiro and Mamoru Ishii. "Flow regime transition criteria for upward two-phase flow in vertical tubes". In: *International Journal of Heat and Mass Transfer* 27.5 (1984), pp. 723–737.

[70] Jian Li, Marisa Stamato, Eirini Velliou, Clayton Jeffryes, and Spiros N Agathos. "Design and characterization of a scalable airlift flat panel photobioreactor for microalgae cultivation". In: *Journal of applied phycology* 27.1 (2015), pp. 75–86.

[71] Ming Li, Dawei Hu, and Hong Liu. "Photobioreactor with ideal light–dark cycle designed and built from mathematical modeling and CFD simulation". In: *Ecological engineering* 73 (2014), pp. 162–167.

[72] Abhinav Soman and Yogendra Shastri. "Optimization of novel photobioreactor design using computational fluid dynamics". In: *Applied Energy* 140 (2015), pp. 246–255.

[73] Wolf-Dieter Deckwer and Robert W Field. *Bubble column reactors*. Vol. 200. Wiley New York, 1992.

[74] A Zaruba, E Krepper, H-M Prasser, and E Schleicher. "Measurement of bubble velocity profiles and turbulent diffusion coefficients of the gaseous phase in rectangular bubble column using image processing". In: *Experimental thermal and fluid science* 29.7 (2005), pp. 851–860.

[75] S Guet and G Ooms. "Fluid mechanical aspects of the gas-lift technique". In: *Annu. Rev. Fluid Mech.* 38 (2006), pp. 225–249.

[76] Henk J. Noorman. "Mass transfer". In: *Basic biotechnology*. Cambridge University Press, 2006. Chap. 8, pp. 201–217.

[77] Jean Philibert. "One and a half century of diffusion: Fick, Einstein, before and beyond". In: *Diffusion Fundamentals* 4.6 (2006), pp. 1–19.

[78] R Byron Bird, Edwin N Lightfoot, and E Warren Stewart. *Transport phenomena. 2nd*. Wiley, 2002.

[79] Adolf Fick. "Ueber diffusion". In: *Annalen der Physik* 170.1 (1855), pp. 59–86.

[80] Charles Henrickson. *Chemistry. Cliffs Notes*. Tech. rep. ISBN 0-764-57419-1., 2005.

[81] William Henry. "Experiments on the quantity of gases absorbed by water, at different temperatures, and under different pressures". In: *Philosophical Transactions of the Royal Society of London* 93 (1803), pp. 29–276.

[82] W. H. Nernst. "Theorie der Reaktionsgeschwindigkeit in heterogenen Systemen". In: *Z. Phys. Chem.* 47 (1904), pp. 52–55.

[83] W. K. Lewis and W. G. Whitman. "Principles of gas absorption." In: *Industrial & Engineering Chemistry* 16.12 (1924), pp. 1215–1220.

[84] Jirı Masojıdek, Michal Koblızek, and Giuseppe Torzillo. "Photosynthesis in microalgae". In: *Handbook of microalgal culture: biotechnology and applied phycology* 20 (2004).

[85] Michelle Rasmussen and Shelley D Minteer. "Photobioelectrochemistry: Solar energy conversion and biofuel production with photosynthetic catalysts". In: *Journal of The Electrochemical Society* 161.10 (2014), H647–H655.

[86] Said Abu-Ghosh, Dror Fixler, Zvy Dubinsky, and David Iluz. "Flashing light in microalgae biotechnology". In: *Bioresource technology* 203 (2016), pp. 357–363.

[87] Quentin Béchet, Andy Shilton, and Benoit Guieysse. "Modeling the effects of light and temperature on algae growth: state of the art and critical assessment for productivity prediction during outdoor cultivation". In: *Biotechnology advances* 31.8 (2013), pp. 1648–1663.

[88] Bo-Ping Han. "Photosynthesis–irradiance response at physiological level: a mechanistic model". In: *Journal of theoretical biology* 213.2 (2001), pp. 121–127.

[89] Bo-Ping Han. "A mechanistic model of algal photoinhibition induced by photodamage to photosystem-II". In: *Journal of theoretical biology* 214.4 (2002), pp. 519–527.

[90] Xiaoxi Wu and Jose C Merchuk. "A model integrating fluid dynamics in photosynthesis and photoinhibition processes". In: *Chemical Engineering Science* 56.11 (2001), pp. 3527–3538.

[91] Victor Pozzobon and Patrick Perre. "Han's model parameters for microalgae grown under intermittent illumination: Determined using particle swarm optimization". In: *Journal of theoretical biology* 437 (2018), pp. 29–35.

[92] E Molina Grima, F García Camacho, JA Sanchez Perez, JM Fernandez Sevilla, FG Acien Fernandez, and A Contreras Gomez. "A mathematical model of microalgal growth in light-limited chemostat culture". In: *Journal of Chemical Technology & Biotechnology: International Research in Process, Environmental AND Clean Technology* 61.2 (1994), pp. 167–173.

[93] Melika Baklouti, Vincent Faure, Lionel Pawlowski, and Antoine Sciandra. "Investigation and sensitivity analysis of a mechanistic phytoplankton model implemented in a new modular numerical tool (Eco3M) dedicated to biogeochemical modelling". In: *Progress in Oceanography* 71.1 (2006), pp. 34–58.

[94] S Esposito, V Botte, D Iudicone, and M Ribera d'Alcala. "Numerical analysis of cumulative impact of phytoplankton photoresponses to light variation on carbon assimilation". In: *Journal of theoretical biology* 261.3 (2009), pp. 361–371.

[95] Philipp Hartmann, David Demory, Charlotte Combe, Raouf Hamouda, Anne-Céline Boulanger, Marie-Odile Bristeau, Jacques Sainte-Marie, Bruno Sialve, Jean-Philippe Steyer, Sophie Rabouille, et al. "Growth rate estimation of algae in raceway ponds: A novel approach". In: *IFAC Proceedings Volumes* 47.3 (2014), pp. 6216–6221.

[96] Andreas Nikolaou, Philipp Hartmann, Antoine Sciandra, Benoît Chachuat, and Olivier Bernard. "Dynamic coupling of photoacclimation and photoinhibition in a model of microalgae growth". In: *Journal of theoretical biology* 390 (2016), pp. 61–72.

[97] Daniel Undurraga, Paola Poirrier, and Rolando Chamy. "Microalgae growth kinetic model based on the PSII quantum yield and its utilization in the operational curves construction". In: *Algal Research* 17 (2016), pp. 330–340.

[98] Andrea Bernardi, Andreas Nikolaou, Andrea Meneghesso, Tomas Morosinotto, Benoît Chachuat, and Fabrizio Bezzo. "High-fidelity modelling methodology of light-limited photosynthetic production in microalgae". In: *PloS one* 11.4 (2016), e0152387.

[99] Raina M Maier, Ian L Pepper, and Charles P Gerba. *Environmental microbiology*. Vol. 397. Academic press, 2009.

[100] Jens Nielsen. "Microbial process kinetics". In: *Basic biotechnology*. Cambridge University Press, 2006. Chap. 6, pp. 155–180.

[101] Jérôme Morchain, Jean-Christophe Gabelle, and Arnaud Cockx. "Coupling of biokinetic and population balance models to account for biological heterogeneity in bioreactors". In: *AIChE Journal* 59.2 (2013), pp. 369–379.

[102] D Ramkrishna. "Solution of population balance equations". In: *Chemical Engineering Science* 26.7 (1971), pp. 1134–1136.

[103] Ho M Hulburt and Stanley Katz. "Some problems in particle technology: A statistical mechanical formulation". In: *Chemical Engineering Science* 19.8 (1964), pp. 555–574.

[104] V Quedeville, H Ouazaite, B Polizzi, RO Fox, P Villedieu, P Fede, F Létisse, and J Morchain. "A two-dimensional population balance model for cell growth including multiple uptake systems". In: *Chemical Engineering Research and Design* 132 (2018), pp. 966–981.

[105] Yu-Dong Ding, Sha Zhao, Qiang Liao, Rong Chen, Yun Huang, and Xun Zhu. "Effect of CO2 bubbles behaviors on microalgal cells distribution and growth in bubble column photobioreactor". In: *International Journal of Hydrogen Energy* 41.8 (2016), pp. 4879–4887.

[106] Yu-Dong Ding, Sha Zhao, Xun Zhu, Qiang Liao, Qian Fu, and Yun Huang. "Dynamic behaviour of the CO2 bubble in a bubble column bioreactor for microalgal cultivation". In: *Clean Technologies and Environmental Policy* 18.7 (2016), pp. 2039–2047.

[107] Maria J Barbosa and René H Wijffels. "Overcoming shear stress of microalgae cultures in sparged photobioreactors". In: *Biotechnology and bioengineering* 85.1 (2004), pp. 78–85.

[108] Chinchin Wang and Christopher Q Lan. "Effects of shear stress on microalgae–A review". In: *Biotechnology advances* (2018).

[109] Thea Coward, Jonathan GM Lee, and Gary S Caldwell. "The effect of bubble size on the efficiency and economics of harvesting microalgae by foam flotation". In: *Journal of applied phycology* 27.2 (2015), pp. 733–742.

[110] Asterio Sánchez Mirón, Francisco Garcia Camacho, Antonio Contreras Gomez, Emilio Molina Grima, and Yusuf Chisti. "Bubble-column and airlift photobioreactors for algal culture". In: *AIChE Journal* 46.9 (2000), pp. 1872–1887.

[111] Jorge MS Rocha, Juan EC Garcia, and Marta HF Henriques. "Growth aspects of the marine microalga Nannochloropsis gaditana". In: *Biomolecular engineering* 20.4-6 (2003), pp. 237–242.

[112] David Demory, Charlotte Combe, Philipp Hartmann, Amélie Talec, Eric Pruvost, Raouf Hamouda, Fabien Souillé, Pierre-Olivier Lamare, Marie-Odile Bristeau, Jacques Sainte-Marie, et al. "How do microalgae perceive light in a high-rate pond? Towards more realistic Lagrangian experiments". In: *Royal Society open science* 5.5 (2018), p. 180523.

[113] Hasan N Oguz and Andrea Prosperetti. "Dynamics of bubble growth and detachment from a needle". In: *Journal of Fluid Mechanics* 257 (1993), pp. 111–145.

[114] JN Lin, SK Banerji, and H Yasuda. "Role of interfacial tension in the formation and the detachment of air bubbles. 1. A single hole on a horizontal plane immersed in water". In: *Langmuir* 10.3 (1994), pp. 936–942.

[115] SV Gnyloskurenko, AV Byakova, Oleksandr I Raychenko, and Takashi Nakamura. "Influence of wetting conditions on bubble formation at orifice in an inviscid liquid. Transformation of bubble shape and size". In: *Colloids and Surfaces A: Physicochemical and Engineering Aspects* 218.1 (2003), pp. 73–87.

[116] Wenbiao Jiang. "The role of solid surface in bubble formation and detachment at a submerged orifice". In: *arXiv preprint arXiv:1710.10576* (2017).

[117] John Shipley Rowlinson and Benjamin Widom. *Molecular theory of capillarity*. Dover Edition, 2002, p. 210.

[118] JC Burton, R Waldrep, and P Taborek. "Scaling and instabilities in bubble pinch-off". In: *Physical review letters* 94.18 (2005), p. 184502.

[119] ST Thoroddsen, TG Etoh, and K Takehara. "Experiments on bubble pinch-off". In: *Physics of Fluids* 19.4 (2007), p. 042101.

[120] Pierre-Gilles De Gennes, Françoise Brochard-Wyart, and David Quéré. *Capillarity and wetting phenomena: drops, bubbles, pearls, waves*. Springer Science & Business Media, 2004, p. 53.

[121] Nathan C Keim, Peder Møller, Wendy W Zhang, and Sidney R Nagel. "Breakup of air bubbles in water: Memory and breakdown of cylindrical symmetry". In: *Physical review letters* 97.14 (2006), p. 144503.

[122] Jacob N Israelachvili. *Intermolecular and surface forces*. Academic press, 2011, pp. 415–419.

[123] Benedict Samuel, Hong Zhao, and Kock-Yee Law. "Study of wetting and adhesion interactions between water and various polymer and superhydrophobic surfaces". In: *The Journal of Physical Chemistry C* 115.30 (2011), pp. 14852–14861.

[124] Yahui Xue, Yang Wu, Xiaowei Pei, Huiling Duan, Qunji Xue, and Feng Zhou. "How Solid–Liquid Adhesive Property Regulates Liquid Slippage on Solid Surfaces?" In: *Langmuir* 31.1 (2014), pp. 226–232.

[125] AV Byakova, Svyatoslav V Gnyloskurenko, Takashi Nakamura, and OI Raychenko. "Influence of wetting conditions on bubble formation at orifice in an inviscid liquid: Mechanism of bubble evolution". In: *Colloids and Surfaces A: Physicochemical and Engineering Aspects* 229.1 (2003), pp. 19–32.

[126] Masato Kukizaki and Tsubasa Wada. "Effect of the membrane wettability on the size and size distribution of microbubbles formed from Shirasu-porous-glass (SPG) membranes". In: *Colloids and Surfaces A: Physicochemical and Engineering Aspects* 317.1 (2008), pp. 146–154.

[127] Svyatoslav V Gnyloskurenko and Takashi Nakamura. "Wettability effect on bubble formation at nozzles in liquid aluminum". In: *Materials transactions* 44.11 (2003), pp. 2298–2302.

[128] G Corchero, A Medina, and FJ Higuera. "Effect of wetting conditions and flow rate on bubble formation at orifices submerged in water". In: *Colloids and Surfaces A: Physicochemical and Engineering Aspects* 290.1 (2006), pp. 41–49.

[129] Daniel J Wesley, Rachel M Smith, William B Zimmerman, and Jonathan R Howse. "Influence of Surface Wettability on Microbubble Formation". In: *Langmuir* 32.5 (2016), pp. 1269–1278.

[130] M Mantel and JP Wightman. "Influence of the surface chemistry on the wettability of stainless steel". In: *Surface and Interface analysis* 21.9 (1994), pp. 595–605.

[131] Nuttha Thongyai. "Study of stainless steel surface cleanability". PhD thesis. Thesis.(MS). King Mongkut's Institute of Technology North Bangkok, 2005.

[132] Mahshid Mohammadi and Kendra V Sharp. "Experimental techniques for bubble dynamics analysis in microchannels: a review". In: *Journal of fluids engineering* 135.2 (2013), p. 021202.

[133] Shahrouz Mohagheghian and Brian R Elbing. "Characterization of Bubble Size Distributions within a Bubble Column". In: *Fluids* 3.1 (2018), p. 13.

[134] William C Baker and James F Pouchot. "The measurement of gas flow part ii". In: *Journal of the Air Pollution Control Association* 33.2 (1983), pp. 156–162.

[135] Nobuyuki Otsu. "A threshold selection method from gray-level histograms". In: *IEEE transactions on systems, man, and cybernetics* 9.1 (1979), pp. 62–66.

[136] Mehmet Sezgin and Bülent Sankur. "Survey over image thresholding techniques and quantitative performance evaluation". In: *Journal of Electronic imaging* 13.1 (2004), pp. 146–166.

[137] Luc Vincent. "Morphological area openings and closings for grey-scale images". In: *Shape in Picture*. Springer, 1994, pp. 197–208.

[138] S Aoyama, K Hayashi, S Hosokawa, and A Tomiyama. "Shapes of ellipsoidal bubbles in infinite stagnant liquids". In: *International Journal of Multiphase Flow* 79 (2016), pp. 23–30.

[139] Jiming Wen, Qiunan Sun, Zhongning Sun, and Haifeng Gu. "An improved image processing technique for determination of volume and surface area of rising bubble". In: *International Journal of Multiphase Flow* 104 (2018), pp. 294–306.

[140] A Albadawi, DB Donoghue, AJ Robinson, DB Murray, and YMC Delaure. "On the analysis of bubble growth and detachment at low capillary and bond numbers using volume of fluid and level set methods". In: *Chemical Engineering Science* 90 (2013), pp. 77–91.

[141] INC Fluent. "Overview and Limitations of the VOF Model". In: *FLUENT 6.3 User's Guide*. 2006. Chap. 23.3.1.

[142] Cyril W Hirt and Billy D Nichols. "Volume of fluid (VOF) method for the dynamics of free boundaries". In: *Journal of computational physics* 39.1 (1981), pp. 201–225.

[143] Vinay R Gopala and Berend GM van Wachem. "Volume of fluid methods for immiscible-fluid and free-surface flows". In: *Chemical Engineering Journal* 141.1-3 (2008), pp. 204–221.

[144] M van Sint Annaland, NG Deen, and JAM Kuipers. "Numerical simulation of gas bubbles behaviour using a three-dimensional volume of fluid method". In: *Chemical Engineering Science* 60.11 (2005), pp. 2999–3011.

[145] D Gerlach, G Tomar, G Biswas, and F Durst. "Comparison of volume-of-fluid methods for surface tension-dominant two-phase flows". In: *International Journal of Heat and Mass Transfer* 49.3-4 (2006), pp. 740–754.

[146] J. U. Brackbill, Douglas B. Kothe, and Charles Zemach. "A continuum method for modeling surface tension". In: *Journal of computational physics* 100.2 (1992), pp. 335–354.

[147] Grétar Tryggvason, Bernard Bunner, Asghar Esmaeeli, Damir Juric, N Al-Rawahi, W Tauber, J Han, S Nas, and Y-J Jan. "A front-tracking method for the computations of multiphase flow". In: *Journal of Computational Physics* 169.2 (2001), pp. 708–759.

[148] G Bornia, A Cervone, Sandro Manservisi, Ruben Scardovelli, and Stephane Zaleski. "On the properties and limitations of the height function method in two-dimensional Cartesian geometry". In: *Journal of Computational Physics* 230.4 (2011), pp. 851–862.

[149] William F Noh and Paul Woodward. "SLIC (simple line interface calculation)". In: *Proceedings of the fifth international conference on numerical methods in fluid dynamics June 28–July 2, 1976 Twente University, Enschede*. Springer. 1976, pp. 330–340.

[150] David L. Youngs. "Time-dependent multi-material flow with large fluid distortion". In: *Numerical methods for fluid dynamics* 24.2 (1982), pp. 273–285.

[151] H Tang and LC Wrobel. "Modelling the interfacial flow of two immiscible liquids in mixing processes". In: *International journal of engineering science* 43.15-16 (2005), pp. 1234–1256.

[152] Samuel WJ Welch and John Wilson. "A volume of fluid based method for fluid flows with phase change". In: *Journal of computational physics* 160.2 (2000), pp. 662–682.

[153] Hrvoje Jasak, Aleksandar Jemcov, Zeljko Tukovic, et al. "OpenFOAM: A C++ library for complex physics simulations". In: *International workshop on coupled methods in numerical dynamics*. Vol. 1000. IUC Dubrovnik, Croatia. 2007, pp. 1–20.

[154] Christopher J Greenshields. "OpenFOAM user guide". In: *OpenFOAM Foundation Ltd, version* 3.1 (2015).

[155] CFD Open. "Openfoam programmer's guide". In: *OpenFOAM Foundation* 2.0 (2011).

[156] Holger Marschall, Korbinian Hinterberger, Christian Schüler, Florian Habla, and Olaf Hinrichsen. "Numerical simulation of species transfer across fluid interfaces in free-surface flows using OpenFOAM". In: *Chemical engineering science* 78 (2012), pp. 111–127.

[157] Suraj S Deshpande, Lakshman Anumolu, and Mario F Trujillo. "Evaluating the performance of the two-phase flow solver interFoam". In: *Computational science & discovery* 5.1 (2012), p. 014016.

[158] Daniel Deising, Holger Marschall, and Dieter Bothe. "A unified single-field model framework for Volume-Of-Fluid simulations of interfacial species transfer applied to bubbly flows". In: *Chemical Engineering Science* 139 (2016), pp. 173–195.

[159] Ankit Verma, R Babu, and Malay K Das. "Modelling of a Single Bubble Rising in a Liquid Column". In: *Fluid Mechanics and Fluid Power–Contemporary Research*. Springer, 2017, pp. 1059–1068.

[160] Ahmad Baniabedalruhman. "Dynamic meshing around fluid-fluid interfaces with applications to droplet tracking in contraction geometries". PhD thesis. Michigan Technological University, 2015.

[161] Axel Sielaff, Jochen Dietl, Stefan Herbert, and Peter Stephan. "The influence of system pressure on bubble coalescence in nucleate boiling". In: *Heat Transfer Engineering* 35.5 (2014), pp. 420–429.

[162] S Abishek, AJC King, and Ramesh Narayanaswamy. "Dynamics of a Taylor bubble in steady and pulsatile co-current flow of Newtonian and shear-thinning liquids in a vertical tube". In: *International Journal of Multiphase Flow* 74 (2015), pp. 148–164.

[163] Paola Brambilla and Alberto Guardone. "Automatic tracking of corona propagation in three-dimensional simulations of non-normal drop impact on a liquid film". In: *Computing* 95.5 (2013), pp. 415–424.

[164] Lui S H. *Numerical analysis of partial differential equations*. Vol. 102. John Wiley & Sons, 2012.

[165] Dmitri Kuzmin. "Introduction to computational fluid dynamics". In: *University of Dortmund, Dortmund* (2009).

[166] JR Grace. "Shapes and velocities of single drops and bubbles moving freely through immiscible liquids". In: *Chem. Eng. Res. Des.* 54 (1976), pp. 167–173.

[167] Johan T Padding, Niels G Deen, EAJF Frank Peters, and JAM Hans Kuipers. "Euler–Lagrange modeling of the hydrodynamics of dense multiphase flows". In: *Advances in Chemical Engineering*. Vol. 46. Elsevier, 2015, pp. 137–191.

[168] William L Haberman and RK Morton. *An experimental investigation of the drag and shape of air bubbles rising in various liquids*. Tech. rep. David Taylor Model Basin Washington DC, 1953.

[169] W Sabisch, M Wörner, G Grötzbach, and DG Cacuci. "3D Volume-of-Fluid simulation of a wobbling bubble in a gas-liquid system of low Morton number". In: *4th Int. Conf. on Multiphase Flow, New Orleans, USA*. 2001.

[170] Thomas Ziegenhein. "Fluid dynamics of bubbly flows". PhD thesis. Technischen Universität Berlin, 2016.

[171] A Albadawi, DB Donoghue, AJ Robinson, DB Murray, and YMC Delauré. "Influence of surface tension implementation in volume of fluid and coupled volume of fluid with level set methods for bubble growth and detachment". In: *International Journal of Multiphase Flow* 53 (2013), pp. 11–28.

[172] Manoj Kumar Tripathi, Kirti Chandra Sahu, and Rama Govindarajan. "Dynamics of an initially spherical bubble rising in quiescent liquid". In: *Nature communications* 6 (2015), p. 6268.

[173] R Kumar and NR Kuloor. "The formation of bubbles and drops". In: *Advances in chemical engineering* 8 (1970), pp. 255–368.

[174] Željko Tuković and Hrvoje Jasak. "A moving mesh finite volume interface tracking method for surface tension dominated interfacial fluid flow". In: *Computers & fluids* 55 (2012), pp. 70–84.

[175] Tomislav Maric, Holger Marschall, and Dieter Bothe. "voFoam-A geometrical Volume of Fluid algorithm on arbitrary unstructured meshes with local dynamic adaptive mesh refinement using OpenFOAM". In: *arXiv preprint arXiv:1305.3417* (2013).

[176] Eduardo Jacob-Lopes, Lucy Mara Cacia Ferreira Lacerda, and Telma Teixeira Franco. "Biomass production and carbon dioxide fixation by Aphanothece microscopica Nägeli in a bubble column photobioreactor". In: *Biochemical engineering journal* 40.1 (2008), pp. 27–34.

[177] Reza Ranjbar, Ryota Inoue, Hironori Shiraishi, Tomohisa Katsuda, and Shigeo Katoh. "High efficiency production of astaxanthin by autotrophic cultivation of Haematococcus pluvialis in a bubble column photobioreactor". In: *Biochemical Engineering Journal* 39.3 (2008), pp. 575–580.

[178] A Sánchez Mirón, M-C Cerón García, F García Camacho, E Molina Grima, and Y Chisti. "Mixing in bubble column and airlift reactors". In: *Chemical Engineering Research and Design* 82.10 (2004), pp. 1367–1374.

[179] W-D Deckwer, R Burckhart, and G Zoll. "Mixing and mass transfer in tall bubble columns". In: *Chemical Engineering Science* 29.11 (1974), pp. 2177–2188.

[180] Xiaosong Sun and Mikio Sakai. "Three-dimensional simulation of gas–solid–liquid flows using the DEM–VOF method". In: *Chemical Engineering Science* 134 (2015), pp. 531–548.

[181] Linmin Li and Baokuan Li. "Implementation and validation of a volume-of-fluid and discrete-element-method combined solver in OpenFOAM". In: *Particuology* 39 (2018), pp. 109–115.

[182] Olle Törnblom. "Introduction course in particle image velocimetry". In: *Course Introductory Material: STEM Project, KTH, Department of Mechanics, Stockholm Sweden* (2004).

[183] Ken Kiger, J Westerweel, and C Poelma. "Introduction of particle image velocimetry". In: *Burgers Program for Fluid Dynamics* (2016).

[184] Markus Raffel, Christian E Willert, Fulvio Scarano, Christian J Kähler, Steve T Wereley, and Jürgen Kompenhans. *Particle image velocimetry: a practical guide*. Springer, 2018.

[185] Wereley Steve. *ME 592: Fundamentals of Particle Image Velocimetry*. 2014. URL: https://nanohub.org/resources/20295.

[186] Feng-Chen Li and Koichi Hishida. "Particle image velocimetry techniques and its applications in multiphase systems". In: *Advances in Chemical Engineering* 37 (2009), pp. 87–147.

[187] I Dias and ML Reithmuller. "PIV in two-phase flows: simultaneous bubble sizing and liquid velocity measurements". In: *Laser Techniques Applied to Fluid Mechanics*. Springer, 2000, pp. 71–85.

[188] D Bröder and M Sommerfeld. "Planar shadow image velocimetry for the analysis of the hydrodynamics in bubbly flows". In: *Measurement Science and Technology* 18.8 (2007), p. 2513.

[189] Dong-Guan Seol, Tirtharaj Bhaumik, Christian Bergmann, and Scott A Socolofsky. "Particle image velocimetry measurements of the mean flow characteristics in a bubble plume". In: *Journal of engineering mechanics* 133.6 (2007), pp. 665–676.

[190] Marko Laakkonen, Markus Honkanen, Pentti Saarenrinne, and Juhani Aittamaa. "Local bubble size distributions, gas–liquid interfacial areas and gas holdups in a stirred vessel with particle image velocimetry". In: *Chemical Engineering Journal* 109.1-3 (2005), pp. 37–47.

[191] Mayur J Sathe, Iqbal H Thaker, Tyson E Strand, and Jyeshtharaj B Joshi. "Advanced PIV/LIF and shadowgraphy system to visualize flow structure in two-phase bubbly flows". In: *Chemical Engineering Science* 65.8 (2010), pp. 2431–2442.

[192] Xinquan Zhou, Benjamin Doup, and Xiaodong Sun. "Measurements of liquid-phase turbulence in gas–liquid two-phase flows using particle image velocimetry". In: *Measurement Science and Technology* 24.12 (2013), p. 125303.

[193] K Sakakibara, M Yamada, Y Miyamoto, and T Saito. "Measurement of the surrounding liquid motion of a single rising bubble using a Dual-Camera PIV system". In: *Flow Measurement and Instrumentation* 18.5-6 (2007), pp. 211–215.

[194] Ju Sang Kim, Sang Moon Kim, Hyun Dong Kim, Ho Seong Ji, and Kyung Chun Kim. "Dynamic structures of bubble-driven liquid flows in a cylindrical tank". In: *Experiments in fluids* 53.1 (2012), pp. 21–35.

[195] Minki Kim, Jun Ho Lee, and Hyungmin Park. "Study of bubble-induced turbulence in upward laminar bubbly pipe flows measured with a two-phase particle image velocimetry". In: *Experiments in Fluids* 57.4 (2016), p. 55.

[196] Aliyu M Aliyu, Hyunduk Seo, Hyogeun Kim, and Kyung Chun Kim. "Characteristics of bubble-induced liquid flows in a rectangular tank". In: *Experimental Thermal and Fluid Science* 97 (2018), pp. 21–35.

[197] Michael F Modest. *Radiative heat transfer*. Academic press, 2013.

[198] Subrahmanyan Chandrasekhar. *Radiative transfer*. Courier Corporation, 2013.

[199] Nicholas Metropolis and Stanislaw Ulam. "The monte carlo method". In: *Journal of the American statistical association* 44.247 (1949), pp. 335–341.

[200] Ramakant Pandey, Akhilesh Sahu, M Premalatha, et al. "Studies on light intensity distribution inside an open pond photo-bioreactor". In: *Bioprocess and biosystems engineering* 38.8 (2015), pp. 1547–1557.

[201] Jérémie Delatorre, Germain Baud, Jean-Jacques Bézian, Stéphane Blanco, Cyril Caliot, Jean-François Cornet, Christophe Coustet, Jérémi Dauchet, Mouna El Hafi, Vincent Eymet, et al. "Monte Carlo advances and concentrated solar applications". In: *Solar Energy* 103 (2014), pp. 653–681.

[202] C Mobley, E Boss, and C Roesler. *Ocean optics web book*. 2010.

[203] Laith S Sabri, Abbas J Sultan, and Muthanna H Al-Dahhan. "Mapping of microalgae culturing via radioactive particle tracking". In: *Chemical Engineering Science* 192 (2018), pp. 739–758.

université PARIS-SACLAY
ÉCOLE DOCTORALE
Sciences mécaniques et énergétiques, matériaux et géosciences (SMEMAG)

Titre : Simulation du bullage dans un photobioréacteur

Mots clés : photobioréacteur, bulles, ombroscopie, VOF, modélisation, simulation, OpenFOAM

Résumé : Au cours des dernières années, la culture de microalgues est largement étudiée pour produire des biocarburants et d'autres produits de valeur en fixant le dioxyde de carbone de l'atmosphère, afin d'atténuer simultanément les effets du changement climatique et de réduire la dépendance à l'égard des carburants fossiles. En comparaison avec les systèmes ouverts, les photobioréacteurs fermés sont davantage utilisés en laboratoire, car ils permettent de contrôler avec précision les facteurs environnementaux tels que le pH, la concentration en éléments nutritifs, etc. Le principe de fonctionnement d'un photobioréacteur repose sur l'injection de bulles dans le milieu de culture pour (i) apporter du dioxyde de carbone aux cellules (ii) agiter le liquide et favoriser le transfert de matière si aucun agitateur mécanique est employé. Par l'apport d'énergie lumineuse les cellules transforment le carbone inorganique en carbone organique par photosynthèse. Ainsi, les phénomènes physiques - l'écoulement, transfert de matière, transfert radiatif - et les phénomènes biologiques - photosynthèse, croissance cellulaire et mort - coexistent dans un photobioréacteur. Plus important encore, tous les phénomènes de base sont fortement dépendants les uns des autres. Des recherches récentes ont révélé que le comportement des bulles avait également une incidence directe sur le processus biologique. En raison du comportement significatif des bulles sur la productivité d'un photobioréacteur, la génération de bulles a été étudiée dans cette thèse au moyen de méthodes expérimentales et numériques.

Dans l'étude expérimentale, nous avons conçu puis fabriqué un nouveau photobioréacteur (colonne à bulles de forme rectangulaire) afin d'étudier le bullage in situ. L'emploi d'une technique d'ombroscopie couplée à une caméra vidéo (haute fréquence d'acquisition) a permis l'enregistrement de séries de bulles. Les images traitées ont permis de mesurer des caractéristiques de bulles (fréquence, volume, facteur de forme). Le volume moyen des bulles et la fréquence de formation de bulles augmentent avec le débit de gaz. De plus, la distribution volumique monodispersée à faible débit devient de plus en plus polydispersée par l'accroissement de celui-ci. L'évolution de la forme des bulles lors de leur remontée dans le liquide a été évaluée par l'emploi de deux facteurs de forme : le rapport d'aspect et la circularité. Ces facteurs diminuent avec la remontée des bulles et traduisent une déformation horizontalement. A débit élevé, les bulles coalescent plus fréquemment.

La simulation du bullage a été réalisé par l'emploi d'une méthode Volume of Fluid (VOF) et d'une bibliothèque open source de mécanique numérique des fluides OpenFOAM. Ces choix de méthodes sont motivés en raison de la robustesse d'OpenFOAM en matière de simulation d'écoulements diphasiques rapportée dans la littérature. Une première étude numérique de simulation 2D a permis de déterminer les valeurs appropriées des paramètres numériques (nombre de Courant et la taille du maillage) tout en minimisant le temps de calcul par rapport à une pré-étude 3D. Sans surprise, nous avons déterminé que la taille des mailles devait être inférieure au diamètre de la buse pour obtenir des résultats significatifs. De façon plus surprenante, nous avons observé que le nombre maximum de Courant n'a pas d'importance particulière pour ces simulations (dans une limite raisonnable : 0 à 1). Les simulations 3D ont ensuite été menées sur un supercalculateur du Mésocentre Fusion (Université Paris Saclay). Elles ont montré que le volume des bulles et l'évolution de leur forme calculées numériquement étaient en accord avec les résultats expérimentaux. Cependant, les simulations 3D n'ont pas permis de représenter la polydispersité de la distribution volumique des bulles en raison d'un temps de calcul nécessaire trop important pour générer une population de bulles suffisamment nombreuses. Pour finir, l'outil numérique a aussi été utilisé pour explorer plusieurs caractéristiques hydrodynamiques de mélange dans un réacteur d'un litre de forme cylindrique.

Pour conclure, le comportement des bulles a été suivi à la fois par des méthodes expérimentales et numériques Cette première étape nous aidera à aller plus loin dans la compréhension des phénomènes physico-biologiques complexes qui ont lieu au sein d'un photobioréacteur.

Title : Simulation of bubbling in a photobioreactor

Keywords : photobioreactor, bubbles, shadowgraphy, VOF, modeling, simulation, OpenFOAM

Abstract : In recent years, microalgae cultivation has been widely studied to produce biofuel and other valuable products by fixing carbon dioxide from the atmosphere, with the aim to mitigate both the climate change and the strong dependence on fossil fuel. In comparison with open ponds, closed photobioreactors are more often used in laboratory due to their accurate control of environmental factors like pH, nutrient concentration, etc. The working principle of a typical photobioreactor is to inject gas bubbles into the culture medium, (i) providing carbon dioxide to the cells and (ii) stirring the liquid. The cells convert inorganic carbon into organic carbon through photosynthesis under illumination. Therefore, physical phenomena, e.g. bubbly flow, mass transfer, radiative transfer, and biological phenomena, e.g. photosynthesis, cell growth and death, coexist in a photobioreactor. More importantly, all the basic phenomena are strongly dependent to each other. Some recent research revealed that bubble behavior may directly affect the biological process. In this context, the aim of this study was to investigate the bubbly flow in a reactor column by both experimental and numerical methods.

In the experimental part, we first designed and manufactured a new photobioreactor (rectangular shape bubble column) to in situ study the bubbling. Coupling a shadowgraphy technique with a high-speed recording video camera allows capturing bubbles train. Both averaged bubble volume and bubbling frequency increased with gas flow rate. Furthermore, quite monodisperse distribution of bubble volume was obtained at low flow rate. Polydispersity increased with the flow rate. The bubble shape evolution was quantitatively assessed using two shape factors, an aspect ratio and a circularity. We found that both shape factors dropped rapidly during bubble rising as soon as the bubble detached from the nozzle which implied that bubbles were flattened. At higher flow rate, bubble coalescence occurred quite frequently.

Volume of Fluid (VOF) method and OpenFOAM, an open source CFD library, were chosen to perform the bubbling simulation. This choice of methods was made since the robustness of OpenFOAM in simulating two-phase flow was reported by the literature. In a first step, 2D simulations were carried out for determining appropriate values of numerical parameters such as the maximum Courant number and mesh size. We found that mesh size should somehow be largely smaller than the nozzle diameter to have meaningful results. On the other hand, maximum Courant number had no importance in the simulations (provided that its value belongs between 0 and 1). Furthermore, 3D simulations were performed in a computing cluster (Mesocentre Fusion, University Paris Saclay). Calculated bubble volume and bubble shape evolution were in correct accordance with the experiments. However, 3D simulations were not able to represent the polydispersity of bubble volume distribution due to a much higher computing time for considering a sufficient number of bubbles. Finally, several hydrodynamic characteristics related to mixing thanks to a bubbling in a cylindrical shape one liter reactor were also explored by the proposed numerical tool.

To conclude, bubble behaviors were successfully captured by experimental methods and represented by numerical methods. This first step helps us to go further in understanding the complicated physical-biological phenomena of a photobioreactor.

Université Paris-Saclay
Espace Technologique / Immeuble Discovery
Route de l'Orme aux Merisiers RD 128 / 91190 Saint-Aubin, France